University of Pretoria

Faculty of Engineering, Built Environment and Information Technology

Department of Mechanical and Aeronautical Engineering

The feasibility of rotor fault detection from a fluid dynamics perspective

by Shane Laurence Robbins

October 2019

Supervisor: Prof P.S. Heyns
Co-supervisor: Dr J.A. Heyns

Dissertation submitted in partial fulfilment of the requirements for the degree in Master of Mechanical and Aeronautical Engineering

Abstract

Title	The feasibility of rotor fault detection from a fluid dynamics perspective
Institution	University of Pretoria
Faculty	Engineering, Built Environment and Information Technology
Department	Mechanical and Aeronautical Engineering
Author	Shane Laurence Robbins
Student Number	13056281
Supervisor	Prof P.S. Heyns
Co-supervisor	Dr J.A. Heyns
Date of Report	October 2019

The majority of condition monitoring techniques employed today consider the acquisitioning and analysis of structural responses as a means of profiling machine condition and performing fault detection. Modern research and newer technologies are driving towards non-contact and non-invasive methods for better machine characterisation. In particular, unshrouded rotors which are exposed to a full field of fluid interaction such as helicopter rotors and wind turbines, amongst others, benefit from such an approach. Current literature lacks investigations into the monitoring and detection of anomalous conditions using fluid dynamic behaviour. This is interesting when one considers that rotors of this nature are typically slender, implying that their structural behaviour is likely to be dependent on their aerodynamic behaviour and vice versa.

This study sets out to investigate whether a seeded rotor fault can be inferred from the flow field. Studies of this nature have the potential to further a branch of condition monitoring techniques. It is envisaged that successful detection of rotor anomalies from the flow field will aid in better distinction between mass and aerodynamic imbalances experienced by rotor systems. Furthermore, the eventual goal is to better describe the adjustments made to helicopter rotor systems when performing rotor track and balance procedures.

Time-dependent fluid dynamic data is numerically simulated around a helicopter tail rotor blade using URANS CFD with the OpenFOAM software package. Pressures are probed at locations in the field of the rotor and compared to results attained in an experimental investigation where good correlation is seen between the results. A blade is modelled with a seeded fault in the form of a single blade out of plane by 4°. Comparisons are drawn between the blade in its ‘healthy’ and ‘faulty’ configuration. It is observed that the fault can be detected by deviations in the amplitudes of the pressure signals for a single revolution at the probed locations in the field. These deviations manifest as increases in the frequency spectrum at frequencies equivalent to the rotational rate (1 per revolution frequencies). The results described are assessed for their fidelity when the pressure is probed at different locations in the domain of the rotor. Deviations in the pressure profiles over the surface of the blades are also seen for the asymmetric rotor configuration but may prove too sensitive for practical application.

Keywords: CFD; Condition Based Maintenance; Condition Monitoring; Fault Detection; Fluid Dynamics; Helicopter; Rotor; Unshrouded

Acknowledgements

I would like to thank and acknowledge the following people and organisations for their support, guidance, patience and contributions in the completion of this work:

- Prof. P.S. Heyns for his support, patience, guidance and for giving me the opportunity to perform this work. I am gracious for the insight you shared throughout this investigation and helping me mould it into the piece of work it has become.
- The C-AIM (Centre for Asset Integrity Management) Group for their support and facilities over the duration of this work.
- Dr. J.A. Heyns for putting aside his time to assist me. Your guidance and input helped me grow confidence and learn so much more through this journey. Furthermore, I appreciate the guidance you provided me personally.
- Mr. George Breitenbach for his assistance in the experimental setup and his guidance through the testing phase.
- The CHPC (Centre for High Performance Computing) in Cape Town for providing me with the resources to run my simulations.
- Charles Crosby, from the CHPC, for his support and timeous feedback whenever I had issues on the cluster. Also for taking the time to explain concepts which I did not understand when I had issues with my simulations.
- Denel Aerodynamics for their support of this project.

I would like to extend my appreciation on a more personal note to the following people:

- Ms. Bonolo Mokoka, the C-AIM programme manager, for always being so positive and motivating everyone in the group on a daily basis.
- Mr. Tony Sinclair, Mr. Geoffrey Balshaw and the entire team at Capital Equipment Group for your sponsorship and financial support over all these years. Without your help I would not be in the position I am today.
- My family and friends, your undoubted support and motivation kept me going. I cannot thank everyone enough for each of the roles you have played in uplifting me and allowing me to strive in everything that I do.

Table of Contents

Nomenclature

Acronyms and Abbreviations

AMI	Arbitrary Mesh Interface
BVI	Blade Vortex Interaction
CBM	Condition Based Maintenance
CFD	Computational Fluid Dynamics
CFL	Courant-Friedrichs-Lewy Number
CHPC	Centre for High Performance Computing
CM	Condition Monitoring
DES	Detached Eddy Simulation
DNS	Direct Numerical Simulation
DP	Design Point
EVM	Eddy Viscosity Model
FEA	Finite Element Analysis
FFT	Fast Fourier Transform
FSI	Fluid Structure Interaction
HAWT	Horizontal Axis Wind Turbine
HUMS	Health and Usage Monitoring System
LES	Large Eddy Simulation
Ma	Mach Number
MRF	Moving or Multiple Reference Frame
NACA	National Advisory Committee for Aeronautics
NDT	Non-Destructive Testing
NS	Navier-Stokes
OpenFOAM	Open Source Field Operation and Manipulation
PSP	Pressure Sensitive Paint
RANS	Reynolds Averaged Navier-Stokes
Re	Reynolds Number
RPM	Revolutions per Minute
RSM	Reynolds Stress Model
RTB	Rotor Track and Balance
SA	Spalart Allmaras
sF	simpleFoam
SGS	Sub-grid Scale
SRF	Single Reference Frame
SST	k-Omega SST
TSA	Time-Synchronous Average
URANS	Unsteady Reynolds Averaged Navier-Stokes
VAWT	Vertical Axis Wind Turbine

General Symbols

a	Speed of Sound	m/s
A_p	Planform Area	m^2
b	Span Length	m
c	Chord Length	m
C_D	Drag Coefficient	
C_f	Skin Friction Coefficient	
C_L	Lift Coefficient	
C_p	Pressure Coefficient	

C_v	Specific Heat at Constant Volume	J/K
D	Drag Force or Diameter	N or m
F	Faulty, Force or Frequency	-, N or Hz
H	Healthy	
k	Ratio of Specific Heats or Turbulent Kinetic Energy	- or J/kg
i	Internal Energy	J/kg
L	Lift Force or Length	N or m
L_c	Characteristic Length	m
M	Moment	Nm
N	Rotational Velocity	RPM
P, p	Pressure	Pa or kPa
P_∞	Free Stream Pressure	Pa or kPa
r	Radius	m
R	Gas Constant	J/kg.K
S	Source Terms	
t	Time	s or h
T	Temperature or Time Period	K or s
u, v, w	Velocity Components	m/s
$\bar{u}$	Velocity Vector or Time Mean Velocity	m/s
u’	Fluctuating Velocity	m/s
U, V	Velocity	m/s
U^+	Normalised Velocity	
x,y,z	Spatial Components	m
Y^+ or y^+	Non-dimensional Distance	

Greek Symbols

α	Angle of attack	Degrees [°]
λ	Volume Viscosity	
μ	Dynamic Viscosity	kg/m.s
ν	Kinematic Viscosity (nu)	m^2/s
ν_t	Turbulent Kinematic Viscosity (nut)	m^2/s
$\tilde{\nu}$	Turbulence Field Variable (nuTilda)	m^2/s
ω	Rotational velocity or Specific Turbulence Dissipation	Rad/s or 1/s
Φ	Dissipation Function of Energy	
ρ	Density	kg/m^3
τ_w	Wall shear stress	Pa

Chapter 1 – Introduction

1.1 Background

Rotating machinery exist in numerous industries fulfilling roles dependent on the required task of the mechanical system as a whole. Of particular interest to this study are rotating machinery specifically consisting of a single rotor, where the rotor is unshrouded, and thus a full field of flowing fluid is present as a result of the turning rotor. Such rotor blades are often slender which means that their structural behaviour is likely to have a dependence on their aerodynamic behaviour and vice versa.

The monitoring and subsequent maintenance of rotating machinery is an important factor in ensuring a productive life cycle and hence that the system as a whole operates smoothly for as long as possible. Distinctively, the condition of rotor blades themselves is a concern as failure of these components can be catastrophic and lethal. When in operation, mechanical systems are susceptible to vibrations due to dynamic phenomena generated by the components of the machine. In most machinery, vibrations are undesired due to the mechanical stress and fatigue it causes on all the components, but on the whole is unavoidable. The vibrations represent the full working physics of all the components including structural and aerodynamic anomalies. As such, vibration based measurements have become a reliable means for the condition monitoring of rotating machinery as it is known that machine condition changes can be observed in these measurements using various signal processing techniques.

Condition monitoring can be complicated, time consuming and expensive. For this reason, there is a constant drive to continually develop it so that more accurate, time efficient and financially cheaper methods can be found. When considering the condition monitoring procedures performed on most rotating machinery, structural responses are the prime focus of techniques and algorithms currently used. However, considering the phenomena which play a part in the behaviour of the machinery being considered, aerodynamics are as much of a contributor to irregularities and the response of the machine as structural phenomena. With this being said, measurement of fluid dynamic behaviour for the purpose of fault detection is not well represented in research or recognised as a useful means of assessing the condition of rotating machinery.

This poses the question of what can be gained from the aerodynamics about the condition of rotating machinery. If there is information in the flow field data relating to fault detection, could the physics be modelled adequately enough to develop a condition monitoring procedure? This study assesses the feasibility of detecting a rotor fault from flow field data using a fluid dynamics model. This is in an effort to establish a foundation of what one could infer from the flow field about machine condition.

Intuitively, the practicality of using a system which measures flow field data may be questionable when an assortment of implications are considered, for instance the setup of measuring systems in the presence of rotating machinery, or the response of such a system to external interactions. The clarity with which the fault may present itself in the information and how this information will be gathered in actual circumstances has not been investigated; which means that full practicality of a measuring and diagnostic technique will be considered depending on the feasibility of the study.

Modelling rotors of rotating machinery with faults provides a safer and financially cheaper alternative to performing the tests experimentally. With success of the modelling and thus identification of the fault from fluid dynamic data, an abundance of information is available. The model provides a better understanding of the fluid behaviours present from which

phenomena can be understood that cause particular behaviours of the machine. This provides a base which can be used for investigation of better diagnostic approaches and fault rectification, which may lead to the development of future monitoring techniques.

With the problem statement described a priori, the hypothesis cannot be tested for all classes of rotors and known faults available. For this reason a single class of rotor is selected, the helicopter tail rotor blade, which shall be subjected to a specific fault mechanism. Although the study focusses on a single rotor type with a single fault, it provides ground for determining the feasibility of inferring rotor condition from the flow data, the primary goal, as well as the modelling thereof. To simplify the proof under scrutiny, a simple geometric anomaly is considered which may find relevance in the field of rotor track and balance on helicopter rotor systems.

The condition monitoring required to maintain general helicopter use is a prime example of why the field requires continual development and improvements. Helicopters experience high levels of vibration and noise with the main and tail rotors being large contributors towards this. Routine maintenance is time consuming and expensive which provides the reason for the large running costs and the time the helicopter spends out of use. As per the class of rotor defined for this investigation, helicopter rotor blades experience intricate phenomena (both structurally and aerodynamically) as a consequence of the complex motions they are required to perform so that a helicopter can undergo the typical manoeuvres they are known for.

1.2 Literature Review

This section reviews a few of the theoretical topics regarding fluid dynamics and the modelling thereof which form part of the main frame of the study to be performed. Sub-sections also discuss and summarise various literature as the topic at hand touches on numerous specialist fields, this will provide a necessary foundation from which the objectives of the study can be adequately scoped in section 1.3 with an understanding of its contributions and limitations.

1.2.1 Fluid Dynamics

Fluid flow around rotor blades introduces complex phenomena which the study aims to capture. Before one can commence into the more complex and intricate details of this particular fluid flow, the principles of fluid dynamics, which may present themselves, need to be considered. This section describes the various non-dimensional numbers often used to describe characteristics of flow in aerodynamics, which follows into a discussion on flow regimes for external flow and the characterisation of compressible flow. The final discussion of this section presents the governing equations of fluid flow.

A. *Non-Dimensional Numbers*

The comparison and analysis of flow regimes, forces and other phenomena is often performed using non-dimensional quantities. Non-dimensionalisation allows a number of variables to be represented in a compact manner with the added advantage that particular scenarios can be scaled to replicate the same physics represented by the specific non-dimensional quantity. The non-dimensional quantities presented below are used in numerous aerodynamic texts indicating the importance of their definition early on.

Reynolds number: The Reynolds number for a body defines the ratio of the inertial forces to the viscous forces experienced by the fluid (Smith, 2017).

$$Re = \frac{\rho V L_c}{\mu} \tag{1.1}$$

where ρ is the density, V is the freestream velocity, L_c is the characteristic length and μ is the dynamic viscosity.

Lift coefficient: The lift coefficient for a body defines the lift force experienced non-dimensionally.

$$C_L = \frac{L}{\frac{1}{2}\rho V^2 A_p} \tag{1.2}$$

where L is the lift force and A_p is the characteristic area which is defined as the planform area (body area as seen from above) for flat bodies such as wings and airfoils (White , 2011).

Drag coefficient: Similarly the drag coefficient expresses the drag force (D) experienced by the body non-dimensionally.

$$C_D = \frac{D}{\frac{1}{2}\rho V^2 A_p} \tag{1.3}$$

The drag force (D) experienced by the body is seen to include two contributors which include friction and pressure (form) drag. Friction drag is generated by the viscous forces imposed on the body by the fluid while the pressure drag is defined by the pressure difference between the leading and trailing edges as a result of the flow over the body.

Skin friction coefficient: The skin friction coefficient represents a non-dimensional form of the wall shear stress along the surface of the body. This quantity is indicative of the shear layer which develops due to viscous effects and the no-slip condition relative to the surface.

$$C_f = \frac{\tau_w}{\frac{1}{2}\rho V^2} \tag{1.4}$$

where τ_w is the wall shear stress.

Pressure coefficient: The pressure coefficient expresses the pressure along the surface of the body in a non-dimensional form to represent a normalised pressure.

$$C_p = \frac{P - P_\infty}{\frac{1}{2}\rho V^2} \tag{1.5}$$

where P is the pressure along the surface and P_∞ is the free-stream (also referred to as far field) pressure of the flow. The pressures can be either absolute or gauge where in the case of gauge pressure, the free stream pressure is often zero.

B. *Flow Regimes*

Fluid flow is characterised by three regimes, that being laminar, transitional and turbulent. The Reynolds number (Re) is typically used to identify which regime a particular flow falls into where, from equation 1.1, Re indicates the ratio of the inertial forces to viscous forces. Laminar flow is defined by low Re which implies the flow is dominated by viscous effects whereas turbulence is defined by high Re and thus dominated by inertial effects.

As mentioned, laminar flow occurs at low Re in which the flow is recognised by the fluid particles moving in a smooth layered fashion (where at very low Re it is described as having a viscous creeping motion) where no substantial mixing of the fluid occurs. Adjacent fluid layers are seen to slide past each other in an orderly fashion. The flow is stable as viscous effects allow for small disturbances being dissipated.

As Re increases, a change in the fluid behaviour occurs in which the flow ceases being smooth and steady (laminar) and becomes fluctuating and agitated (turbulent) where the intermediate stage in which the changeover occurs is called the transition to turbulence (White , 2011). All flows have the characteristic that they become unstable above a certain Re. The Re at which transition begins is often termed the critical Re and is the regime in which small disturbances start to grow. Transition occurs anywhere between the range of Re of 2000 to $1x10^6$ and is dependent on the type of flow being considered (Bakker & Fluent Inc., 2002-2008). In external fluid dynamics along a surface the onset of transition is considered to be around $Re_{critical} = 5x10^5$ (Bakker & Fluent Inc., 2002-2008; White , 2011). With an increasing Re the flow moves through the laminar and transitional regimes and ultimately becomes fully turbulent. Turbulent flow is slowly varying in the time-mean but has superimposed strong random high-frequency fluctuations (White , 2011). Turbulent flow is recognised by the fluid particles moving chaotically in which significant mixing of the fluid occurs and is considered to be a disorderly random phenomenon. Due to the unsteady, aperiodic (irregular) and random nature of this regime, it is difficult to describe turbulence using a full deterministic approach and thus it is often described statistically.

In analysing turbulent flows, identifiable swirling patterns may be observed which characterise turbulent eddies. The existence of such eddies implies rotation and thus vorticity in the flow where vorticity is defined as a measure of the degree of local rotation in the fluid (Bakker & Fluent Inc., 2002-2008). Mechanisms such as the stretching of three-dimensional vortices play a key role in turbulence. The magnitude (velocity) of the larger eddies is in the order of the mean flow, having been derived from it, where these larger eddies transfer energy (dissipate) to smaller eddies producing a cascade of swirling regions. In the smallest eddies, turbulent energy is converted to internal energy by viscous dissipation (ANSYS Inc., 2006).

Fluid flow far away from a surface can be treated as inviscid (negligible viscosity) flow. However, for flow near the surface, there is a thin region in which the viscous forces are of the same order of magnitude as the inertial forces and thus viscosity cannot be ignored. The region in which the viscous effects between the fluid and the surface are still noticeable is the velocity boundary layer and the distance over which the viscous forces have an effect is the boundary layer thickness (Bakker & Fluent Inc., 2002-2008). Figure 1-1 shows the development of the boundary layer for flow over a flat plate depicting the transition of the flow from the laminar to the turbulent regime when the flow becomes unstable and as the boundary layer grows in the streamwise direction from the leading edge. Near the surface, viscous stresses are strong due to friction and the so called no-slip condition which stipulates a zero relative velocity at the interface between the fluid and the surface. Because of this, the viscous sublayer (or laminar sublayer) region has very large velocity gradients and is laminar. The buffer layer describes a balance between viscous shear stresses and turbulent stresses whereas the overlap layer is also made up of these stress components but the turbulent stresses start to dominate the fluid behaviour intermittently. The turbulent layer is where the wall effects (stress components due to the wall) are almost non-existent and the flow behaves like a wake but cannot be considered inviscid since the viscosity still plays a role in the behaviour of the turbulent flow.

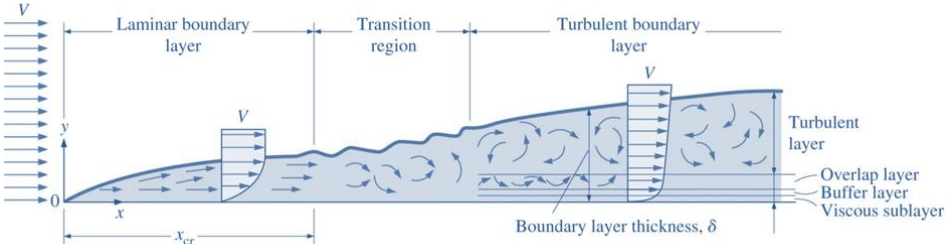

Figure 1-1: Development of the boundary layer for flow over a flat plate, and the different flow regimes (Cengel & Ghajar, 2011)

When a fluid separates from a body, it forms a separated region between the body and the fluid stream. This low-pressure region behind the body where recirculating and backflows occur is called the separated region. The larger the separated region, the larger the pressure drag (Cengel & Ghajar, 2011). Flow separation occurs as a result of adverse pressure gradients in the direction of the flow. A separation point may be observed after such an adverse gradient by considering the velocity profile along the surface where an inflection point in the profile will be seen indicating the reversed flow tendency in this region. Corners, sharp turns and high angles of attack all represent sharply decelerating flow situations where the loss in energy in the boundary layer leads to separation (Bakker & Fluent Inc., 2002-2008).

The region of flow trailing the body where the effects of the body on velocity are felt is called the wake region (Cengel & Ghajar, 2011). Another term which may often be heard in fluid dynamics is vortex shedding which is a phenomenon where vortices form in the wake of a body immersed in flow and which appear in an oscillatory manner due to periodic detachment from either side of the body. This phenomenon may present issues as it can cause the body to move towards the low pressure zones and thus initiate a vortex induced vibration.

C. *Compressible Flow*

Depending on the extent of variation of density during flow, the flow can be classified as either compressible or incompressible where the latter is an approximation that is often used if it can be assumed that the density of the fluid will remain fairly constant throughout. Incompressibility can be alternatively defined by saying that the volume of a given fluid particle should not change. The assumption of incompressibility is made for most liquid flows due to their resistance to density change during fluid flow (Cengel & Ghajar, 2011).

Gases however may experience density change during the motions of fluid flow and are thus considered compressible. Compressible flow can be defined juxtaposed to incompressible flow by saying that the volume of a given fluid particle is able to change with position which implies that the density will vary throughout the flow field. The effects of compressibility become significant when the speed of the fluid becomes comparable to the speed of sound through the fluid which is evaluated according to the Mach number (White , 2011).

$$Ma = \frac{V}{a} \tag{1.6}$$

where V is the flow velocity and a is the speed of sound of the fluid. For a perfect gas, the speed of sound can be found according to equation 1.7 (White , 2011).

$$a = \sqrt{kRT} \tag{1.7}$$

where k is the ratio of specific heats of the fluid, R is the gas constant of the fluid and T is the temperature.

The Mach number is generally used as a criterion for the classification of the levels of approximation required when modelling gaseous flows and gives a rough guide as to when a flow will fall into a particular class. The different effects experienced for different flow classes are defined by the magnitude of the Mach number as described below:

Ma < 0.3 → Incompressible flow: Density effects are negligible
0.3 < Ma < 0.8 → Subsonic flow: Density effects are important with no shock waves
0.8 < Ma < 1.2 → Transonic flow: Shock waves first appear, dividing subsonic and supersonic regions of the flow
1.2 < Ma < 3.0 → Supersonic flow: Shock waves strengthen reducing the presence of subsonic regions and confining them closer to the airfoil surface
3.0 < Ma → Hypersonic flow: Shock waves and other flow changes are strong

It should be noted that although gasses are highly compressible, the flow of a gas is not necessarily compressible and a class exists in which gaseous flows can be modelled as being incompressible (Cengel & Ghajar, 2011).

One may recall that density is a function of temperature and pressure and in high-speed flow of a gas there are significant deviations in these variables which must be related by an equation of state such as the perfect-gas law (White , 2011).

D. *Governing Equations*

The governing equations for fluid flow represent mathematical statements of the conservation laws of mass, momentum and energy. These equations are summarised collectively as the Navier-Stokes equations and are presented below in conservative form. The system of equations govern the time-dependent three-dimensional fluid flow and heat transfer of a compressible Newtonian fluid (Versteeg & Malalasekera, 2007):

Continuity:

$$\frac{\partial \rho}{\partial t} + div(\rho \bar{u}) = 0 \tag{1.8}$$

Momentum in the x-direction:

$$\frac{\partial (\rho u)}{\partial t} + div(\rho u \bar{u}) = -\frac{\partial p}{\partial x} + div(\mu\ grad\ u) + S_{Mx} \tag{1.9}$$

Momentum in the y-direction:

$$\frac{\partial (\rho v)}{\partial t} + div(\rho v \bar{u}) = -\frac{\partial p}{\partial y} + div(\mu\ grad\ v) + S_{My} \tag{1.10}$$

Momentum in the z-direction:

$$\frac{\partial (\rho w)}{\partial t} + div(\rho w \bar{u}) = -\frac{\partial p}{\partial z} + div(\mu\ grad\ w) + S_{Mz} \tag{1.11}$$

Energy:

$$\frac{\partial (\rho i)}{\partial t} + div(\rho i \bar{u}) = -p\ div(\bar{u}) + div\ (k\ grad\ T) + \phi + S_i \tag{1.12}$$

where:
- u – Velocity in x – direction
- v – Velocity in y – direction
- w – Velocity in z – direction
- p – Pressure
- ρ – Density of fluid
- μ – Viscosity
- i – Internal energy
- S – Source terms in each direction
- t – Time
- $\bar{u} = u\hat{\imath} + v\hat{\jmath} + w\hat{k}$

and

$$\phi = \mu \left\{ 2\left[\left(\frac{\partial u}{\partial x}\right)^2 + \left(\frac{\partial v}{\partial y}\right)^2 + \left(\frac{\partial w}{\partial z}\right)^2 \right] + \left(\frac{\partial u}{\partial y} + \frac{\partial v}{\partial x}\right)^2 + \left(\frac{\partial u}{\partial z} + \frac{\partial w}{\partial x}\right)^2 + \left(\frac{\partial v}{\partial z} + \frac{\partial w}{\partial y}\right)^2 \right\} + \lambda (div\ \bar{u})^2$$

Complementary to these equations are equations of state based on the thermodynamic conditions of the fluid particle:

Equations of state: $p = p(\rho, T)$ and $i = i(\rho, T)$

where in the case of a perfect gas the equations of state become:

$$p = \rho RT \text{ and } i = C_v T \tag{1.13}$$

where C_v is the constant volume specific heat of the fluid.

1.2.2 Computational Fluid Dynamics

Computational Fluid Dynamics (CFD) is the analysis of systems involving fluid flow, heat transfer and associated phenomena by means of computer-based simulations (Versteeg & Malalasekera, 2007). CFD is a tool that is used extensively in this investigation. Through CFD simulations, the flow fields around the rotor blade are solved such that information relating to the pressures, velocities and temperatures (where necessary) are available to observe the phenomena at work.

An overview of the CFD setup and tool to be used is discussed as well as the different levels of CFD approximations pertaining to turbulence modelling. The final section addresses the topic of modelling in the presence of a rotational domain.

A. *CFD Software and General Setup*

Various CFD software packages exist and are in use, some of which include ANSYS-Fluent, Numeca, Star CCM+, FloEFD and OpenFOAM to name a few. Selecting a software package is not a decision that should be taken lightly and one is often limited to the selection based on availability of the software in the environment in which they are in, computational power and other factors. For reasons pertaining to user support, academic support, licensing and computational power support systems OpenFOAM was selected as the CFD software package in which the flow around the helicopter tail rotor blade shall be modelled. OpenFOAM is an open-source CFD software package which is released and primarily developed by OpenCFD Ltd (OpenCFD Ltd, 2004-2019). Due to the fact that it is open-source, the software is powerful for many users as it can be custom developed according to individual requirements.

Simulation setup of any OpenFOAM case requires at least three directories which contain, at the very least, the text files described below:

- 0: the first time directory (or first iteration in the case of steady state simulations) contains files which describe the boundary conditions and initial conditions of all the field variables (e.g. U, p, nut, nuTilda).
- constant: contains a subdirectory, polyMesh, which encompasses multiple text files describing the mesh for the case. The directory also contains the files turbulenceProperties and transportProperties which select the turbulence model and set physical properties for the case respectively.
- system: includes files controlDict, fvSchemes and fvSolution which control the settings for the simulation procedure such as the selection of the type of physics being solved, the start and end times, the time step and settings for data output. The discretisation schemes and linear solvers used for the case are defined in the two latter files.

A CFD package obtains the solution to a problem by performing three top level functions; pre-processing, solving and then post-processing. Construction of the case files described above, along with other additional files, constitutes the majority of the pre-processing level as it outlines the inputs and constraints of the problem.

Once the pre-processing has been completed, the CFD package can begin to solve the problem. Field variables are computed throughout the domain for each control volume defined by the mesh according to a set of governing equations; the governing equations used are dependent on the type of solution desired with the standard being the Navier-Stokes equations described by equations 1.8 to 1.13. Post-processing is the final stage of the process where the user can view the results computed at various points of interest. Although CFD provides solutions it is important to assess the validity of the solutions obtained to make sure that they are sensible, based on literature and what is expected from knowledge of the topic being investigated.

B. *Turbulence Predictions*

CFD software packages are capable of representing both laminar and turbulent flows. For laminar flow, the governing Navier-Stokes equations can be solved directly (Bakker & Fluent Inc., 2002-2008). Turbulence, on the other hand, presents issues which require further numerical and computational effort.

Section 1.2.1.B gave an in depth discussion on turbulence phenomena where it was identified that turbulence brings about eddies. As a result of the dissipation of energy and fluctuation inherent in turbulence, eddies exist in a wide range of length and time scales that interact in a dynamically complex way in almost all physical flows. Large eddies contain the most turbulent kinetic energy with scale sizes in the order of the passages through which the flow moves through or in the order of the body around which the flow moves past. The energy from larger eddies are transferred to smaller eddies through dissipation. These flow characteristics need to be addressed in numerical solution methods as well where, in general, there is much difficulty in trying to accurately capture all the contributions at the various scales in which they appear (Bakker & Fluent Inc., 2002-2008; Versteeg & Malalasekera, 2007).

A substantial amount of research effort has been dedicated to the development of numerical methods so that the important effects due to turbulence can be captured (Versteeg & Malalasekera, 2007). The methods present different levels of solving the Navier-Stokes equations with different amounts of modelling incorporated into the solution schemes and can be grouped into three main categories. The first is the solution of the Reynolds-Averaged Navier-Stokes (RANS) equations which makes use of turbulence models to calculate the time-averaged flow fields for turbulent flows, secondly through large eddy simulation (LES) where larger scale turbulence is evaluated directly and finally by direct numerical simulations (DNS) which resolves all the important scales of turbulence in time and space.

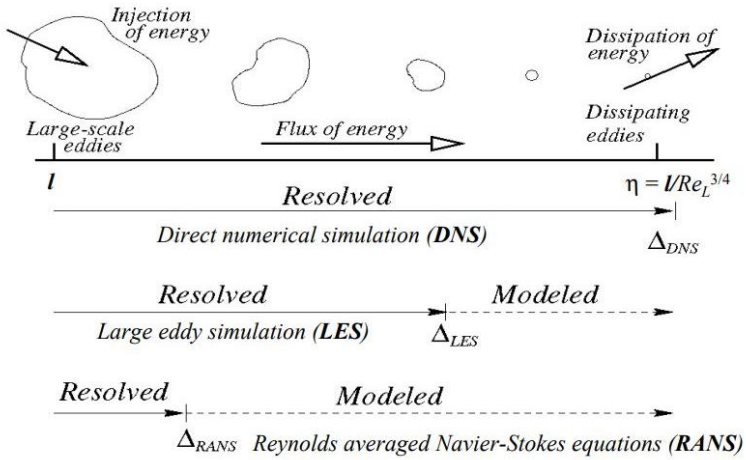

Figure 1-2: Numerical categories for the levels of modelling used in resolving turbulence (Bakker & Fluent Inc., 2002-2008)

Figure 1-2 shows the levels at which each of the categories of the numerical schemes resolve turbulent phenomena. Each of these categories of numerical simulation of turbulent flow will now be discussed in a bit more detail for a background of each.

Direct Numerical Simulation (DNS):

DNS simulations compute the solutions to the time-dependent (mean flow and turbulence fluctuations) Navier-Stokes equations without modelling. The unsteady Navier-Stokes equations are resolved on spatial grids that are fine enough to predict the smallest length scales of eddies at which dissipation is observed as well as at time

scales which capture the period of the fastest fluctuations thus resolving the full spectrum of scales (Versteeg & Malalasekera, 2007).

The issue with DNS is that it is immensely computationally intensive requiring vast amounts of computer power. This makes it impractical for most industrial applications and is often only used for simple low Reynolds number flows. For most engineering applications in industry it is often the case that this level of resolution is not necessary and the simpler mean flow properties generated with RANS models are sufficient.

Large Eddy Simulation (LES):

The larger length scale eddies are the main contributors for the transport (mixing) of mass, momentum and energy which have a direct implication on the mean flow fields serving as the primary component of turbulence. This leads one to directly resolving large scale eddies and modelling the smaller eddies which have less impact on the flow fields.

LES is a transient turbulence model which falls between the DNS and RANS models in terms of what is directly resolved and what is modelled. Time-dependent (transient) computations of the flow field are performed on spatially averaged forms of the Navier-Stokes equations for the flow field of the large eddies. Eddies smaller than the mesh sizes are modelled using a sub-grid scale (SGS) model of which many styles are available.

LES has the advantages that it is more accurate than RANS models and computationally cheaper than DNS but it is still computationally intensive, specifically with respect to storage and analysis of the large data sets that are generated which circumvents its practical use. It should be noted that LES performs three-dimensional transient modelling which can be avoided to a certain degree when using RANS models (ANSYS Inc., 2006; Bakker & Fluent Inc., 2002-2008).

Reynolds-Averaged Navier-Stokes (RANS) turbulence modelling:

Fluctuations inherent in turbulence result in the velocities, pressures, temperatures and other flow properties in the Navier-Stokes equations becoming rapidly varying functions of time and space. Each of these properties can be decomposed into a mean and fluctuating component as seen in Figure 1-3.

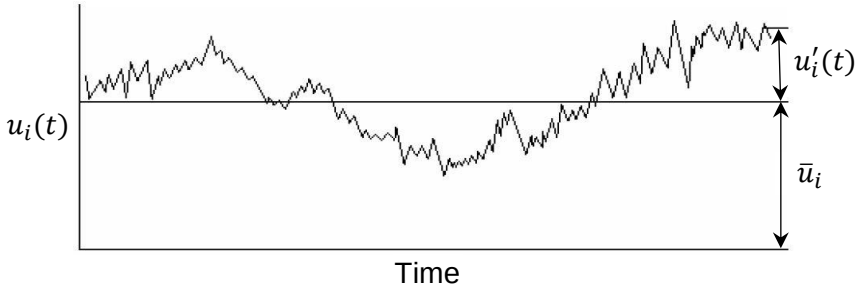

Figure 1-3: Mean and fluctuating components of properties in turbulent flow

The time mean of a turbulent function $u(x, y, z, t)$ is defined by (White , 2011):

$$\bar{u}_i = \frac{1}{T}\int_0^T u_i \, dt \tag{1.14}$$

where T is an averaging time period. The fluctuation u_i' at time t is defined as the deviation of u_i from its averaging value $\bar{u}_i$:

$$u_i'(t) = u_i(t) - \bar{u}_i \tag{1.15}$$

The standard Navier-Stokes equations require extensive resources to solve for such instantaneously fluctuating variables. Furthermore, in many instances it is sufficient to have mean values for flow properties when one resorts to CFD for answers in practice. This led to rewriting the Navier-Stokes equations in terms of mean or time-averaged turbulent variables. Each property is written in terms of its mean and fluctuating parts, represented by equations 1.14 and 1.15, and substituted into the Navier-Stokes equations to form the time-averaged Navier-Stokes equations. Doing this, however, brings about new terms known as Reynolds (or turbulent) stresses (White , 2011).

RANS turbulence modelling is the generation of computational procedures which provide sufficient accuracy in the prediction of the Reynolds stresses and other scalar transport terms. In doing this, closure of the time-averaged Navier-Stokes equations is obtained even though the various turbulence scales are being modelled. This allows for the computation and analysis of the mean flow properties, which includes the averaged effects of turbulence, without having to resolve the full time-dependent flow field. It is important to understand that the time-averaged flow pattern is not the flow pattern which one would observe but a statistical representation of it and it is uncommon that it would satisfy the steady Navier-Stokes equations (ANSYS Inc., 2006; Bakker & Fluent Inc., 2002-2008).

Turbulence models predict the Reynolds stresses by one of two methods, Eddy-Viscosity Models (EVM) or Reynolds-Stress Models (RSM). EVMs use the Boussinesq assumption to relate the Reynolds stresses to the mean flow by a turbulent viscosity. Different models are constructed to find a description for this turbulent viscosity such that an equivalent viscosity due to turbulence is obtained. This equivalent viscosity models the behaviour turbulence introduces. RSMs solve individual transport equations for the Reynolds stresses. This method is more complex, computationally expensive and does not utilise the idea of turbulent viscosity.

Classical turbulence models that are used to supplement RANS equations which fall under the divide of EVMs and RSMs range from zero-equation or algebraic models, half-equation, one-equation and two-equation models to the more intensive Reynolds stress models where some of the commonly used models are summarised as follows:

- Zero-equation model: Mixing length model
- One-equation model: Spalart Almaras Model
- Two-equation models: k-epsilon model family (Standard, RNG, Realizable), k-omega model family and ASM
- Seven-equation model: Reynolds stress model

The complexity of each model is signified by the number of equations which indicates the number of extra partial differential equations that need to be solved. With the multiple turbulence models available it is important to note that each model has its own advantages and disadvantages where particular models may be better suited to represent certain flow types better than others (Versteeg & Malalasekera, 2007).

Turbulence modelling through RANS simulations is the approach widely used for the computation of flows in industrial applications. It provides a smaller cell count, is capable of obtaining steady state solutions and requires less computational power than its counterparts. Unsteady RANS is often referred to as URANS, while RANS refers to both steady and unsteady computations.

RANS modelling presents issues in that there is not yet a single turbulence model that can reliably predict all turbulent flows in industrial applications with sufficient accuracy. There is also the issue that turbulence models have difficulty in making predictions in other flow regimes as they are calibrated for the phenomena which occur in the turbulent

regime, specifically when one considers the difference in the characteristics of separation for the different regimes. This means that attention must be given to the flow regimes in which the fluid will be expected to be found and the consequent modelling of the flow (Smith, 2017; Versteeg & Malalasekera, 2007).

When modelling turbulent flows, near wall treatment requires distinct consideration for accurate capturing of the boundary layer. It is possible to resolve the boundary layer but this comes at the cost of large cell counts. Wall functions allow parts of the boundary layer to be modelled. This is in accordance with the law of the wall which presents correlations that are used to calculate the shear stress in adjacent cells near the wall so that the effects of the boundary layer are captured appropriately without having to refine the mesh too much. The correlations presented by the law of the wall make use of the no slip condition to model friction and other viscous effects which occur near the wall in reality. The treatment of near walls has considerable effects on the results that are obtained due to the importance of this region on the overall flow (Versteeg & Malalasekera, 2007).

The y^+ value is a non-dimensional wall distance for a wall bounded flow which indicates the distance of the centroid of the first cell off the wall. Reported values of y^+ can be used to identify the level at which the boundary layer off the wall is being captured and signify the level of cell resolution required. From Figure 1-4 the law of the wall indicates that values of y^+ between 30 and 500 capture the turbulent boundary layer appropriately while wall functions are required to model the inner layers. Cells with y^+ values in the order of 1 are seen to capture the boundary layer and thus the full velocity profile, dismissing the need for modelling with wall functions.

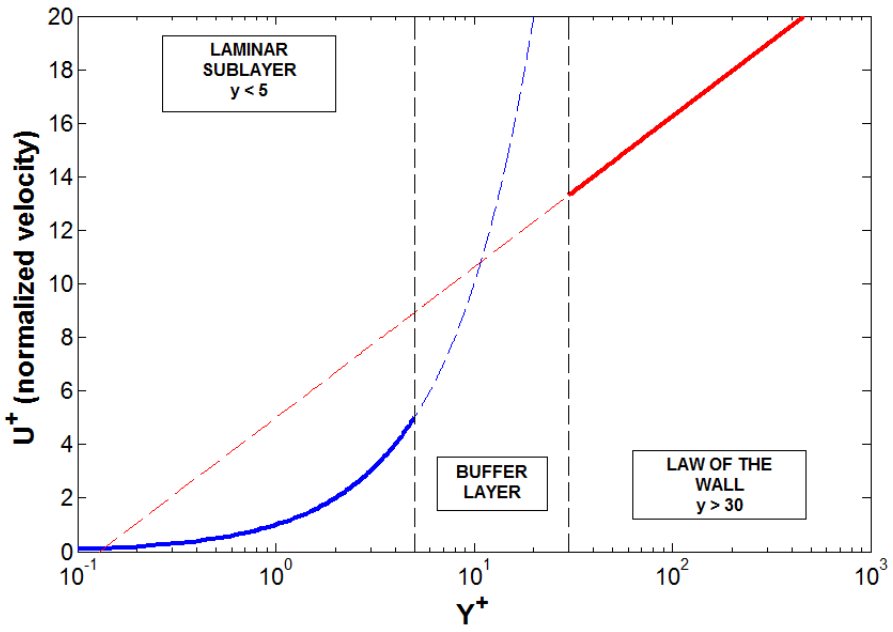

Figure 1-4: y^+ ranges for law of the wall (LEAP CFD Team, 2013)

Detached Eddy Simulation (DES):

DES is a hybrid model between RANS and LES which presents itself as another option to turbulence predictions with the mixture of accuracy provided by LES but the efficiency of RANS.

For high Reynolds number wall bounded flows, LES becomes prohibitively expensive to resolve the near-wall region. The use of RANS in near wall regions would significantly mitigate the mesh resolution requirement. DES is a practical alternative to LES for high-Reynolds number flows in external aerodynamic flows.

C. *Modelling Rotational Domains*

Many problems that are solved using CFD have components that are stationary where the software solves the governing equations for the fluid velocity, pressure and temperature, based merely on the inlet and outlet conditions. However, when considering rotating machinery, the effects of the moving components need to be accounted for. This complicates the process of simulating the rotor blade in a CFD package to some extent.

There are multiple options available for simulating rotating domains in the OpenFOAM environment. The selection of the method is dependent on the type of problem being solved, how the user goes about setting up the problem and the desired results. There are two key considerations when setting up simulations on rotational domains, the first being whether the setup consists of a Single Reference Frame (SRF) or Multiple Reference Frame (MRF) and the second being the use of a stationary or moving mesh.

Figure 1-5 shows two alterations for the setup of a basic rotor system in the presence of either a SRF or MRF. SRF is used when it is only the rotational domain that is of interest. whereas MRF may be used when there is a rotational domain as well as an interest in a stationary domain that surrounds the rotating component. In the example displayed, there may be a casing with baffles whose interaction with the rotor should be studied. In most uses of the MRF approach, it is required to specify a method for dealing with the interfaces (termed Arbitrary Mesh Interfaces or AMI in OpenFOAM) between the moving and stationary frames; solving for the interaction through these interfaces may lead to increased computational requirements and may introduce instabilities.

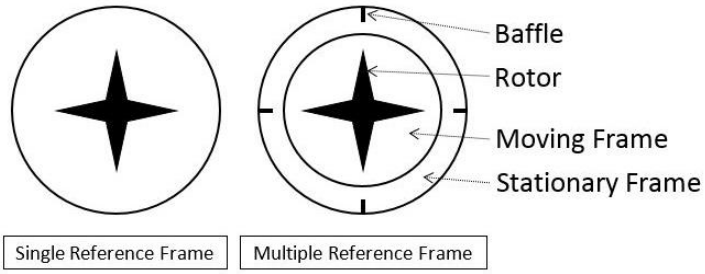

Figure 1-5: SRF and MRF simulation setups

For the instance in which a stationary mesh is used, the governing equations in the rotating frames are adjusted to include the extra forces (coriolis and centrifugal) experienced by the fluid, while the standard governing equations are solved when there are stationary regions. This method is sometimes termed the frozen rotor approach as the rotor is not physically moved, but the effects of rotation are accounted for. This does present the issue that the transient nature in which the moving and stationary components interact may not be captured appropriately as the rotor is fixed in one position (ANSYS, Inc., 2006).

When the dynamic mesh approach is used, the mesh points are physically moved. When used in a MRF setup it is said to be a sliding mesh setup due to the stationary and moving frames passing one another. The standard setup of equations and solution methods are not capable of dealing with the large deformations experienced by the mesh when using mesh motion. The Arbitrary Lagrangian Eulerian (ALE) method is used to transform the Navier-Stokes equations such that the computational domain is mapped to a stationary reference domain which the solution schemes can solve. The solution obtained in the reference domain is then mapped back to the computational domain where one should understand that it is through the equation transformation and consequent mapping that the rotation is accounted for. The workings of this method will not be discussed but the reader is referred to the following texts for more detail (Hirt, Amsden and Cook, 1974; Duarte, Gormaz and Natesan, 2004; Donea *et al.*, 2017).

1.2.3 Helicopter Rotor Behaviour

This section serves to gain an understanding of the numerous mechanisms at work when a helicopter rotor blade is in motion. The structural and aerodynamic behaviours that a helicopter rotor blade is known to excite may produce flow fields that interact with each other resulting in the occurrence of complex three dimensional phenomena and unsteadiness (Wagner, 2005). The rigid motions and deflections that a helicopter rotor blade generally experiences as well as some of the flow phenomena which can be expected as a result of the complex rotational motions shall be discussed.

It should be noted that majority of the literature found on helicopter rotor blades is specifically with reference to the main rotor. The phenomena and behaviours observed around the main rotor can be used to describe that of the tail rotor with a few exceptions due to the fact that each set of rotors perform similar functions with different objectives. Thus the workings of the main rotor can be related to the tail rotor with some simplifications and deviation.

In order to gain a better understanding of the workings, motions and expected flow phenomena of helicopter rotor blades a distinction needs to be made between the various modes of flight that a helicopter may endure as this has an effect on the physics and interactions at work. The flight modes may include an idle position (the helicopter is grounded but ready for flight), hover, axial flight, forward flight, backward flight and a few other modes which cannot be defined as broadly and have less relevance such as banking. The idle and hover flight modes will be of central consideration but forward flight presents interesting phenomena which may be mentioned and to which much of the literature is dedicated to.

Rotor blades may experience three primary rigid motions in the form of flapping, lagging and pitching (or feathering) (Wagner, 2005). Figure 1-6 shows these motions and how they would occur relative to the hub. On top of these rigid motions, the blade may experience bending and torsion as a result of the structural response to the aerodynamic forces. Such reactions lead to local changes in the angle of attack along the blade and complicated effects on the flow phenomena may be experienced. All these motions, factors and responses lead to a highly complicated motion of the complete rotor blade which is difficult to represent through a model. Figure 1-7 represents some of the interactions which may cause bending and torsion of the blade.

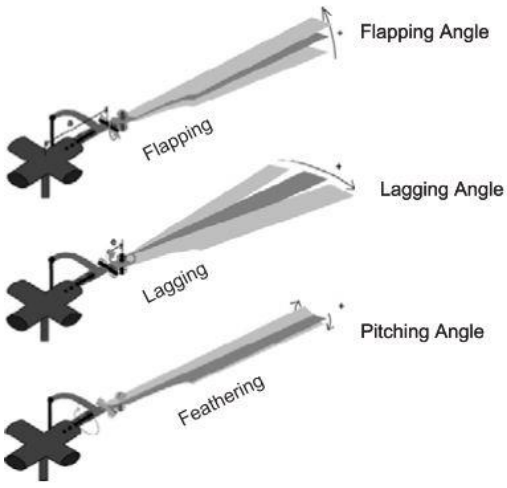

Figure 1-6: Components of an articulated rotor
(Wagner, 2005)

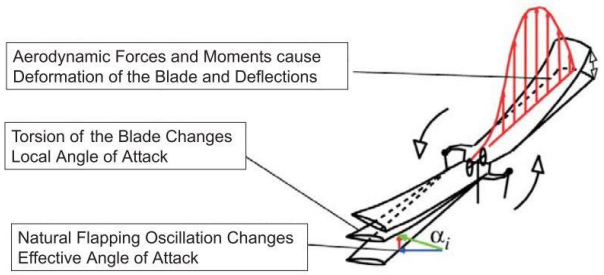

Figure 1-7: Flow structure interaction on a rotor blade
(Wagner, 2005)

The linear velocity at a specific radial distance along the blade may be related to the rotational speed as follows:

$$V = r\omega \tag{1.16}$$

where r is the radius at which the linear velocity, V, is to be determined and ω is the rotational velocity in rad/s.

Cross sections of the rotor may be simplified and represented as two-dimensional airfoils, where equation 1.16 can be used to compute the local velocity at which to analyse the section at. An important deduction from this equation is that it indicates that as one proceeds from the centre of the blade to the tip, the velocities increase, which suggest that all three flow regimes may be expected. Long blade lengths and high rotational speeds can lead to transonic flow at the tips of the main rotor blades, but with the much shorter blade lengths of the tail rotor it is not expected to reach such an extent, but will most likely enter the subsonic flow regime in which compressibility becomes important.

When in forward flight, the linear velocity vectors along the blade, due to its rotation, need to be added to the velocity vector of the helicopter as seen in Figure 1-8. This results in an asymmetric inflow which is an imbalance of the flow and thus the lift produced by the blades on the advancing and retreating sides. To balance the lift on either side and steady the helicopter the rotors react by flapping, lagging, pitching as well as oscillatory torsion of the blade (Wagner, 2005). The blade on the advancing side does not require a large angle of attack while the blade on the retreating side receives a pitch change to the extent where dynamic stall may occur. These motions lead to a zone of reverse flow on the retreating blade. Figure 1-9 summarises parts of this discussion where one may observe the angles of attack and resulting pressure fields of the blades on the advancing and retreating sides. It has been mentioned that the discussions made are with reference to the main rotor but may be applied to the tail rotor. It may also be realised that although this discussion refers to forward flight when it was identified as not being the main focus, it gives insight into the flow phenomena which may occur as a result of cross winds and other interactions when the helicopter is in idle or hover.

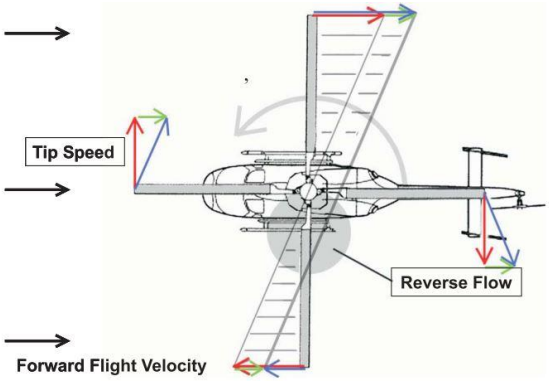

Figure 1-8: Superposition of velocities on a helicopter rotor (Wagner, 2005)

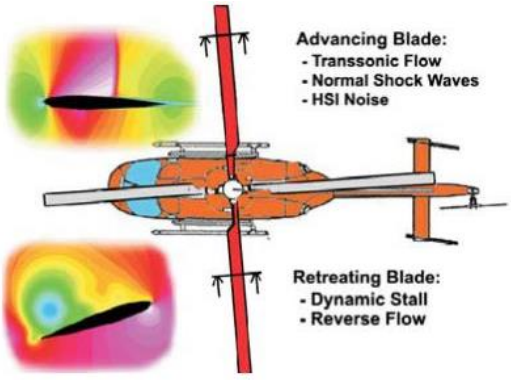

Figure 1-9: Flow problems on a helicopter rotor (Wagner 2005)

Having discussed some of the motions and interactions which a helicopter rotor blade is generally exposed to, it is seen that there are many factors at play resulting in complex motions and phenomena. All of these factors need to be considered for the modelling of the rotor blade as one needs to ensure that the different flow regimes will be represented well along with the likely presence of compressibility, separation, reversed flow and the trailing wakes. This is in addition to the occurrence of the blade passing through its own wake which is somewhat unique to the field of rotary wings applications and rotating machinery on a broader scale.

1.2.4 Rotor Condition Monitoring

Maintenance routines for most machinery can, in general, fall under two main categories as shown in Figure 1-10: corrective and preventative maintenance. Corrective maintenance (also referred to as unscheduled or failure-based maintenance) is the maintenance of machinery only when failure has occurred, this may be performed by the replacement of the failed part or by scraping the entire system and the commissioning of a new one. The continual upkeep and assessment of a machines operational condition in order to prevent and identify incipient failure is the strategy followed for preventative maintenance. Preventative maintenance can be further classified into scheduled (also time-based or planned) or condition-based maintenance, where the former is a routine in which maintenance is performed at set time intervals or at intervals in which the machine has been in operation. Alternatively, condition-based maintenance (CBM) is performed when necessary according to the identification of an incipient fault detected from the monitoring of the system. As a result of CBM being performed only when necessary, it exhausts the life of major components as well as requiring fewer maintenance procedures over the life of the machine proving financially beneficial.

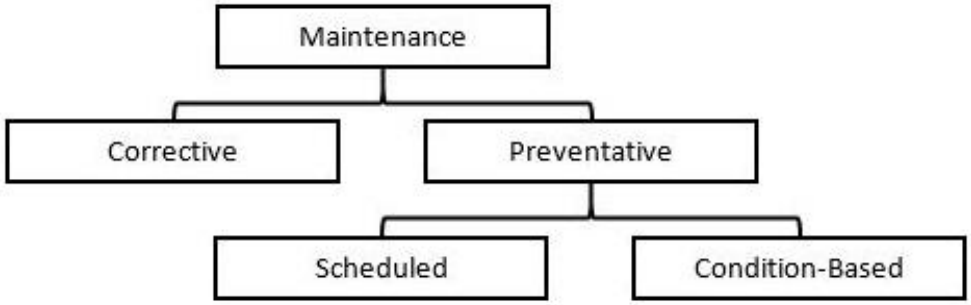

Figure 1-10: Typical maintenance routines

Condition monitoring (CM) forms the foundation on which CBM routines are based, as the machine and component condition is described by the monitoring system to indicate any maintenance that may be required in order to prevent failure. CM can be described as the monitoring and inspection techniques used to assess component integrity, identify possible damage and prevent failure which requires the acquisitioning, processing, analysis and interpretation of data from the machine (García Márquez *et al.*, 2012). Ample research has been conducted for each one of these constituents of CM for different machinery due to the benefits associated with performing this routine of maintenance. Specifically in the field of helicopters, Pawar and Ganguli (2007) describe the significant attention that research into monitoring systems has received due to its expectation in reducing the large maintenance costs involved in keeping a helicopter in operation.

The following sections describe literature relevant to the CM of rotor systems. Due to the intended research, similarities in the structural composition of the rotors, their fault mechanisms, operation and CM techniques employed; literature on helicopter rotors and wind turbines was studied. Faults which are typical of these rotor types are described in the first section. The section that follows describes the CM techniques currently used on these two rotor classes as described by the literature as well as references to other studies of interest. Finally the topic of rotor track and balance (RTB) in helicopter rotor systems is discussed in further detail.

A. *Rotor Damage and Fault Mechanisms*

This section serves to give the reader an understanding of the numerous damage and fault mechanisms which may present themselves in the rotor systems of interest. The abnormalities may exist as a result of the manufacturing procedure, installation error, failure of other components, exposure to the environment, material imperfections, fatigue, deterioration or cause problems as a result of its in operational dynamic behaviour.

Helicopter and wind turbine blades are commonly manufactured using composite materials. Composite materials present complexity in the understanding of their behaviour and the subsequent modelling of them, owing to the research being done on it. The manufacturing of the blades in this instance requires a high amount of manual work where defects may be included such as delamination's, voids, inclusions, cracks, dry fibres and defective fibre alignment (Amenabar *et al.*, 2011).

Over the lifespan of the rotor system, the rotor blades may start to present damage and fault mechanisms from its general use such as fatigue cracking, matrix cracking, de-bonding, fibre breakage, structural deformations and again delaminations. Owing to the environmental conditions experienced by the blades over their life they may show damage and not function accordingly due to dirt or ice on the blade, erosion, corrosion, ultraviolet irradiation, lightning strikes or moisture absorption (Yang and Sun, 2013).

Even if one were able to acquire rotor blades which were identical, the system may experience issues only when in operation and as a result of the dynamic behaviour of the rotor. These imperfections are usually presented as imbalances and since it is near impossible to manufacture identical blades, this may be accentuated by the other types of defects mentioned. Imbalances are seen to comprise of two parts, mass and aerodynamic imbalances. Non-uniform build-up of moisture, ice, material inconsistencies and other damage mechanisms create mass irregularities which cause mass imbalances. Kusnick, Adams and Griffith (2015) describe aerodynamic imbalances on wind turbines as the asymmetry introduced as a result of the individual blades not producing the same amount of thrust. They describe this to be as a result of a change in the blade profile due to defects as described above with the inclusion of incorrectly pitched blades. Aerodynamic imbalances on both types of rotor systems may also be due to blade mistracking where individual blades do not rotate in the same plane. Imbalances have an impact on the entire system as the defect manifests itself in blade failure and high hub loads, damaging bearings and other components.

Articulated helicopter rotor blades have many connections and components which work in unison for it to perform as desired. A damaged pitch control system, defective lag damper, damaged trim tab or misadjusted pitch link are all examples of components or sub-systems to the rotor which would negatively affect its performance.

B. *Condition Monitoring Techniques*

Common Contact, Non-Contact, and NDT Techniques for Structural Assessment:

One might say that when considering the literature on measurement techniques utilised for rotor CM that the vast majority serve to obtain one of two objectives, to make a direct structural observation or to acquire the blades structural response. Direct structural observations will seek to find imperfections or anomalies in the structural makeup of the blade with methods such as x-ray, computed tomography or infrared thermography being used. Response of the blade to loads which are applied statically or dynamically allow the blade to be characterised in terms of mechanical and dynamic parameters, changes in the blades response and thus its characteristic parameters signify the presence of abnormalities and probable flaws. Measurement techniques used to assess blade response include displacement sensors, velocity sensors, acceleration sensors,

strain sensors, ultrasound, acoustic emission, shearography, laser Doppler interferometry and photogrammetry. A number of the said measurement techniques form the basis of vibration measurement and analysis. As mentioned, acquisition of the information in the ways described allows the static and dynamic characteristics of the blade to be formulated; through signal processing and algorithms these characteristics may be represented as the blades loading capabilities, fatigue limits, material stiffnesses, resonant frequencies, mode shapes and frequency response functions (FRFs) that are compared to expected or historical values for condition assessment. The techniques mentioned are some of the more common methods and are described in numerous texts where specific detail on their application and use is discussed (Hameed *et al.*, 2009; Amenabar *et al.*, 2011; García Márquez *et al.*, 2012; Yang and Sun, 2013). The main purpose of this section is to get an idea of the CM and measurement techniques currently in use and to gain insight into the types of measurements made, what they measure, how they measure and their contribution to the CM of the rotor in terms of their fault detection capabilities.

Another important distinction amongst the various CM measurement and analysis techniques is the capability of identifying that there is a fault somewhere in the system (global detection) or being able to identify and isolate the location of an exact fault (local detection). This depends on the technique used, how it is employed and its limitations. Ideally one would want to monitor an entire system and be notified of the exact fault on a specific component such as the developments made in gear and bearing monitoring with vibration analysis. Very few CM systems have this capability, and the task of accomplishing this goal on rotor systems is difficult with the complexity associated with the material used, the structural dynamics and aerodynamics at hand.

The fact that helicopter and wind turbine rotor blades are made of composite materials has already been alluded to. Damage detection in these materials is not straight forward signified by the research dedicated to testing and modelling them. Studies on composite rotor structures suggest that damage can be detected by monitoring changes in the material stiffness, the tip response, blade root loads, rotational frequencies and the modes resulting from flap, lag and torsion in the blade (Pawar and Ganguli, 2007). Furthermore, it has been shown through the study of these composites that matrix cracking can be detected as a result of large changes in the peak-to-peak tip response, the loads experienced at the root of the blade and strains.

Amenabar *et al.* (2011) compare methods used to inspect wind turbine blades for delamination that occurs during the manufacturing process. They compare shearography, infrared thermography, ultrasonic and x-ray methods; demonstrating the effectiveness and shortfalls of each method for this purpose. These methods also have the capability of detecting small cracks. In a review on wind turbine CM, fault detection and their related algorithms by Hameed *et al.* (2009), the use of thermoelastic stress analysis to detect shear web disband, trailing edge delamination and cracks is mentioned; also the utilisation of ultrasound transducer patches to accurately detect damage in critical locations on the structure. In addition to some of the common measurement methods, they describe embedding fibre-optic strain sensors into material components of the rotor blade. Acoustic monitoring is said to have a strong relationship with vibration monitoring. Acoustic sensors measure sound directly and are attached to the component with a flexible glue as opposed to vibration sensors (such as accelerometers) which are attached directly to the component to measure its movement (García Márquez *et al.*, 2012). The generation and propagation of cracks in the blades manifest as acoustic emissions through the structure. Surface mounted sensors pick up sound waves radiated by the structure for the detection and location of damage. Even though a number of these texts are specific to wind turbines, similar use of the methods as applied to helicopter rotor blades are confirmed in the review on helicopter rotor CM by Pawar and Ganguli (2007).

Both Hameed *et al.* (2009) and García Márquez *et al.* (2012) make reference to performance monitoring of wind turbines as an indicator of the overall condition of the rotor system. Analysing the expected power output of the rotor for given wind conditions can indicate potential problems in the event of abnormal operation. Moreover, Pawar and Ganguli (2007) report usage monitoring of critical components, the components life cycle is determined as a result of documented history and time in service, along with any known damage it has endured.

Vibration based CM is one of the forefront techniques used in machine condition analysis receiving considerable research attention. Helicopters endure severe levels of vibration originating largely from the engines, main rotor, tail rotor, other rotating components and airloads. Vibration amplitudes measured at frequencies related to these components using accelerometers in the cockpit not only signify discomfort to passengers but aid in identifying the presence of a fault and the probable culprit (Stupar, Simonović and Jovanović, 2012). The method described may be useful in identifying when levels of vibration exceed ideal limits and the component primarily responsible for it but it does not give any information on the characteristic parameters of the blade which can be used to better understand the fault at hand.

Studies continue to attract researchers to vibration analysis in which state of the art measurement techniques are being developed to collect vibration data for the rotor blade itself in non-invasive ways juxtaposed to the traditional use of accelerometers. Ozbek *et al.* (2010) assess the feasibility of monitoring the vibrations and dynamics of large wind turbines using photogrammetry. Blade displacements are measured to which they exhibit the plausibility of frequency and modal analysis for wind turbine applications. Furthering the optical non-contact technique; Gwashavanhu, Oberholster and Heyns (2016) compare the vibration analysis of a rotating blade when using photogrammetry with that of tracking laser Doppler vibrometry. In their findings they reveal good correlation between the two optical methods with deviations from accelerometer results being due to the invasive presence of the probes on the blades. Recognising the potential of photogrammetry as a structural health monitoring technique, Lundstrom, Baqersad and Niezrecki (2016) monitor the dynamics of a helicopter main rotor using photogrammetry in a full scale test. They present results on the blade dynamics and extract operating deflection shape information for the helicopter with the intention that their work will lead to yielding full-field strain measurements to reveal strain amplifications and indicating damage. Changes in blade tip response have been noted as a means of detecting damage, the optical methods discussed provide valuable insight into this dynamic behaviour. This is confirmed in Pawar and Ganguli's (2007) review with laser Doppler vibrometers capable of measuring the tip torsional response over and above the height, lead and lag differences between the blades.

Imbalance:

Efforts in rectifying rotor imbalance may not be directly associated with finding defects in the rotor blade itself. However, it is still an important problem to solve since imbalance could be indicative of inherent damage in the blade in conjunction with relieving the system of any effect that imbalance has on the sub-systems connected to the rotor, such as the loads it transmits to the hub, bearing and drivetrain systems.

A method is proposed on identifying and correcting rotor imbalance in wind turbines by Kusnick, Adams and Griffith, (2015). The methods effort is placed in distinguishing whether the imbalance is caused by a mass or aerodynamic (blade pitch error) imbalance by using a combination of parameters which include the generator power signal and sensors mounted on the blades which return blade tip accelerations, root pitching moments and blade root axial force measurements. Making use of blade mounted sensors has the advantage of identifying the specific blade responsible for the imbalance.

Monitoring of the loads and vibrations transmitted to the rotor hub system from the blades will indicate blade damage. The hub is expected to experience loads at harmonics relating to the number of rotor blades per revolution (i.e. mN/rev) with damage or faults detected as increases in the one per revolution (and its harmonics) responses. This is true for both helicopter rotors and wind turbine systems as described by Pawar and Ganguli (2007) and Hameed *et al.* (2009), respectively. Singh *et al.*, (2008) use an aeroelastic finite element analysis to evaluate the effects of stiffness and mass imbalance on a helicopter tail rotor blade. The imbalances are modelled based on blade moisture absorption, stiffness and root damage where it is also observed that the one per revolution harmonic responses indicate damage. Interestingly, they conclude that hub loads from mass imbalances are primarily due to the mechanical imbalances whereas hub loads from stiffness imbalances are primarily a result of the aerodynamic forces. Stiffness imbalances may be described as the reduction in stiffness at the root due to damage in the flap hinge and pitch link bearings of helicopter tail rotor blades.

Dealing with helicopter rotor imbalances is referred to as rotor track and balance (RTB), this topic is dealt with in detail in the following sub-section. One detail to consider though is the fact that RTB is not only used to rectify the imbalances but also a number of the helicopter CM systems use it for the detection of blade damage. It shall be seen that these methods are ill-equipped to provide comprehensive information about blade health from the data acquired.

Other:

Literature which may not directly deal with helicopter or wind turbine rotor blades but bear relevance to this study are discussed here.

The effects of ballistic damage on the aerodynamic performance of airfoil sections were investigated by Robinson and Leishman as reported in Pawar and Ganguli's review paper. Parameters such as the lift, drag and pitching moment were studied where it was found that a reduction in lift and an increase in drag occurred due to the presence of the damage. Chordwise and spanwise pressure measurements were also taken to assess the three-dimensional aerodynamics of the damaged blade. Their study gives a take on the negative aerodynamic effects the airfoil succumbs to when damaged with Pawar and Ganguli referencing it as one of the only works that deal with aerodynamic properties under damaged conditions at that time.

Forbes and Randall, (2013) successfully estimate the natural frequencies of turbine blades from the casing pressure and vibration measurements which are realised through an analytical model as well as experimentally. Although this study is performed for gas turbines, they state that the primary source which dominates casing vibration in a gas turbine is the aero/structure interaction of the internal pressure and the turbine casing. This is of particular interest as they further stipulate that this dominant excitation occurs as a result of three constituents, quoted directly from their paper as:

I. Interaction of the rotating pressure profile around each rotor blade (noting that this is only the case for unshrouded rotor blade setups),
II. Propagation of acoustic waves inside the engine casing, and
III. Pressure fluctuations on the casing wall due to turbulent and impulsive flow.

The force dominating the excitation of the turbine casing are the pressure fluctuations described by the first point.

There might be a fundamental difference between the interactions for a shrouded and unshrouded rotor that exist due to the presence of the casing, but it is Forbes and Randall's description of the dominant factors which make up the pressure responses that is of interest. More so, the fact that the pressure signal retains diagnostic information

noting that the relation between the pressure signal and natural frequency of the blades is dominated by the content of a single faulty blade.

Acoustic monitoring has been identified as a measurement technique that is frequently used as a CM tool. However, traditional acoustic measurements are taken using single microphones (or other transducer types) at selected locations whereas newer implementations of acoustic monitoring make use of acoustic cameras which record the acoustic field radiated from the monitored machine using a camera and an array of microphones placed at a distance. This relieves the measurement system of being in contact with the machine, invasively recording data. Cardenas Cabada *et al.* (2017) demonstrate the use of acoustic imagery in diagnosing gear faults on a simple test platform. A beamforming method is used to extract time-varying signals of the acoustic radiations from the machine as a function of space, kurtosis is then used on the signals to extract impulsive features which can be analysed for fault signatures.

C. *Helicopter Rotor Track and Balance*

Similar to the discussion on imbalance in general rotors, helicopters experience large amplitude vibrations induced by the rotors at the same frequency as their rotation. Rotor track and balance (RTB) on helicopter rotor blades is the procedure followed in order to balance the blades, consequently resulting in a reduction of those major rotating frequency components of rotor vibration. In fact, vibration reduction throughout the aircraft can be considered as one of the primary objectives of RTB hence why the procedure is sometimes referred to as helicopter smoothing. Smoothing of the aircraft using RTB is effective because of the immense contribution rotor vibrations have on overall helicopter vibration compared to other components. Reduction of overall helicopter vibration is important as it negatively impacts human performance and component life (Renzi, 2004).

Rotor track is the path the blade follows through its rotation with the aim of the procedure being to ensure that each blade tip passes through the same vertical location, thus rotating through the same plane where the rotor is then said to be in perfect track. It is well known in the field of RTB that achieving perfect blade tracking alone may not result in vibration reduction. Even though this may not result in vibration reduction, it might be an effort of reducing asymmetric loading of the hub. It has, in any case, become an industry wide standard to evaluate the track at first during maintenance. The goal of rotor balancing is the correction of the mass and aerodynamic imbalances as alluded to in the previous section.

RTB is traditionally implemented using equipment to measure and record data for analysis, making adjustments to the rotor setup and the use of algorithms to make recommendations on the possible adjustments to acquire desired vibration levels.

Vibration sensors (such as accelerometers) are setup in the cockpit to measure the vibration levels encountered by the pilot, a tachometer is used on the rotor shaft to measure rotational speed and the relative positions of the blade tips are measured by a tracker with all the data being connected to and recorded by a data acquisition unit. The electro-optical method is used for rotor tracking where photographic images are taken of each blade tip during rotation and compared to one another to assess the relative track of each blade (Renzi, 2004). More sophisticated techniques are being developed which make use of photogrammetry, for instance, for blade tracking and characterisation.

Alterations made to the rotor system for RTB include the addition or subtraction of weights, adjustment of the pitch control rods or adjustment of the trim tabs. Each blade has a pitch control rod which is used to enforce blade pitch allowing the individual adjustment of angle of attack. Locations at which weights can be added to rotor blades are included during the manufacturing of the blade for the purpose of RTB. Trailing edge

trim tabs function as a camber change also yielding extra surface area on the blade allowing for increased lift and are manually bent to realise aerodynamic changes. These elements are represented in Figure 1-11.

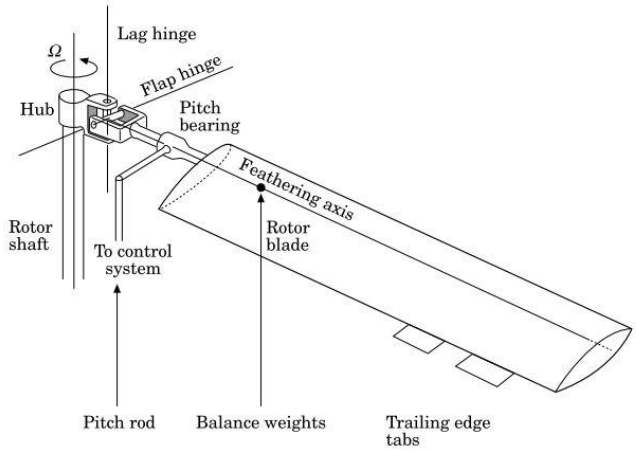

Figure 1-11: Representation of track and balance elements for a rotor blade. Taken from Rosen and Ben-Ari (1997).

The procedure followed in order to approach a tracked and balanced rotor is described by Renzi, (2004) as follows:

- The blades are statically balanced with weights and a jig with load cells using the chordwise and spanwise moments as criteria.
- Pitch control rods are adjusted to obtain perfect tracking on the ground.
- Whilst on the ground, the vibrations are checked and brought within acceptable limits for flight and safety.
- Test flights are performed at selected test speeds, which represent the helicopters typical use, to record vibration data for the flight modes.
- An algorithm is used to assess the vibration data and recommend adjustments to smooth the helicopter.
- Iterations of the outlined procedure are performed. Idealistically, smoothing is achieved in as few a number of iterations as possible due to the expense and time required.

The procedure described above was mathematically modelled by Rosen and Ben-Ari (1997). Their model indicates adjustments to the blade mass, pitch control rod and trim tab based on measurements from an optical sensor and accelerometer vibration measurements. Interestingly, in Ben-Ari and Rosen's (1997) second of their sequential papers on RTB, they state that adjustments to the pitch control rods and trim tabs should be considered as the elementary corrections to be made due to their effectiveness with blade mass additions being secondary for fine tuning.

Helicopter rotor blades are problematic to balance due to the numerous conditions they are exposed to. If RTB is optimised for a single flight mode, the vibrational characteristics will prove to be unfavourable in other flight modes. RTB algorithms try make a compromise such that acceptable levels of vibration are experienced over a number of flight modes (Ben-Ari and Rosen, 1997; Renzi, 2004). RTB algorithms are comprised of two categories which are learning and non-learning. Non-learning algorithms suggest adjustments based on a heuristically populated database of the helicopters response to adjustments. A learning algorithm is similar but the database is updated so that the algorithm can develop into giving more accurate recommendations. According to Renzi (2004), the current equipment, algorithms and procedure implemented do work when used properly by the diligent maintainer. Bechhoefer, Fang and Garcia (2014), on the

other hand, believe that there is room for improvements in the execution of RTB. They state, RTB algorithms have seen inadequate development due to limited availability of data sets to work on and the lack of an adequate basis to quantify new algorithms. They present a methodology to simulate the rotor vibration which occurs in the presence of a fault and suggest metrics to evaluate algorithm performance. One might also consider the fact that even though RTB is mathematically modelled in various ways, the databases used in RTB procedures are based on heuristic data. This implies the need for more advanced modelling which may encourage improvements in all aspects of RTB.

Current RTB research and development is being performed to make use of responsive components such as active trailing edge trim tabs and active pitch control rods that can adjust during flight. This is in an effort of alleviating the issue caused by employing a single rotor setup that has to find a compromise for all flight modes, with the vision that smooth operation will be encountered through all flight regimes due to in flight tuning. This advance in RTB may produce much lengthier life spans of the aircraft overall as one blade setting is not expected to suffice for all regimes, but it is still in active development and implementation. One can also expect that the implementation of such a system will be expensive and require extensive safety testing and maintenance.

Pawar and Ganguli (2007) believe that there is a fundamental difference between rotor CM and RTB since RTB sets out to minimise the vibrations caused by rotor imbalance while rotor CM attempts to assess the structural integrity of a blade and isolate the damage. However, since vibration monitoring is an integral element in the execution of RTB, it is not uncommon for the vibration data to be used in identifying potential rotor damage. By virtue of the manner in which the data is collected, it will only allow detection of some form of global defect. The increased vibration levels might signify imbalance to be rectified by RTB or may be indicative of damage with further investigation required to distinguish between them. Although, one might acknowledge that if blade tracking cannot be corrected by the described RTB procedure, blade damage is present.

1.2.5 Rotor Blade Modelling

Rotor modelling is by no means a new field in research, it holds an extensive background in which investigations have made considerable progression in model accuracy and representation of particular phenomena. The modelling and understanding of the structural behaviour exhibited by rotors and the fluid behaviour in the vicinity of the rotor have received attention, both individually and through their coupled interaction. Whilst in rotation, the behaviour of the flow around the blades may cause structural responses such as deflections and rapid vibrations of the blades, which in turn may change the flow field and so the cycle may commence. The interaction between the flow and the structure is termed Fluid Structure Interaction (FSI). The effects of FSI make rotors susceptible to aerodynamic induced loadings and other aero-elastic effects which leads one to think that such effects may need to be modelled if accurate results are to be obtained.

A number of studies in the field of rotor simulations are dedicated to making numerical advancements and developing the modelling accuracy from both a structural and aerodynamic perspective. When modelling FSI, aerodynamic loads and behaviour are determined using CFD and structural response is determined using FEA (Finite Element Analysis), requiring a good understanding of both codes. A model setup of this nature represents reality to an advanced degree but the coupling and convergence of these two analyses can be computationally expensive. The fact that there is so much research dedicated to the problem of rotor modelling (particularly helicopter rotors) may be indicative of the difficulty of the problem. Furthermore, this indicates the lack of a definitive model which can accurately predict the several complex phenomena which include the wakes, dynamic stall, compressibility and shock interactions, reversed flow, all flow regimes, unsteady flow, blade vortex interaction (BVI – the interaction of the

vortices produced by each of the helicopter rotors) as well as a fair representation of the structural dynamics of an articulated blade from FSIs, rigid body motion and deformations. In fact, certain instances of the phenomena mentioned are specialist fields and have uncertainties and complexities of their own which prohibit their successful modelling.

Some authors express that helicopter rotor blades need to be modelled with a full aero-elastic coupling as a result of the FSIs, flow phenomena and rotor motions (Conlisk, 1997; Yu, 2000; Potsdam *et al.*, 2004; Wagner, 2005). The requirement for the level of accuracy produced in FSI modelling needs to be justified against the computational expense and difficulty in modelling it correctly. Bramwell, Done and Balmford (2000) indicate that much of helicopter theory can be deduced when one regards the blade as rigid and understanding the underlying assumptions made to implement such simplifications. This is supported by Conlisk (1997) who also mentions that due to the complexities which present themselves when modelling rotors, investigations need to be well targeted in scope so that significant simplifications can be made in order to focus on specific aspects of the flow.

In consideration of studies which are scoped to understand the aerodynamics related to rotors, Pandey *et al.* (2012) conducted a numerical simulation on a helicopter rotor blade in a way that is similar to how the simulations are carried out in this study. They performed a single CFD simulation on an isolated helicopter rotor blade for a specified rotational speed and angle of attack said to represent hovering flight conditions. The MRF rotational model and the standard k-epsilon turbulence model were used for the simulation. The only objective of their study was to analyse the flow around the rotor for these conditions where comments are made on the presence of the vortex sheet in the plane of the blade and the concentrated tip vortices.

Aerodynamic analysis can be completed through experimentation and visualisation, this also allows the validation of numerical results. Interferometry has been used to study aerodynamics around rotorcrafts with specific attention to characteristics such as dynamic stall, BVI and transonic flow on a rotor blade (Carr and Yu, 1992). The interferometry methods presented capture and quantify the contours of the flow field under the specified blade conditions based on the principle of light refracting differently through changes in density of the fluid. Recently, studies into the use of fast-response Pressure Sensitive Paint (PSP) for the quantification and visualisation of unsteady aerodynamics has gained momentum such as the work of Gardner *et al.* (2014). They investigate three-dimensional dynamic stall on a pitching airfoil using PSP at Mach 0.3 and 0.5 demonstrating the potential advantage of using it over pressure transducers for a complex three-dimensional flow. Disotell *et al.* (2016) illustrate the use of PSP to obtain global surface pressure measurements of static and dynamic stall on a wind turbine airfoil at a low Reynolds number. Weiss *et al.* (2017) measure global surface pressures on fast rotating blades and prove its resolution as being comparable to pressure tap data to within 250 Pa. These few texts give an indication of the potential in which PSP could be used, with the field still growing and other work demonstrating its applications, developments and shortcomings with particular interest on those testing and experimenting on rotating, helicopter and wind turbine blades.

Rotor models which focus on the accuracy of the modelling, in terms of the prediction of flow phenomena and performance parameters, as well as some experimental flow visualisation have been introduced. Literature considered have been based on modelling methods which shall suffice in representing the necessary flow patterns to obtain the required data with adequate accuracy. Simulations which consider faulty conditions and the identification thereof are more in line with the intended work. Identification of defects by observing changes in simulated results using models with seeded faults can be very beneficial. Not only can it be safer and cheaper, but the

models present an abundance of data on which algorithms and detection strategies can be tested and optimised before implemented in the field. In particular situations, CM systems may be developed through a model but are fine-tuned using parameters from actual service data (Pawar and Ganguli, 2007).

An aero-elastic analysis based on finite elements is used to mathematically model structural damage, blade mistracking, friction and freeplay of a helicopter rotor system by Ganguli, Chopra and Haas (1998). Damaged or mistracked blades are modelled as changes in stiffness, inertial and aerodynamic properties. Rotor faults represented include chord wise imbalance, aerodynamic mistracking, localised cracks, stiffness defects, manufacturing defects, friction and freeplay in the pitch-control system and the lag damper, and friction in the flap and lag hinge. A number of the faults modelled could be identified by the monitoring of the flap, lag and twist (torsion) responses. Conclusions are also drawn to the effect of the defects on the hub response. Another major topic is the use of FEA studies on composite materials to better characterise their structural properties. FEA model updating is performed based on experimental results so that accurate models can be developed. Better models predict structural characteristics such as fatigue, natural frequencies and mode shapes better so that their changes in the presence of faults can be studied (Yang and Sun, 2013). Other studies that model rotor faults and suggest such detection strategies are summarised in Pawar and Ganguli (2007). The reader is directed to those references for more detail as the studies shall not be described elaborately in this report. They bear resemblance to the work discussed above with many of them using mathematical and finite element models to acquire structural responses for particular defective cases. Majority of which conclude that faults are identified by monitoring tip response and hub response in the form of vibrations described by imbalance.

A CFD analysis on a Vertical Axis Wind Turbine (VAWT) under fault conditions consisting of missing blades is considered for CM by Park, Asim and Mishra (2012). They monitor VAWT output performance noting a significant degradation as blades are removed. Oggiano *et al.* (2016) use URANS CFD to model a Horizontal Axis Wind Turbine (HAWT) with a single blade off-pitched to emulate imbalance and for comparison with experiments. They discuss the effect of off-pitched blade on the torque and axial force experienced by each blade as well as the rotor in total and also report a drastic decrease in output performance with the fault. Also, they compare the pressure distribution on the blade directly behind the faulty blade using the simulation results and pressure taps data from the experiments. They determine that as the wind speed increases, the effect of the faulty blade on the aerodynamics of the other blades is reduced due to the wake being convected away. Another study which uses performance output to monitor rotor condition is completed by Allmark (2016). This study considers a CFD analysis on tidal stream turbines with off-set pitch blades to simulate rotor imbalance faults to develop condition monitoring and fault diagnosis techniques.

As a consequence of fluid interactions, acoustic analyses and noise generation are studied allowing one to delve deeper into the exploration of aerodynamic behaviours. Strawn and Biswas (1996) simulate aerodynamics and acoustics of a helicopter rotor blade. Their analysis is performed on a non-lifting (zero pitched) rotor to match experimental data. Good agreement is found for the in-plane acoustic pressures (impulsive noise) generated by the blade between the experimental and simulated results. Li *et al.* (2016) study the effects on the performance and aeroacoustics of an axial fan when there is a blade with an abnormal angle (different pitch to the other blades). They observe the abnormal blade to cause a degradation in fan performance and a rise in aero-acoustic noise simulated with a 3D LES model. The study is performed for a fan under shrouded conditions where the noise is produced as a result of the interaction between the tip of the fan and the case wall where assessments are made on the effects of the tip clearance, the tip vortex and tip leakage on the noise and

performance. Although their motivation for studying the noise generated by the fan is due to the detrimental effects it has on nearby workers, their results illustrate the ability of fault detection from aero-acoustic noise. This serves as justification for more studies to be done to investigate aerodynamic and noise behaviour with faulty components. These are but two examples of simulations based on noise. Aero-acoustic simulations are another specialist research field which is introduced here to allow the reader to consider the applicability of aerodynamics and noise for fault detection and the capability to model it.

1.3 Scope of Research

Based on the many facets which present themselves in the context of this study that have been identified and presented in the elaborate literature study, the scope of research needs to be described in detail. This section presents a motivation for the work based on gaps identified in the literature which are then broken down into a set of objectives. To define clear bounds of what will and will not be considered in this investigation, research specifications, simplifications and assumptions are detailed.

1.3.1 Motivation

The literature on condition monitoring clearly illustrates the dominance that structural response and analysis possesses for rotor monitoring and diagnostics. In particular, the prowess that vibration based condition monitoring possesses in identifying the structural integrity of machines and their components is exemplified. It would be naïve to think that most defects would not show up in this way since defects emerge as changes in structural characteristics, which until today, have been easy to measure, quantify and compare. However, for the rotors to be considered, the dependence of the structural response on the aerodynamic response as a result of their interaction has been indicated; implying that fluid behaviour may carry information about the dynamic characteristics of the rotor because of their interaction. Even in the situation where these effects are minimal, some faults may exist which have an influence on the fluid. It is also the case that condition monitoring systems are under continual development since current systems are incapable of monitoring every component of a system, identifying any and all types of abnormalities and then isolating the problem. Implying that techniques which consider condition monitoring from a different perspective which have the potential to adequately detect faults that may not be well resolved by other methods could make a valuable contribution.

It is also true that much of rotor based modelling is lopsided such that it is purely focused on model accuracy and, in most cases, is without the introduction of the faults that may be typical of a rotor. Many studies model the structural behaviour of rotors for structural characterisation for model updating to improve numerical predictions. Similarly, of the studies which consider fluid behaviour, an overwhelming number focus on modelling performance parameters accurately such as drag, lift, torque and vortical structures. Pertaining to fluid models which do investigate faulty conditions, missing blades and off-pitched blades appear to be the main fault conditions considered where, to the authors' knowledge, there are no studies which consider helicopter rotor fault modelling using CFD. This may be a result of the various flow phenomena, structural phenomena and external interactions the blade is exposed to, making it difficult to model. It is also important to note that of the fluid models conducted under faulty conditions, most investigate monitoring of the power output performance for fault detection.

The work of Forbes and Randall (2013) and Li *et al.* (2016) where pressure signals are used to estimate blade natural frequencies and aerodynamic noise is used to detect an off-pitched fan blade, support arguments that the fluid carries diagnostic information about the rotor when in operation. These studies considered a form of rotor that was in

a shrouded environment where both observe the contribution the casing has on the flow. This study is different as an unshrouded rotor will be considered. The benefit of developing a fluid based diagnostic approach is that the technique may be capable of detecting faults that cannot be picked up by structural approaches, specifically when in operation. This will also benefit imbalance detection in distinguishing whether it is mass or aerodynamic. For instance, rotor imbalance induced aerodynamically is not a structural issue and could be detected with ease from the flow field. Furthermore, it is anticipated that the type and degree of aerodynamic imbalance could be distinguished based on the fluid behaviour, such as the detection of yaw or pitch faults in wind turbines or identifying a pitch or tab adjustment on helicopter rotors.

Great value comes of performing the investigation through modelling. First and foremost, modelling is safer and cheaper as it is dangerous and expensive to damage rotor blades for experimental investigations. The literature states, particularly in the field of helicopter rotor track and balance, that there is a lack of data for testing of strategies. Databases of simulated signals provide an abundance of data which allow the optimisation of acquisitioning locations and algorithms. Also, simulations provide physical insights to the dynamic behaviour of the modelled media leading to how different faults express themselves (Madar, Klein and Bortman, 2019).

As further support for the proposed study, Pawar and Ganguli (2007) are quoted as follows: *"…so much attention has been given to algorithms for damage detection in recent years, it is necessary to bring the focus back on accurate physical modelling of damage and the use of more sophisticated aero-elastic analysis models such as those incorporating computational fluid dynamics*." This is in response to the lack of a definitive rotor damage detection technique for helicopters as currently vibration results for RTB analyses are used to signify possible damage.

The aim of this study is to use CFD to model a simplified rotor blade that ordinarily is unshrouded and investigate the feasibility of inferring a seeded fault from its fluid dynamic behaviour. The problem may be approached in a simplified manner, even to the point where the current analysis performed may be impractical in reality. But the point is to generate a model that allows one to understand what is happening to the fluid and aerodynamics as well as assessing the feasibility of detecting the fault based on these occurrences.

The eventual goal is that if a fault can successfully be detected purely based on the flow phenomena, having models which describe the aerodynamic and fluid properties in the presence of a fault allows an understanding of anomalous behaviour. It is anticipated that this may lead to detection techniques that use measurements of pressures on the rotor, in the field of the rotor or from abnormal acoustic (aerodynamic) noise generated. Acquisition may take the form of, for example, the use of pressure sensitive paint (PSP) or monitoring with an acoustic camera.

PSP studies demonstrate its use in visualising and thus quantifying the unsteady aerodynamics along with the ability to obtain global pressure measurements which occur on a rotor blade. If one can model the rotor as well as seeded faults along the rotor and identify the flow characteristics and possible trends, it may be possible to visualise in this way. The model provides the basis under which certain fault mechanisms may be identified.

Implementing these detection techniques would be non-contact and non-invasive. Depending on the effectiveness of the modelling, future detection techniques that use flow field data could also be passive, meaning that they will not require pre-damage data as the model will suffice in signifying abnormal conditions or the detection could be done by comparison of the features with other blades in the system.

1.3.2 Objectives

The objectives of this study are stated as follows:

- Assess the feasibility of detecting a rotor fault from flow field data
- Gauge the suitability of using CFD to model a simplified helicopter rotor setup
- Demonstrate the use of simulated pressure transient data for fault detection
- Comment on the sensitivity of fault detection locations in the field
- Compare the effectiveness of fault detection on the blade and in the field
- Mention any notable flow field change in the presence of the fault for future detection strategies
- Provide a basis on which further studies can be developed to progress CM strategies

1.3.3 Research Specifications, Simplifications and Assumptions

With the question posed as to the detection capabilities from fluid responses, one cannot solve all the complexities associated with the topic. Thus a detailed description of this study's inclusions is required. This study's focus will not be on the development of a detection algorithm nor will it be on signal processing. Some form of signal processing and analysis will be conducted but it is understood that there are more sophisticated techniques that could be used and that may be more appropriate, efficient and accurate which are left for future work. A question on general rotor fault detection from the flow information is to be answered but the problem has to be deduced in some way. A description of the type of rotor class, fault mechanism and the way in which the modelling will be formulated is discussed.

A. *Rotor Definition:*

Up to this point, the rotors discussed for investigation have been fairly general under the agreement that they are unshrouded. It may be that at some stage, the findings of this work could be applied to a broader spectrum of rotors which include shrouded rotors. But the priority is to deal with rotors which do not have casing interactions and as such the full field of flow is available. This presents problems in the dynamic monitoring of their blades and data acquisitioning. One might consider the following categories for unshrouded rotors: fans, propellers, helicopter rotors, wind turbines and water turbines. These are summarised in Figure 1-12 below.

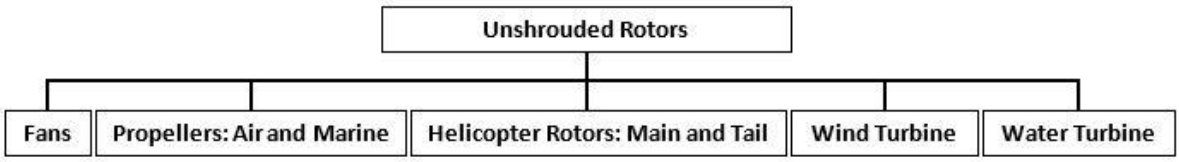

Figure 1-12: Unshrouded rotor classes

Fans, propellers and water turbine blades are generally rigid whereas helicopter rotor and wind turbine blades are made of composites. Due to the material and slender construction of helicopter and wind turbine rotors, they exhibit FSI more than the other classes and exhibit increased difficulty in performing damage detection due to the composite materials.

A helicopter tail rotor blade is used in this investigation. The availability of a test bench with a helicopter tail rotor makes it possible to conduct an experimental investigation to gather information for validation of the rotor simulations. It is advantageous to model the tail rotor, as opposed to the main rotor, since it allows considerable reduction in the complexity of the problem. The structural behaviour is less pronounced than for a main rotor allowing a reasonable comparison between the experimental and numerical

results. From a fluid dynamics perspective, it is interesting to note that the tail rotor may suffice in representing some of the phenomena of the main rotor due to them having comparable linear velocities. The ratio of the speeds at which the two rotors operate is inversely proportional to the rotor diameters producing similar linear velocities along the blades. This should not be confused with the overall function and phenomena on the blades though, as the main rotor is cyclically pitched in forward flight and will encounter severe structural behaviours as mentioned.

B. *Fault Definition:*

At this stage it is not expected that finer defects and faults such as cracks, fibre breakage, minor delaminations and de-bonding will be detected in the flow field, specifically with the modelling used. But it is expected that faults that pose as geometrical changes can be detected. Blade geometry deviations may be represented by dirt, icing, erosion, off-pitched blades, severe trailing edge delamination's and imbalance.

The intention is to consider a simple geometric fault that is pronounced so that the plausibility of the problem can be satisfactorily determined. With this in mind, rotor tracking of the helicopter blade will be considered. This allows for a simple enough geometric change as a single rotor can be rigidly displaced in the model to observe the effect on the flow while ensuring that the problem considered is of a realistic nature. In other words, the fault mechanism simply provides a practical example on which to base the feasibility study.

Modelling using URANS and without a full aero-elastic coupling will not allow for any form of vibration prediction which is a primary concern of RTB. This also prohibits the observation of tip responses which have been identified in literature as a means of assessing damage. Consideration of the fault in this sense may contribute to rotor imbalance detection as aerodynamic contributions to imbalance can be quantified from their asymmetries. It is not within the scope to develop an algorithm but the results may be ground on which to formulate other investigations. One idea might be to do a parametric study on pitch and trim tab adjustments and their aerodynamic loading effects on the hub as well as the fluid dynamic information to make the adjustment recommendation. This investigation serves as a premise for conducting such a study. Even though vibrations are not considered nor the accurate response of the blade adjustments due to FSI, it may have a valuable contribution to RTB algorithms and the formulation of physics-based models over the current data driven algorithms.

C. *Modelling Definition:*

Even though a full aero-elastic model expresses the FSIs between the blade and the fluid and thus realistic conditions more accurately, it has been identified in the literature of Section 1.2.5 that computational expense can be reduced considerably whilst maintaining reasonable accuracy by neglecting this level of modelling. Using fluid dynamic behaviour, modelled with CFD, to infer evidence of a blade geometry change is the main objective. The rotor will be modelled as rigid permitting a pure fluid dynamic investigation to accomplish this objective. It is understood that neglecting structural responses through a full FSI coupling limits the study of rotor fault detection through behaviour such as the tip response described in literature. It is assumed that such influences on the fluid dynamic behaviour are negligible on a helicopter tail rotor blade in comparison to the geometric deviations to be considered.

It is not this study's purpose to measure aerodynamic airloads on the helicopter or rotor performance parameters nor model them accurately. Rather, some analysis is to be performed of fluid dynamic properties which can be measured in practice in the presence of a geometric fault. For this reason unsteady RANS turbulence modelling will be used. RANS is known to serve most industrial applications as it is robust and provides

reasonable accuracy and fair computational expense. The higher levels of turbulence modelling serve more accurate studies with better representation of the turbulence properties. A dynamic mesh shall be used to simulate the rotational domain where investigative studies will be done to select models which represent the turbulence, compressibility and flow regimes along the blade. Transient data shall be captured from within the domain of the rotor but the rotor will be considered at its fixed operating speed thus neglecting start-up effects when simulating.

Tail rotor blades are described as experiencing a number of interactions in reality. In order to reduce complexity for the purposes of this study, the rotor shall be modelled as an isolated entity. No external interactions will be considered, the rotor shall be simulated in rotation with interactions as it rotates through its own wake.

There has been some mentioning of the use of acoustic information, such an analysis will not be considered in this investigation. This was brought forward due to the relationship it has with the flow field; an analysis of aerodynamic and pressure trends may be related to acoustic manifestations. This is in addition to the existence of current acquisition techniques acoustics provides and for the consideration of future diagnostic methods with the information of this study as grounds.

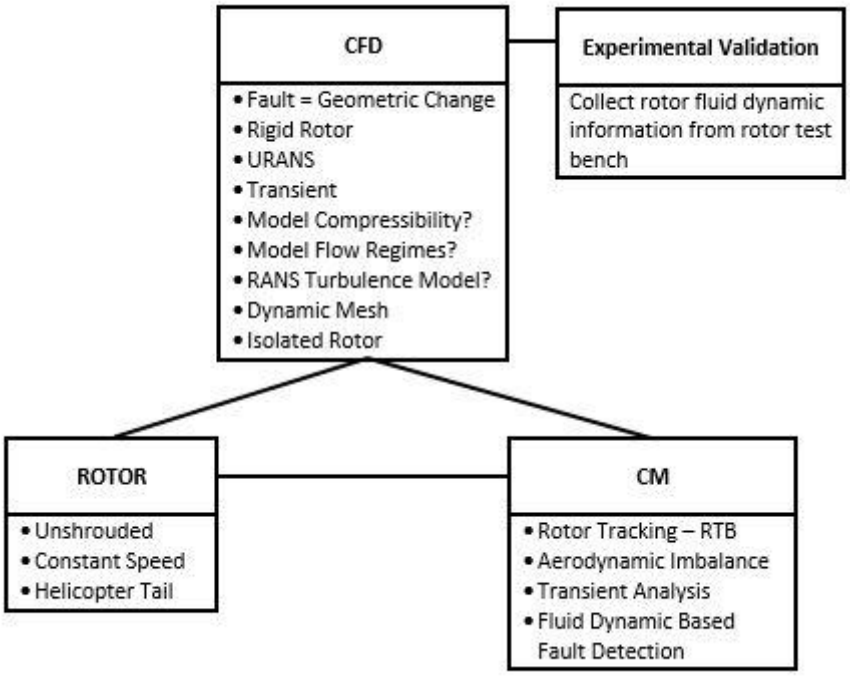

Figure 1-13: Summary of scope

Figure 1-13 provides a summary of the scope of the investigation, defining specifications for each field encompassed within the investigation. Sections 1.3.3.A to 1.3.3.C consider and motivate the choices made for the type of unshrouded rotor, the fault mechanism and some of the numerical modelling that shall be performed. In summary this study will consider a simple rotor to explore the extent to which rotor faults would change the flow field around a rotor and how these changes could be used for rotor fault detection. Helicopter rotor monitoring is commonly done through vibration analysis with accelerometers in the cockpit to identify the effects of the blades on the cockpit when in operation during RTB procedures. But, this monitoring does not give insightful information about the rotor behaviour and simply focusses on the mechanical impact the fault propagates without actually identifying the fault mechanism or its location.

Through this study an experimental investigation is done on a helicopter tail rotor as a representative but simpler rotor. This is done in order to understand the nature of the flow phenomena that are present as well as to use the fluid dynamics information acquired to validate the numerical investigations. The experimental investigations are not purposefully performed under faulty conditions due to safety concerns. Following the experimental studies, numerical validation and investigative studies are performed on simpler 2-dimensional cases to explore various modelling assumptions which are not defined in the above scope of work. These investigations include mesh convergence studies and the selection of a wall function, a RANS turbulence model and an appropriate solving application. Finally, a perfect tracking and a mistracking simulation will be compared to examine fluid dynamic changes. These will be considered in the perspective of fault detection for CM so that the feasibility on rotor fault detection using fluid dynamic information can be concluded.

1.4 Chapter Summary and Document Overview

An in depth discussion on the fundamentals in fluid dynamics was covered due to the need of having a sophisticated understanding of the fluid flow and phenomena which may occur. Various aspects around CFD were then introduced where attention was given to the various levels of modelling and the considerations that may need to be made. The highly complex nature of helicopter rotors in motion was addressed where attention should also be given to the conclusions in the difficulty of modelling such behaviours.

Rotor condition monitoring, with specific attention to wind turbines and helicopter rotor blades, was studied in light of the faults they incur and current monitoring and detection techniques employed. Attention was drawn to the fact that, fluid dynamic information may carry diagnostic information about the rotor and is not well represented in literature unlike the several structural approaches. The reader was informed on the availability of a tail rotor blade which forms the object of this study. The rotor blade shall be modelled using CFD under healthy and faulty conditions, the fault is imposed geometrically representing a mistracked blade. The flow field will be studied to assess the ways in which the fault can be inferred from it.

Chapter 2 presents an experimental investigation conducted to gather fluid dynamic data using a helicopter tail rotor blade test bench. The data is collected, processed and analysed. This is done for comparison and validation of the healthy rotor simulation conducted in Chapter 4.

Chapter 3 describes a number of numerical validation and investigative studies. These are conducted on simpler 2D cases to explore modelling assumptions and test these assumptions against results from literature. The studies provide guidance such that the most appropriate modelling parameters are selected to setup the simulations of Chapter 4.

Chapter 4 describes the simulations of the rotor blade performed where a healthy and faulty blade are explored. The results are processed and analysed to aid in the detection of aerodynamic imbalance.

Chapter 5 presents the conclusions, limitations and recommendations of the investigation.

Chapter 2 – Experimental Investigation

Experiments were conducted in order to collect data which shall be used for comparison and thus qualitative validation of the data produced by the simulations of the helicopter rotor blade. This allows the simulations to be assessed on a realistic basis. It also allows the study to emulate a scenario of measurement techniques which provides a better understanding of what is physically possible to measure. This chapter describes the rotor blade that was used, the experimental setup as well as the data that was captured along with certain restrictions and assumptions that were required in order to complete the collection of data.

2.1 Tail Rotor Blade

Picking a tail rotor blade as a representative of the problem at hand is beneficial as it presents a realistic ground around which to base the study as well as provides a reduction in the complexity of typical structural motions and fluid dynamic phenomena when compared to a main rotor. Additionally, basing the investigation around this rotor blade allows the geometry to be accurately modelled as it can be measured if unknown.

The tail rotor selected comes from an AS350 helicopter (both the B2 and B3 variants) with part number 355A12-0040-08. Table 2-1 gives some of the specifications of the tail rotor blade which were taken from the systems manual used by helicopter technicians. It is stipulated that the airfoil profile used in the design of the blade is the NACA 0012 airfoil. The NACA 0012 airfoil is a part of the four digit series of airfoils where the 00 designates the camber (symmetrical in this case) and the 12 designates the maximum thickness which is the percentage of the chord length (i.e. maximum thickness = 12% of chord length). It should also be noted that the maximum thickness of the airfoil occurs at 30% along the chord length (Airfoil Tools, 2017).

Table 2-1: Specifications of helicopter tail rotor blade

Composition of tail rotor	Composite materials
Total weight (without rod)	6.8 kg
Actual chord	185 mm
Locally in the tab area	205 mm
Rotor diameter	1860 mm
Symmetrical airfoil profile	NACA 0012
Theoretical twist	0°
Wedging of strap in torsion area	10°
Pitch axis rotation	37 mm from leading edge
Number of blades per rotor	2
Rotational speed (max. regulated)	2147,3 tr/mn
Rotational speed in autorotation	2472.8 tr/mn
Power	1140 kW
Maximum thrust	2630 N

Other specifications of interest are the theoretical twist which defines how the blade twists as one moves radially outwards from the centre of the blade where it can be seen that this is zero, indicating that the blade profile is straight through its length. Figure 2-1 summarises the overall dimensions of the rotor blade in a simplified sketch.

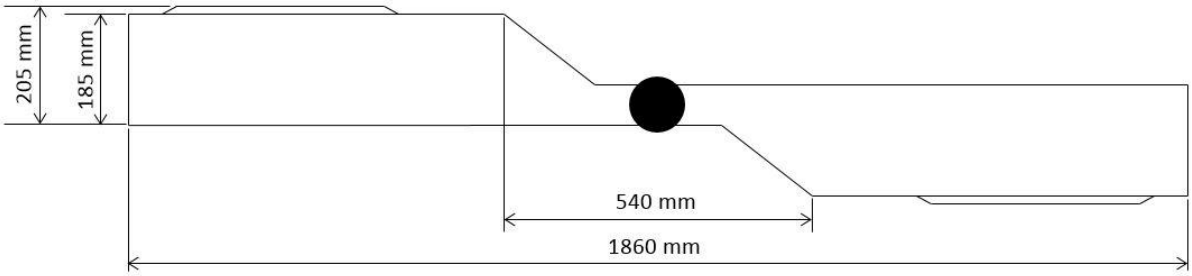

Figure 2-1: Overall dimensions of tail rotor blade

2.2 Experimental Setup

The experimental investigations of Xu and Amano (2002) and Xu, Amano and Perez (2002) were used as a basis around which to formulate the experimental work considered in this investigation. In their investigations, unsteady pressure field measurements of an axial flow fan were taken on the blade and at the inlet and outlet of the fan using a rake of transducers, respectively. Taking measurements on the blade requires more sophisticated equipment and setup time increasing the complexity of the procedure which is undesirable for condition monitoring purposes. Flow field measurements were taken in the field of the rotor at specific locations which is simpler and more practical. This represents measurements taken at stationary points in the field or at fixed locations on the helicopter.

The helicopter tail rotor blade was attached to a shaft which had a sleeve to control both blade pitches uniformly. The shaft was positioned by two bearing houses. A 7.5 kW electric motor powered the shaft through a belt and pulley system, as shown in Figure 2-2. Zebra strips were pasted on the shaft that were read by a laser tachometer to determine the speed of the shaft, shown in Figure 2-2 and 2-3. The power supplied to the electric motor could be controlled which adjusted the speed of the rotor.

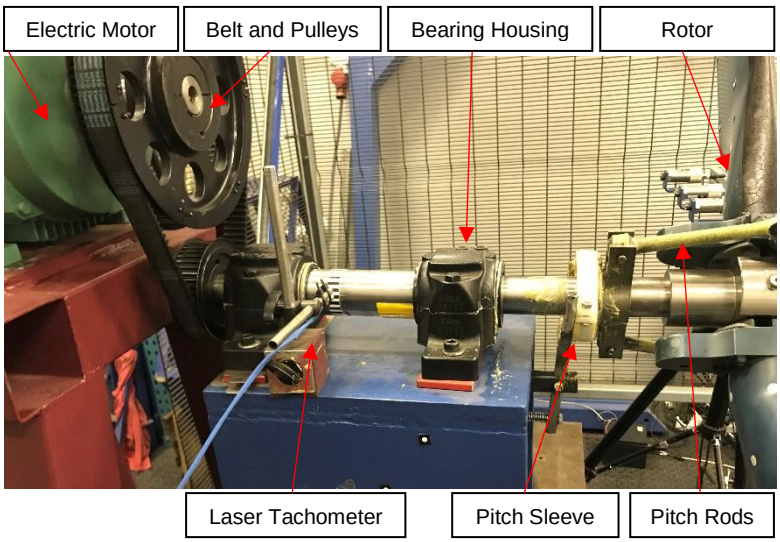

Figure 2-2: Rotor shaft setup

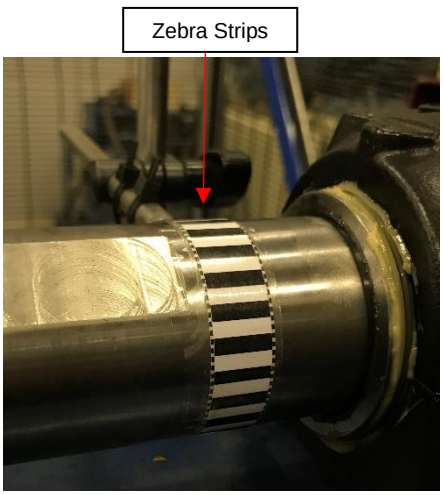

Figure 2-3: Laser tachometer zebra strips

The pitch of the blade was measured by placing a tilt sensor (inclinometer) at 30% of the chord length of the blade. This position was selected as it is the position which has the maximum height along the chord and should be parallel to the chord line of the aerofoil, thus expressing the blade pitch.

Three WIKA P-30 pressure transducers were attached to a frame to form a radial rake of measurements. The transducers were positioned at radial distances of 67%, 80% and 100% of the rotor radius, i.e. 620mm, 744mm and 930mm (at the tip) from the centre of the rotor.

The stand for the rake was then positioned such that the pressure probes were parallel to the blade and perpendicularly placed at a distance X, shown in Figure 2-5. Marker X in Figure 2-5 was measured from the trailing edge of the blade (the chord line when using zero pitch) to the opening of the WIKA sensor for pressure measurement. Values of X for which data was captured were 20mm and 100mm, producing a total of 6 time-dependent pressure measurements. The setup of pressure transducers are shown in Figures 2-4 to 2-6.

Figure 2-4: Positioning of pressure transducers

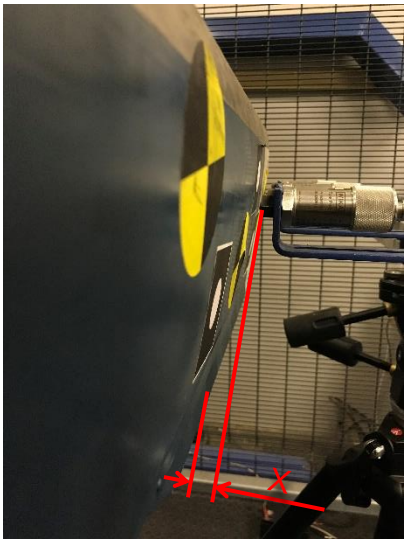

Figure 2-5: Perpendicular distance of pressure transducers from rotor

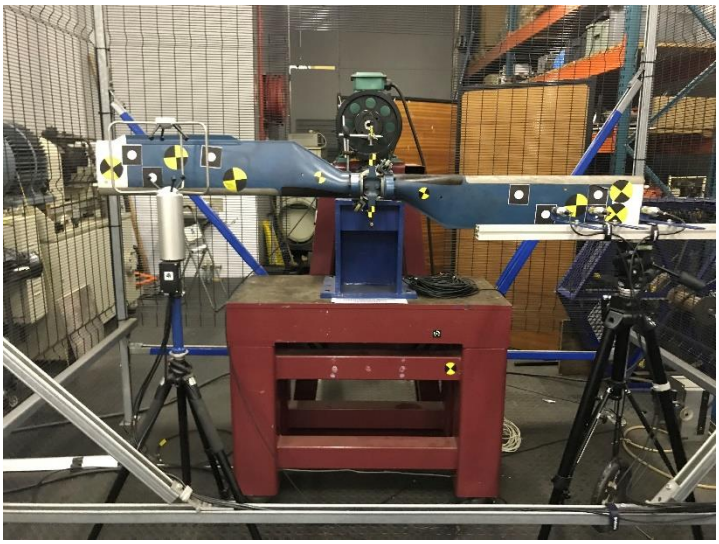

Figure 2-6: General setup around rotor

Finally, Figures 2-6 and 2-7 depict the overall setup for the experiments. The positioning of the transducers can be seen in both of these. Figure 2-7 shows the power supply used to provide the transducers with power. The data acquisitioning unit is an all-in-one kit which is equipped with a computer, screen, mouse, and keyboard and accepts the channels from the different equipment. The tachometer and each of the three pressure signals were wired to this for data acquisitioning.

To collect data, the transducers were placed in their appropriate locations and the rotor was spun manually to ensure no collisions would occur along with a few other safety checks. Power was supplied to the rotor to witness a slow rotational speed. Once all was in order, the data acquisition unit was set to record at 19.2 kHz and the power to the rotor was ramped up from another room for safety reasons. Power was ramped until the maximum capacity of the motor was reached where recording continued for a few seconds to acquire steady conditions. The power was then cut and recording was stopped.

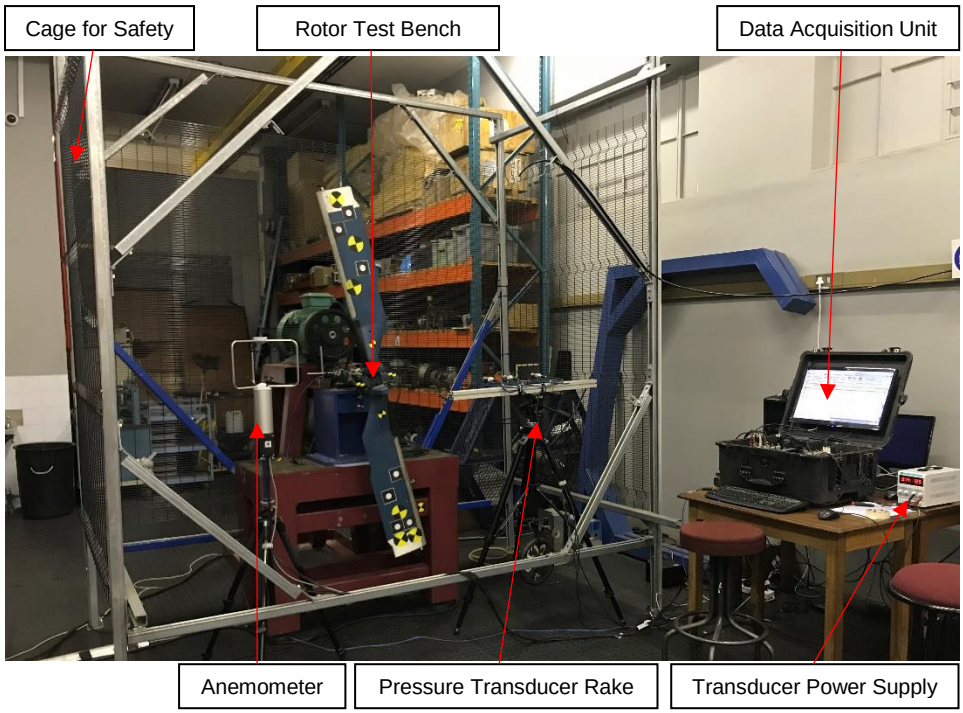

Figure 2-7: Complete experimental setup

A cage that was constructed around the rotor test bench can be seen in a few of the figures. This was for safety purposes. An anemometer is also seen in the experimental setup which was connected to the data acquisition unit and for which data was recorded during the experiments. The particular anemometer used can determine wind velocity 3-dimensionally where it was hoped that the results could be used for validation. The results produced by the anemometer were however discarded as it collected data at a maximum output frequency of 32 Hz which was insufficient in capturing any useful transients when the helicopter rotor was ramped up to full speed.

2.3 Experimental Data Preparation and Results

Two sets of experiments were conducted in order to acquire results at the two rake locations thus producing six pressure readings in the field of the rotor blade. The pressure results produced in test one when the rake was placed 20mm from the blade chord line are referred to as probes 0, 1 and 2 for radial locations 620mm, 744mm and 930mm (at the tip), respectively. Similarly, the rake of transducers positioned 100mm from the blade chord line for test two are referred to as probes 3, 4 and 5. Figure 2-8 illustrates a portion of the tachometer pulse recorded during test one which also portrays the competence in the selected sampling frequency on the data acquisitioning unit in representing the zebra strip profiles. The zebra strip used in the experiments had 23 pulses per revolution. When placing the zebra strip around the shaft, the butt joint formed when the two ends met interlaced the strip pattern well

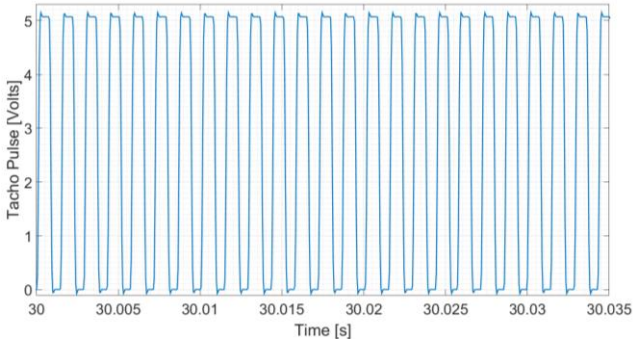

Figure 2-8: Tachometer pulse with 23 pulses per revolution

which is evidenced in Figure 2-8 since there aren't any substantial deviations amongst the pulses. The tachometer signal was then transformed into a plot of the revolutions per minute shown in Figure 2-9 for each test.

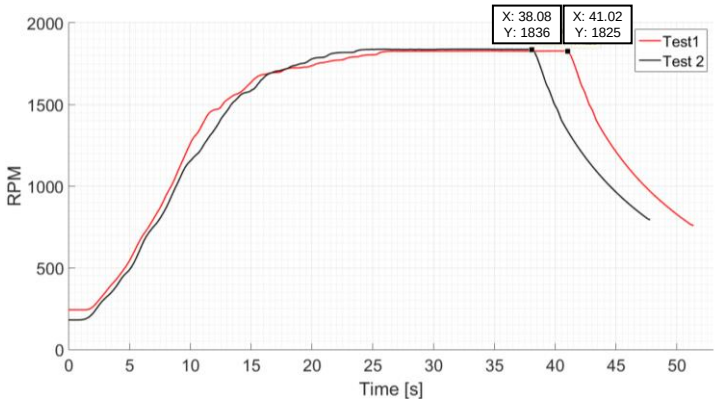

Figure 2-9: RPM of helicopter rotor blade for experimental testing

The maximum rotational speed achieved by the rotor test bench was with a zero-pitched rotor due to the power restrictions of the electrical motor. Increasing the pitch of the blade increases the drag experienced by each blade and thus the torque required. Using an electrical motor at its maximum power results in the rotational speed being reduced with the increased torque. The experiments were performed with a zero-pitch blade so that the maximum rotational speed could be used for this investigation. Figure 2-9 shows that the test bench achieved a maximum average of 1830 RPM between the two tests. A zero-pitched rotor does not emulate the operational conditions of a helicopter rotor and the rotational speed acquired in the experimental investigation is lower than that specified for the particular rotor in Table 2-1. However, these conditions are good for the purposes of this study as one can still draw useful conclusions from the described investigation. Also, consider that Singh *et al.* (2008) simulate a tail rotor speed of 1564 RPM in their research while Strawn and Biswas (1996) use a zero-pitched rotor in their study of helicopter rotor aerodynamics and acoustics.

Figure 2-9 shows how the speed was ramped up once recording began. When maximum power was reached, the data was recorded for a few seconds at constant speed and then powered off. The raw data was converted from Voltage [V] to Pressure [Pa] and the mean of each data set was subtracted to remove any DC offset in the data due to elevation effects thus representing a 0 gauge pressure. Each data set was then filtered to discard the data outside of the constant speed ranges where test one used the data set from 27s to 41s and test two used the data set from 25s to 37s. Figures 2-10 and 2-11 show the pressures that were recorded by each probe for the constant speed patches.

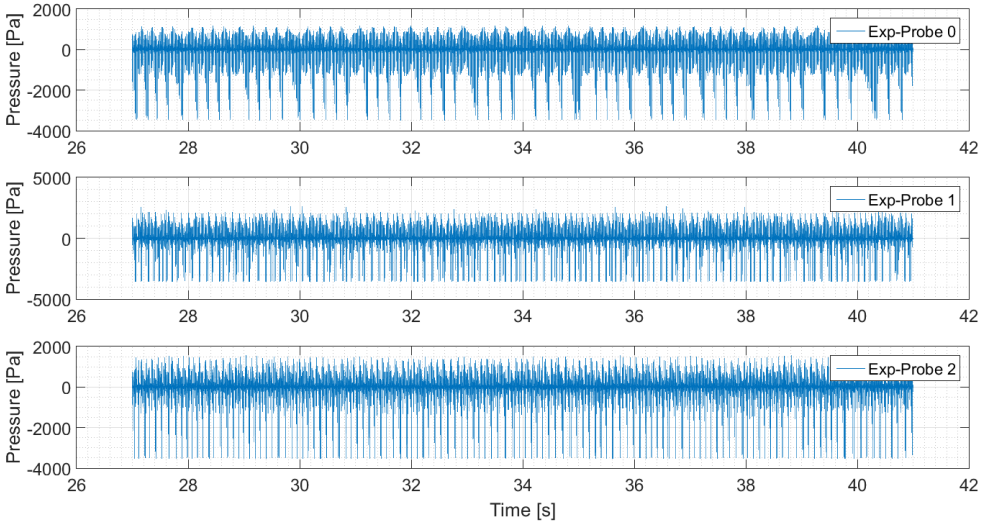

Figure 2-10: Experimental test 1 pressure data during constant speed

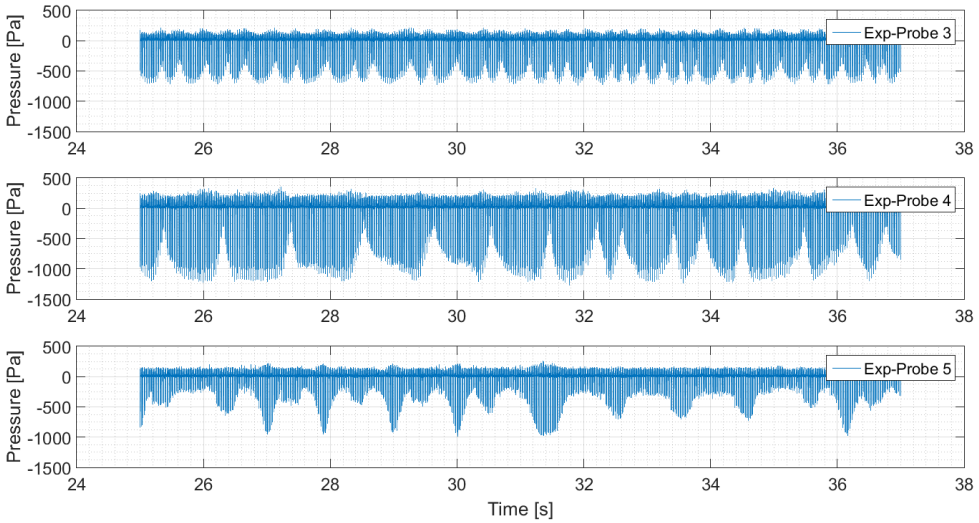

Figure 2-11: Experimental test 2 pressure data during constant speed

Apart from visually showing the general trend in the pressure fluctuations and identifying the presence of a low frequency component, presentation of Figures 2-10 and 2-11 do not provide much useful information. The tachometer signal was used to perform a time-synchronous average of each data set so that comparisons can be done on a single period of the rotor pressure profile at the recorded locations. Figures 2-12 and 2-13 show an overlay of all the segregated signals used to generate the averaged signal (plotted as a thicker black line) for probes 0 and 3 respectively. The maximum and minimum recorded values are plotted as dashed red lines. Two pulses occur per revolution of the blade as a result of the two blades passing the pressure rake. Despite the high sampling frequency of 19.2 kHz, the pressure signals display a quantised like appearance. This is however not a result of the sampling frequency on the data acquisitioning unit being too low but rather due to the limitation in the sampling frequency of 1 kHz of the WIKA P-30 sensor itself. This limitation results in the data acquisition unit rerecording the value held by the pressure sensor in-between each of the samples it produces. An attempt was made at resampling the pressure signals to the probe limit of 1 kHz as a post-processing step but this was found to degrade the profiles produced after averaging significantly. Even though the quantised signal is not a good physical representation, the averaged results provide a fair representation of the pressure profile for a revolution of the blade. One should also note the slight phase mismatches in Figure 2-12 for some of the signals which may be a result of minor fluctuations in the rotor rotational speed. The results presented in Figure 2-13 are seen to be a lot more orderly and represent the pressure profile well. When comparisons are completed with these time-synchronously averaged signals, the maximum and minimums are also plotted to gauge the variations.

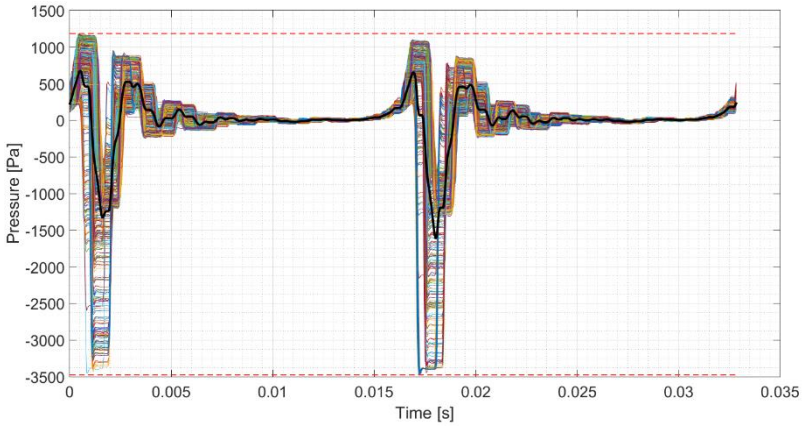

Figure 2-12: Time-synchronous averaging of experimental probe 0

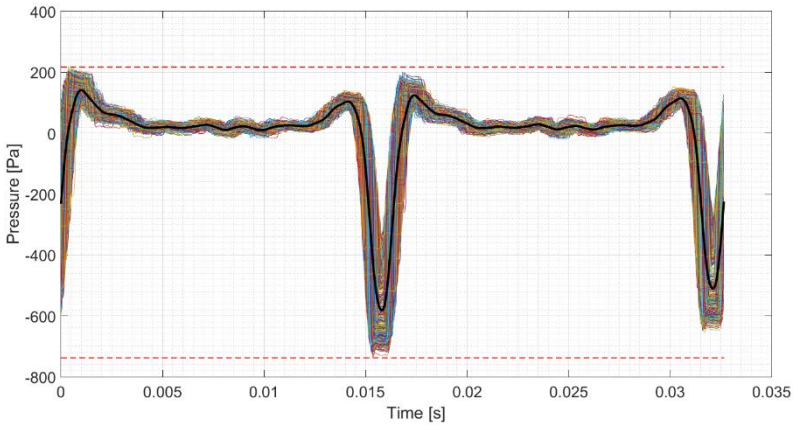

Figure 2-13: Time-synchronous averaging of experimental probe 3

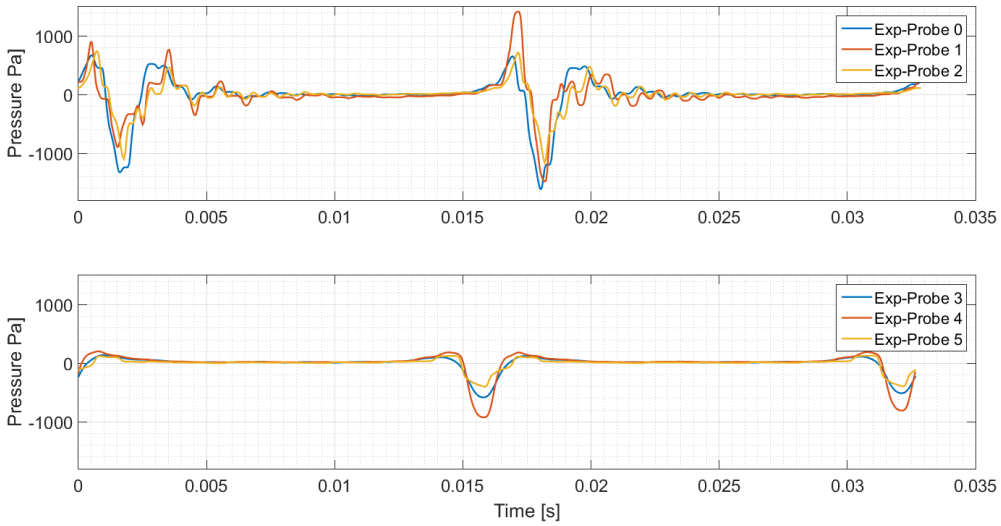

Figure 2-14: Comparison of experimental pressure results

Figure 2-14 provides a comparison for each of the pressure signals after they were processed. As one may expect, probes 0, 1 and 2 produce higher peak values as they are situated closer to the passing blades. These transducers also exhibit fluctuations in the pressure after the blade passes which indicates the presence of trailing vortices and other transients disturbing the flow near the blade and in its wake. These occurrences do not possess enough energy to affect the transducers situated further away. A progression in the peak values of the pressures is seen for the transducers placed at 67% and 80% of the blade radius while the transducer at the tip displays smaller values. The rising pressure as one moves from the centre to the tip is related to the increase in linear velocity along the blade from the hub to the tip with losses at the tip due to tip vortices. Finally, one should note the differences in the peak values for the two different blades expressed by all six pressure signals. A static analysis of the rotor test bench, in which each of the blade tracks were measured with respect to a fixed location, found that the tips were 15 mm out of track (i.e. a single blade was approximately 0.95° out of plane with respect to the hub). Even though the level of mistracking was not substantial, it evidences that the experimental investigation was not conducted with a blade which tracked perfectly. Importantly, this is shown in the different peak levels of the results which the investigation sets out to prove. It is also noteworthy that this degree of mistracking features in these results considering they were time-synchronously averaged. This is essential when one considers the variance displayed in the peak values of the signals of Figure 2-12 which may be due to any of a number of factors as discussed in the following paragraphs.

Having compared the pressure signal levels in the time domain, an analysis was also conducted in the frequency domain to compare the frequency components present in the pressure signals. The full pressure signals over the constant rotational speed sections were

transformed into the frequency domain using a Fast Fourier Transform. To ensure that the quantised structure of the oversampled signals did not affect the frequency results, the signals resampled at 1 kHz were tested. No difference was found between the results produced and thus the complete signal was used to maintain consistency in the analysis. Figure 2-15 compares the results produced for each pressure signal in the frequency domain. All of the signals evidenced amplitudes at the blade pass frequency of each test (≈ 61 Hz) and its respective harmonics. A frequency component and its harmonics is also observed at the rotational frequency of the rotor (≈ 30.5 Hz) indicating the described mismatch in the blades during the experiments.

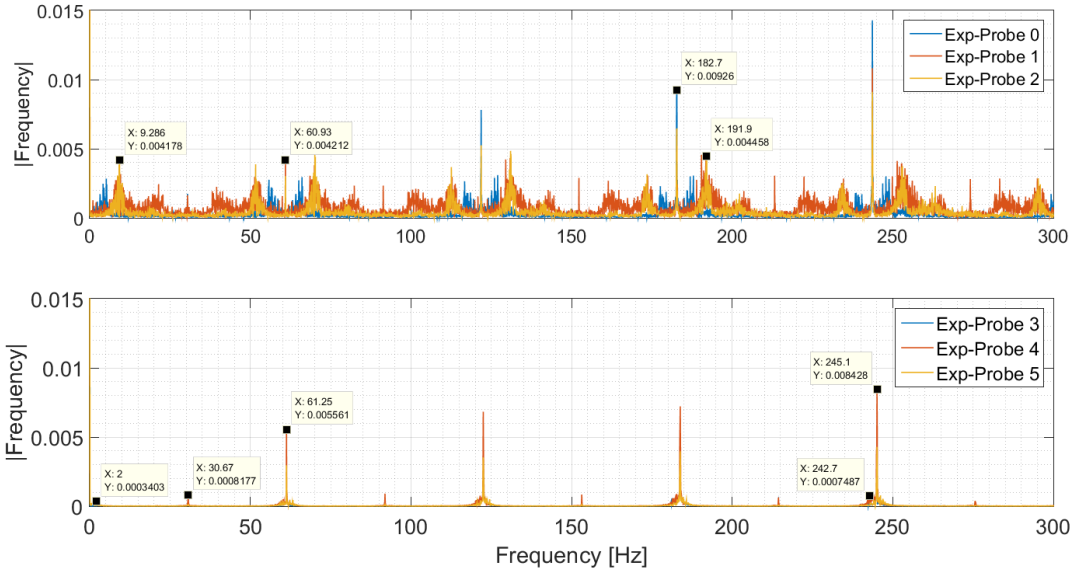

Figure 2-15: Comparison of experimental frequency results

Transducers 0, 1 and 2 in Figure 2-15 clearly show sidebands around both the blade pass frequencies and the rotational frequency. Sidebands are typically indicative of modulation. The modulation that occurs in these experiments may be a result of the rigid body flapping of the blades or due to flow phenomena in the wake of the blades such as vortex shedding. Section 1.2.3 described the behaviour which typifies an articulated helicopter rotor blade. It is understood that a helicopter rotor blade responds to flow dissymmetry through blade flapping (amongst others). This implies that blade flapping may only occur as a consequence of a specific flight manoeuvre while condition monitoring would be exercised under steady and controlled conditions. Even though this is true, the possible effect of blade flapping on the results cannot be ruled out since the tail rotor has a flexible coupling at the hub which may allow the blade to experience motions about this hinge degree of freedom or vibrate during the experiments. Even though blade flapping cannot be confidently ruled out, there may be more evidence that the modulation results from flow phenomena rather than the blade flap. The modulating frequencies are present in the spectrum (≈ 2 Hz, 5 Hz and 9 Hz) where one could also compute them as the difference from the carrier frequency. The modulating frequency suggested by probe 0 is different to that suggested by probes 1 and 2 where one might expect the same frequency at all probes for a flapping blade since it would be a rigid body movement. Radial locations along the blade represent different linear velocities in which vortex shedding may be occurring at different rates. Transducers 1 and 2 produce similar results since they are near each other and are most likely dominated by the tip vortex. In the fan experiments conducted by Xu, Amano and Perez (2002), they describe the presence of higher frequencies to be related to the fan rotation as has been discussed in this instance and lower frequency components to be a result of aerodynamic delay. Therefore, what they broadly define as aerodynamic delay could be a result of the behaviour of the flow in the wake of the blade and ultimately be responsible for the presence of the low frequency pressure fluctuations.

It is likely that the modulation is due to one of these components, as opposed to other factors such as pressure rebounds from the laboratory walls or the presence of the safety cage, because of the dependence of the modulation on the positioning of the rake. Transducers 0, 1 and 2 clearly show sidebands unlike transducers 3, 4 and 5 implying that one might expect to see the effects from the laboratory or safety cage in results at both rake locations but are not seen to as high of a degree in the transducers placed further away.

2.4 Conclusion

This chapter discussed the experimental setup as well as the experimental procedure that was followed in order to capture data that shall be used to validate the numerical simulations. Experimental results provide quantitative validation since the actual values can be compared, as well as qualitative validation as the results can be used to portray what the model lacks physically and how it relates to reality in representing the actual phenomena present.

Two important features of the setup were determined during the experimental testing which include the use of a zero-pitched rotor and a rotational speed of 1830 RPM. The results presented set the basis on which comparisons shall be made which include a time domain comparison of the pressure peaks produced by each blade in the signal at that location and a frequency analysis to assess the frequency content in the pressure signals.

Chapter 3 – Numerical Validation and Investigative Studies

The research scope detailed in Chapter 1 states a number of broad assumptions and simplifications in order to direct the investigation. There are however many detailed modelling assumptions that require further consideration. This is done here. The modelling options are considered based on cross sections of the rotor. Performing the studies in this way allows the complexity of the final model to be reduced into smaller components. The results of each of these smaller components culminate in the construction of the final rotor simulations with motivation behind their choices.

A description of what is entailed in the investigations and how they are carried out is described as well as the relation that the studies have to physical occurrences on the blade. The effect of adjusting the chord length with respect to results from literature is considered. A mesh independence study is performed to acquire a good balance between computational expense and adequate flow field resolution before considering the effect of the wall function initial conditions. Comparisons are made between different solvers and turbulence models at different speeds and compared to literature to make justifiable decisions on their selection. Finally a few other considerations in preparation of the full rotor simulation are discussed.

3.1 Investigation Description

A three-dimensional transient simulation of the full rotor incorporating all of its associated complexities is difficult to resolve immediately. For one, it is not known to what degree the fluid dynamics need to be represented for the particular rotor and it can be computationally expensive to perform unnecessary iterations on the full model in the event that inappropriate models are used. Breaking down the problem into simplified simulations will allow for a better understanding of the aspects involved in tackling the full scale model.

Simulations are therefore first conducted for the 2D cross-section of the NACA 0012 airfoil of the rotor. This provides a necessary basis from which the research topic can develop and be built on, increasing the complexity until the full scale model is implemented.

It has been identified that the linear velocities at cross sections of the blade may vary from zero at the centre to the maximum at the tip according to equation 1.16. Understanding when transition and turbulence may appear and when flow becomes subsonic or transonic is important so that the correct modelling can be implemented for the 2D airfoils and rotor. Equation 1.1 and 1.16 can be rearranged and substituted to produce Equation 3.1 below.

$$r = \frac{Re\,\mu}{\omega\rho L} = \frac{Re\,\mu}{\frac{\pi N}{30}\rho L} \tag{3.1}$$

Considering that flow transition starts to occur at Re = 5x10^5, with the reported rotor rotational speed from the experimental work in Chapter 2 and the chord length of the tail rotor blade from Table 2-1, then r = 0.206m. This is based on fluid properties for air at 1 ATM and at room temperature of 20˚C which yield $\rho = 1.225\ kg/m^3$ and $\mu = 1.7894 \times 10^{-5}\ Ns/m^2$.

Also, equations 1.16, 1.6 and 1.7 can be rearranged as follows:

$$r = \frac{Ma \times a}{\omega} = \frac{Ma \times \sqrt{kRT}}{\frac{\pi N}{30}} \tag{3.2}$$

Using a Mach number of 0.3 and fluid properties for air at room temperature produces a radius of 0.537m.

These two calculated radii indicate the distances at which turbulence and subsonic flow can be expected along the rotor. Figure 3-1 indicates these points on the rotor blade where it can be seen that turbulence occurs along most of the blade with subsonic flow experienced at the outer half of the blade. Substitution of Mach = 0.8 into equation 3.2 yields a radius of 1.43m which is beyond the radius of the tail rotor implying that the rotor blade is not expected to feature transonic flow. The calculations above indicate that turbulent conditions can be assumed over most of the blade with further investigation into the compressibility experienced by the fluid.

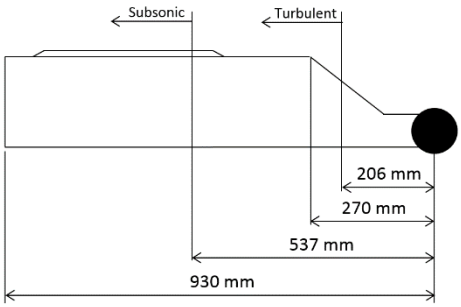

Figure 3-1: Expected flow along helicopter tail rotor blade

Several studies in literature analyse two-dimensional flow around the NACA 0012 airfoil, both numerically and experimentally. Mach 0.3 and 0.5 air speeds are popular for these investigations. Considering that Mach 0.5 relates to a rotor radius of 0.895m, which is near the tip of the blade, validating numerical results using these two speeds will provide fair representation for most of the blade. This will allow the selection of parameters which one could anticipate to model the entire rotor effectively.

Rumsey (2016) provides a validation case for the NACA 0012 airfoil at different angles of attack and a chord length of 1m based on experimental and numerical results using different turbulence models. As a starting point to this investigation, the numerical procedure detailed by Rumsey is followed with some minor differences to replicate the results. Replicating the validation case provides a firm base on which to make comparisons as modelling occurs under the same conditions as well as providing confidence in the implementation of the CFD software. Deviations between the produced results and the validation results can be appropriately described without misconceptions based on modelling different scenarios. With this notion in mind, the first imperative comparison is assessing the deviation in the results when adjusting the chord length of the airfoil from 1m to the corrected 0.185m for the zero-pitched rotor blade.

The investigative studies then assess the mesh density requirements for the corrected airfoil through a mesh independence study. The results of the study provide a meshed domain around the airfoil which adequately resolves the flow field whilst having an efficient mesh count. The selected mesh is used for the remaining studies in this chapter and provides a reference on which the meshes for the full rotor are based. Use of the study to define the full rotor case is required as a mesh independence study at such a scale would be uneconomical.

The remaining studies consider different wall functions for boundary layer treatment, the selection of a specific RANS turbulence model and the selection of an appropriate solver in modelling the fluids compressibility. These parameters are determined based on their applicability in modelling the full rotor and their correlation with the validation data at the specified speeds. Acquiring the parameters through these studies gives confidence in setting up the full rotor simulations and even though accuracy in modelling performance parameters is not the main objective; validation with results from literature ensures that the results reflect realistic conditions.

All of the investigative studies make use of the same geometry and case setup; the parameter of interest is the only change in each study to assess its effects independently. Figure 3-2 portrays the domain used with the airfoil situated at its centre. The domain boundaries for the generated geometry were placed at a radius of 140C (where C represents the chord length) while the outlet boundary was sliced at 110C from the leading edge. The slice facilitates the mesh generation as a C-shaped procedure is followed producing better mesh orthogonality around the airfoil and thus improving quality. The boundary locations used in these studies are smaller than those used in Rumsey's validation case for computational efficiency as there are a number of studies performed. The effects of placing the boundaries at these reduced locations were considered and found negligible with enough mesh resolution. Figure 3-2 also describes the boundary conditions that were imposed for velocity and pressure.

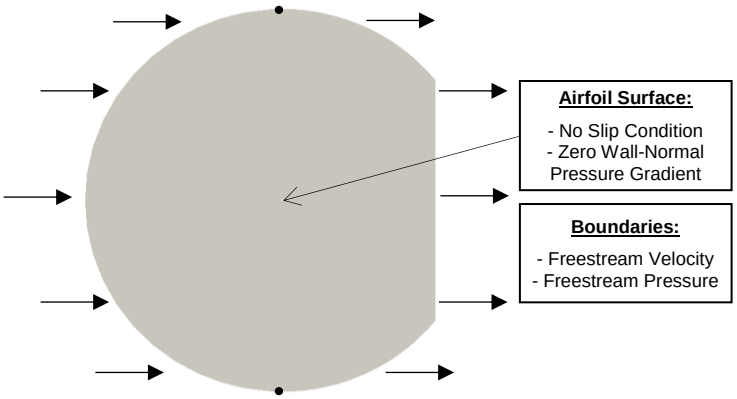

Figure 3-2: Domain of investigative studies

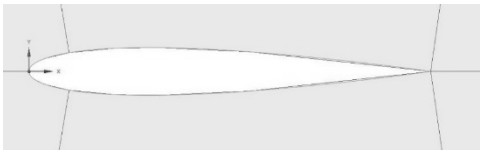

Figure 3-3: Airfoil profile

It is important that the geometric profile of the airfoil is sufficiently specified. Inaccurate representation of its geometry will generate poor results. The airfoil profile can be generated by plotting points defining the profile as described by Airfoil Tools (2017) or Abbott and Von Doenhoff (1959) and fitting a line through the points. Equation 3.3 is Rumsey's adjustment of the original NACA 0012 equation which defines the profile for values of x between 0 and 1. The adjustment suits a CFD analysis well as it forms a sharply closed trailing edge, as opposed to a realistic blunt edge. One thousand evenly spaced x points were used to generate the airfoil profile to ensure that the geometry was well resolved. These values were linearly scaled to produce the airfoil with the shorter chord length of 0.185m. Figure 3-3 shows the airfoil geometry.

$$y = \pm\, 0.594689181\left(0.298222773\sqrt{x} - 0.127125232x - 0.357907906x^2 + 0.291984971x^3 - 0.105174606x^4\right) \quad (3.3)$$

Solver selection is later performed at both validation speeds to assess the fluid compressibility effects. However, studies in Sections 3.2 to 3.5 consider a single velocity derived from a Reynolds number of $6\text{x}10^6$ as specified in the validation case. The simpleFoam solver in OpenFOAM is used which models steady-state, incompressible flows with turbulence. The one-equation Spalart Allmaras (SA) and two-equation k-Omega SST (SST) turbulence models are considered due to their reputation in modelling the expected flows. Second-order discretisation schemes were used and simulations were monitored and run until convergence was achieved. Deviations from the above case setup will be specifically mentioned in each case. Overall, good CFD practices were used throughout.

Modelling rotor performance is not the objective but using the lift, drag, pressure and skin-friction coefficients for comparisons throughout the investigative studies is convenient. These quantities allow the parameters of concern to be compared against one another and represent how well they model values from experimental and numerical sources. The figures in the following sections make reference to Rumsey, Ladson&Gregory (2016), CFL3D (Rumsey 2016), Agard1 Ma0.3, Agard1 Ma0.5, Agard2 Ma0.5 and Immersed BL 0.5. The data

expressed as Rumsey, Ladson&Gregory (2016) and CFL3D (Rumsey 2016) all come from the validation case with different naming used based on where Rumsey acquired the information. The reported CFL3D simulation used a k-Omega SST turbulence model. The Agard citations represent results from Agard (1979) with specification on results taken from two different experiments presented in the paper (1 or 2) and for Mach 0.3 or 0.5. Finally, Immersed BL 0.5 represents the numerical results of Karimian and Ardakani (2011) for the airfoil at Mach 0.5.

3.2 Chord Length Effect

The chord length of 1m specified by the validation case and the corrected chord length of 0.185m for the actual rotor were simulated under the exact same conditions. Even with the same conditions, one should not expect the results to resemble each other exactly. The induced velocity is maintained at the same speed in each case implying that the airfoil's encounter the same freestream Mach number but different Reynolds numbers. Figure 3-4 shows the lift and drag coefficients for the airfoil's simulated with the Spalart Allmaras and k-Omega SST models against the validation data. Figures 3-5 and 3-6 show the pressure and skin friction coefficients along the surface of the airfoil for these cases respectively. Note that even though the corrected chord length was simulated, the data is normalised by dividing by the chord length for comparison purposes.

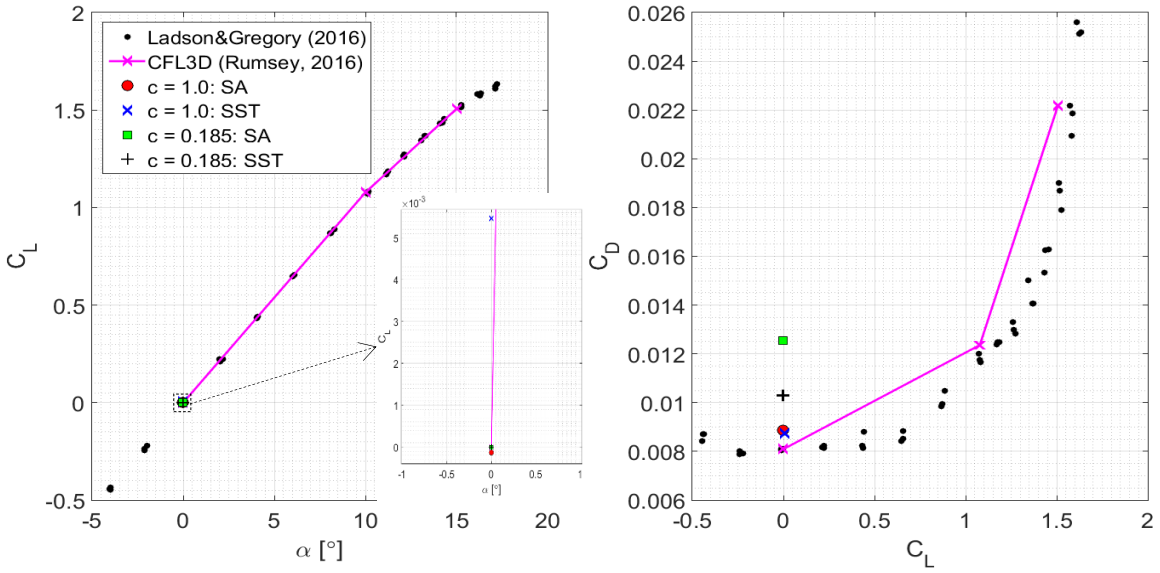

Figure 3-4: Lift and drag coefficients for different chord lengths

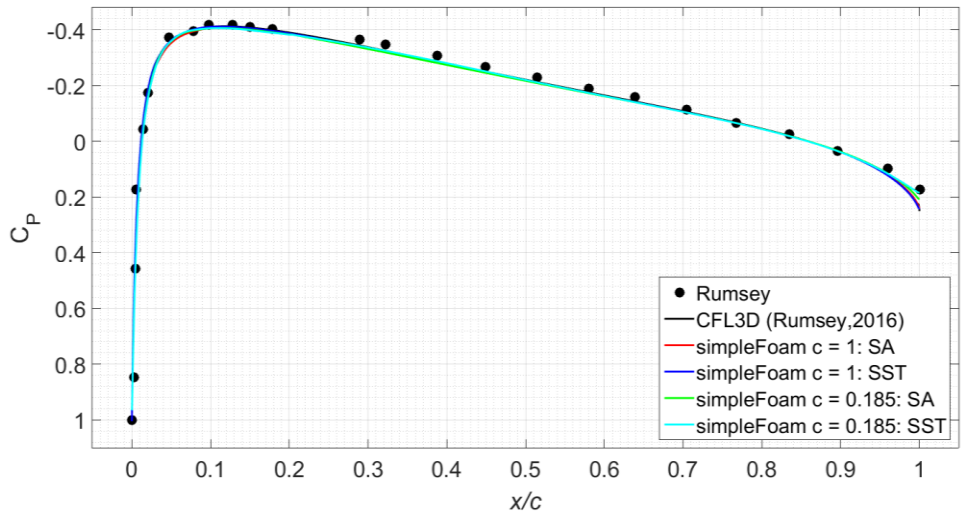

Figure 3-5: Pressure coefficients for different chord lengths

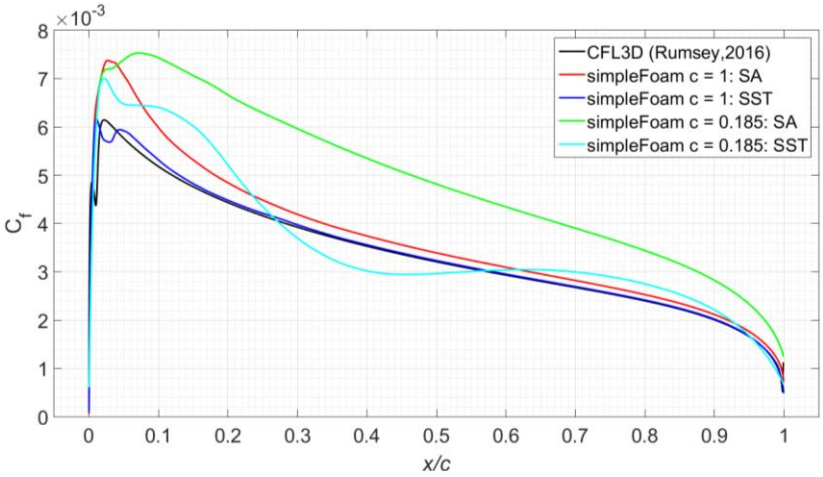

Figure 3-6: Skin friction coefficients for different chord lengths

If one first considers the cases simulated to replicate the validation case (i.e. c = 1), agreement is found for the lift coefficients as well as the pressure coefficients. The zoomed in portion of the lift coefficients shows some spread in the predicted values but these are found on a small scale and can be considered negligible. Each case approximates zero lift for the symmetric non-pitched airfoil within reason. Both turbulence models predict similar drag for the validation case and are slightly higher than those displayed by the validation data. The skin friction data from the validation case was approximated with an SST model, good correlation is found when compared with the simulation in this investigation over most of the airfoil with a slight difference at the leading edge. The two SST models for c = 1 predict a double hump in the skin friction at the leading edge but at different locations and to different extents. This might be a result of different mesh resolutions at the leading edge. Also the minor differences between their profiles and thus modelling is the probable reason for the drag differences. Attention is also drawn to the difference in the profile of the SA model compared to the SST models for the skin friction. It is expected for the models to perform differently but it is interesting that they predict similar drags. This implies that the drag from the SA model experiences a smaller contribution from the pressure (form) drag than the SST model which is an expected coincidence since SST models separation better. This is confirmed in Table 3-1. Even though there are slight differences between the simulated and validation results, the simulations replicate the results and predict the trends to an adequate degree. Confidence in further studies can be drawn from these results.

Comparing the results for the change to the corrected chord length, the lift and pressure coefficients relate well. Both turbulence models predict elevated drag coefficients (understanding they are normalised to the smaller airfoil's surface area) in comparison to the validation chord length and also display a spread between one another, unlike the previous case. Consider that rearranging the Reynolds equation to determine the characteristic length at which transition occurs produces a value of 0.083m. In theory, this transition length is the same for both airfoil's but the airfoil's have different lengths, therefore transition occurs near the leading edge of the validation airfoil, meaning that almost all of it is in turbulence (modelled with a high turbulence intensity over almost all of the airfoil) while turbulence only occurs near half way along the corrected airfoil (a low turbulence intensity is modelled along the former part of the airfoil while the remainder of the airfoil possesses a high turbulence intensity).

Table 3-1 demonstrates the contributions that the pressure drag (as a result of flow separation) and viscous drag (as a result of shear stress indicated by the skin friction coefficient) have on the total drag of the airfoil for each simulated case. Due to the fact that the validation airfoil possesses increased amounts of turbulence, flow separation is prolonged restricting the contribution that pressure drag has. On the other hand, the corrected airfoil experiences more separation relative to its length and thus increased pressure drag is experienced as shown in Table 3-1. It becomes more evident if one considers the advanced capabilities that the SST model has in modelling flow separation and recirculation in comparison to the SA model and

comparing their results in Table 3-1. The SST model is seen to capture a larger pressure drag contribution for each airfoil but specifically for the corrected airfoil.

Table 3-1: Drag force breakdown for different chord lengths

Simulation		**Drag Force [N]**		
Chord	*Model*	*Total*	*Pressure - Separation*	*Viscous - C_f*
1	SA	55.77079	9.540321 (17.11%)	46.23047 (82.89%)
1	SST	55.14081	12.33108 (22.36%)	42.80973 (77.64%)
0.185	SA	14.61806	3.332204 (22.80%)	11.28585 (77.20%)
0.185	SST	11.97887	3.707058 (30.95%)	8.271808 (69.05%)

Observing the skin friction coefficient for the SST model on the corrected airfoil also suggests that separation occurs at around x/c = 0.3 based on the dip in the profile which is not observed for the SA model. This is probable since it was theoretically predicted that transition occurs sometime after this point; the turbulence intensity deficit restricts the flow from overcoming the adverse pressure gradient as the flow passes the highest point of the airfoil (remembering that 30% marks the maximum airfoil height) suggesting separation and recirculation in this region. The incapability of the SA model to predict this separation means that it overdetermines the viscous forces signified by the area under its skin friction profile for the airfoils. Flow separation might also be signified by the small deviations in the pressure coefficient at the trailing edge.

In summary, the corrected airfoil experiences a higher relative drag because there is increased flow separation as a result of the delay in transition to turbulence. This is modelled well by the SST model and simply modelled as increased viscous forces by the SA model due to its inferior capability in modelling the small amount of separation present.

Overall the results presented are good. This investigation demonstrates that the validation case was replicated fairly with the minor deviations discussed. The effect of changing the chord length on the turbulence properties and flow fields were identified and descriptions given on the observed quantities. Further investigative studies make use of the corrected chord length and can be compared with confidence.

3.3 Mesh Independence

Maximum, minimum and average values for metrics such as the aspect ratio, skewness and orthogonality can be used to assess the quality of a mesh when generating it. However, even if a mesh has been generated with good qualities it may not have the resolution required to capture certain physics and flow phenomena. Simply increasing the size of a mesh is also not a feasible approach as the run-time and computational power required increases with an increasing mesh size. Thus a mesh independence study is performed where the mesh is refined until certain monitored variables are seen to converge.

The mesh independency study was completed by maintaining the same geometry and case settings but using different mesh counts. Simulations were performed using the k-Omega SST model in all cases. Local mesh controls were defined on the geometry described in Section 3.1 to control the mesh generation. Biasing (or stretching) of the mesh in certain zones was also used to stretch the mesh such that the mesh could be focused in regions of interest such as near the stagnation point at the leading edge of the airfoil, near the airfoil surface and in the wake where large gradients are expected in the flow field. The element size and bias factors used for each size control were parameterised so that the effects of the mesh could be explored in a parametric study. Emphasis is focused on creating a mesh which possesses a block-like structure as this is generally desired for good quality cells, renders better results and aids in the convergence of the solution. The study began with a coarse mesh and proceeded into finer meshes where refinements were focussed around the airfoil and wake region by use of the bias factors. The coarsest mesh, referred to as DP0 (Design Point 0) is

shown in Figure 3-7 and can be contrasted to the finest mesh, DP4, shown in Figure 3-8. Each figure shows the mesh of the entire domain as well as a zoomed in portion of the area around the airfoil. Figure 3-8 displays additional views of the resolution around the leading and trailing edge of the airfoil. One may observe the sizing's through the domain as well as how elements were focused in localised areas.

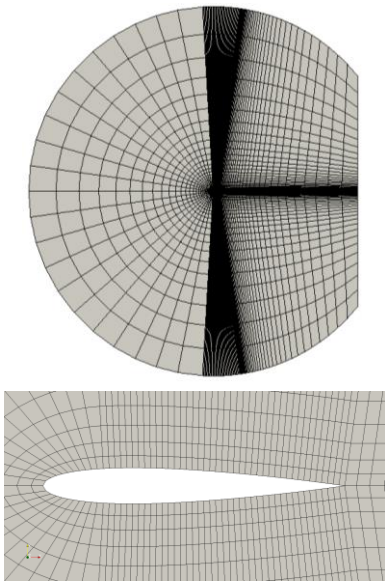

Figure 3-7: Coarse mesh of DP0

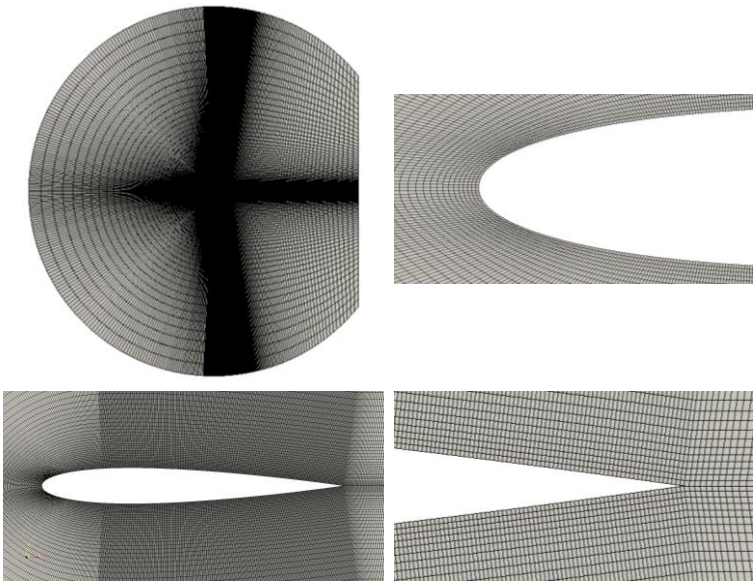

Figure 3-8: Finest mesh of DP4

The lift, drag, pressure and skin friction coefficients were again used to gauge the solution changes with the mesh changes. Figures 3-9 and 3-10 show the pressure and skin friction coefficients for the different design points, respectively. The poor quality of the results produced by DP0 can be observed while convergence towards a mesh independent solution is seen as the meshes are refined from DP0 to DP4. The pressure profile is almost converged by DP2 already, with slight differences observed at the trailing edge. The skin friction coefficient shows a bit more variability through the various meshes but convergence can be observed by the peaks at the leading edge.

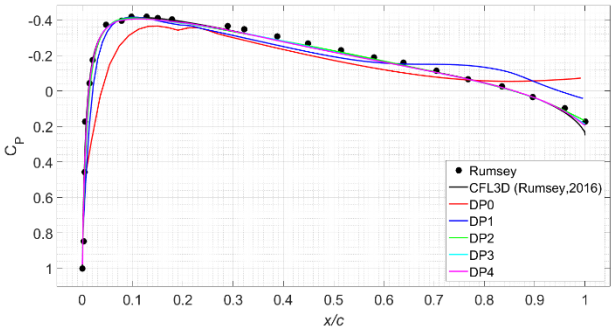

Figure 3-9: Pressure coefficient for mesh independence

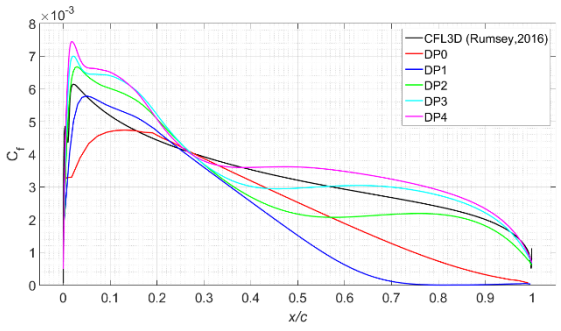

Figure 3-10: Skin friction coefficient for mesh independence

Figure 3-11 shows the converged lift and drag coefficients for each mesh explored, plotted against the total number of cells in the domain. The lift coefficient is seen to converge rapidly while the drag converges from DP0 to DP3. Changes in results can also occur by distributing the mesh differently through local changes. DP4 increased the mesh count slightly but more importantly the effect of distributing the mesh in the wake region was considered. This was found to have minimal effect on the results as observed, as long as the mesh was mostly focussed in the general region of expected flow phenomena as done through all design points.

The mesh generated in DP3 was selected as the converged mesh and to be used in the remaining investigative studies. The results of DP2 are not far from DP3 and use fewer cells but DP3 provides additional accuracy without being much more uneconomical, ensuring accuracy in further studies.

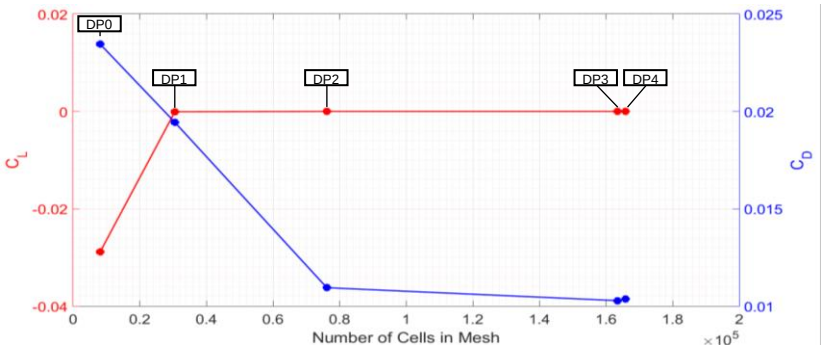

Figure 3-11: Lift and drag coefficients vs number of cells for mesh independence

3.4 Initial Conditions - Wall Functions

OpenFOAM requires that all fluid properties are prescribed initial conditions which the solver uses as a starting point in its first iteration. Initial values for the turbulent kinematic viscosity (υ_t or nut), turbulent kinetic energy (k), specific turbulence dissipation (ω or omega) and the turbulence field variable ($\tilde{\upsilon}$ or nuTilda) in the far field and at the walls were determined from equations specified by the validation case. The equations stipulated in the validation case are taken directly from the original derivations of the turbulence models. Values for the variables in the far field were prescribed freestream conditions while the wall of the airfoil was given a zero wall-normal gradient for pressure and the no slip condition for the velocity boundary conditions.

Values could be specified at wall regions for the turbulent viscosity which means that the boundary layer needs to be resolved. Alternatively wall functions could be used which reduces the mesh count significantly. Certain quantities have specific wall functions such as the kqRWallFunction for the turbulent kinetic energy but the turbulent viscosity has a number of functions available for selection. This study considers the effect of using different wall functions on the results for the SA and SST turbulence models.

Figure 3-12 shows the skin friction coefficient when using the two turbulence models and permutations of three different wall functions to model the turbulent kinematic viscosity near the wall. The nutkWallFunction performs poorly for both turbulence models. When used with the SA model, improbable results are obtained since the SA model does not specify or compute turbulent kinetic energy. A better response is seen for this wall function when used with the SST model, but its peculiar profile at the leading edge is incomparable to the other results including the validation case. The nutUWallFunction and nutUSpaldingWallFunction perform similarly and little can be described between them. The nutUSpaldingWallFunction was selected for use in further investigations due to the small difference in the two wall functions and it is defined as a scalable wall function which means that in the event that the y^+ drops below the recommended value of 30, it is capable of modelling in this region but not advised.

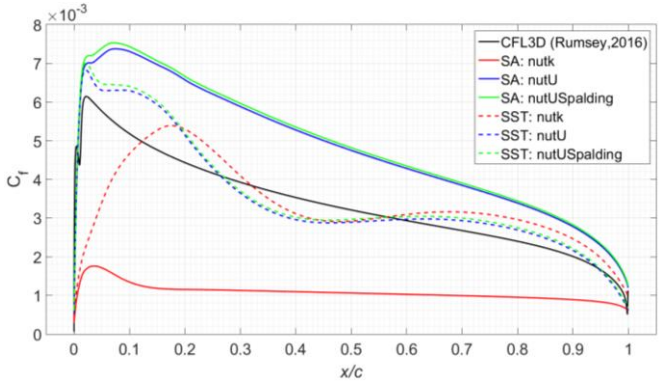

Figure 3-12: Skin friction coefficient for wall function study

3.5 Solver and Turbulence Model Selection

The previous sections have discussed the deviation found in the results for the rotor airfoil in comparison to the validation case, the convergence of a mesh independent solution and the selection of an appropriate wall function. All of these studies used simpleFoam, the steady-state incompressible solver, but ultimately the goal is to perform a transient analysis to acquire time-dependent data. The presence of compressible effects on the fluid at the outer half of the rotor has also been alluded to. This section considers solvers which model compressible behaviour and introduces a transient analysis. The simulations are performed at the two rotor representative speeds and compared to data from literature so that an appropriate selection can be made. From these studies, a solver is selected for use in the final rotor simulation and a discussion is given on the turbulence model performances leading to the selection of one.

In the studies to follow results from an ANSYS-Fluent simulation are included for comparative purposes only. This software package is not to be used in the final rotor simulation but was available for the investigative study where an incompressible k-Omega SST solution was attained for the rotor at Mach 0.3. The familiar simpleFoam solver is used for steady-state, incompressible and turbulent flow whereas rhoSimpleFoam is a steady-state, compressible solver for turbulent flow. Finally, pimpleFoam is a transient solver for incompressible, turbulent flow which uses a merged PISO-SIMPLE algorithm hence the term ‘pimple’.

When conducting the investigative studies using the transient solver, an issue in the case setup caused instability and convergence to unsteady results that could not be made sense of. It is possible that the problem may have been in the initial conditions specified for the case but this could not be resolved satisfactorily. To overcome this, the transient solvers were initialised with the steady solutions of simpleFoam and allowed to converge to solutions which made more sense. Results for the attempted transient solutions from specified initial conditions are provided for the Mach 0.3 case with the final results in all cases of the transient simulations having been initialised using simpleFoam (sF ini). To obtain the results presented in this section for the transient analyses, the fields were sampled at a high rate and then averaged.

Figure 3-13 shows the drag coefficients for the various solvers and turbulence models simulated at freestream speeds of Mach 0.3 and 0.5. The offset between the simulated drag

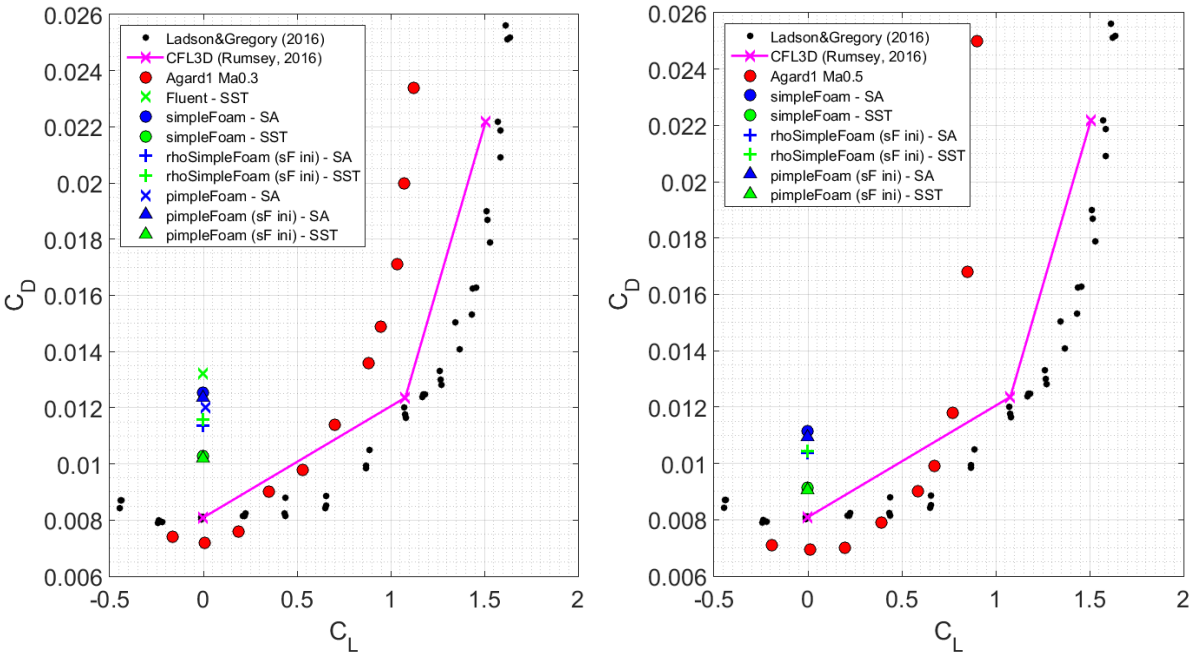

Figure 3-13: Drag coefficients for different solvers and turbulence models at Mach 0.3 (left) and at Mach 0.5 (right)

coefficients and the results from literature may be explained by the chord length effect as described in Section 3.2, with possible minor losses in accuracy due to the use of wall functions and not resolving the boundary layer. However, for the results produced, similar behaviour is observed for all the models at both speeds. The Agard results from literature report a small reduction in the drag coefficients at Mach 0.5 for the lower angles of attack, this trend is well represented by the models as a clear reduction in the drag coefficient is observed. As expected, the SST models perform better approaching the validation data with groupings seen for the same turbulence models between the steady and transient solvers. The results for the steady compressible solvers are grouped between the two steady incompressible turbulence model groupings.

Figures 3-14 and 3-15 present the pressure coefficients over the surface of the airfoil for the different models at the two different validation speeds with an extra view on a zoomed in portion of the results at the leading edge. The erratic profile of the unstable pimpleFoam results are seen in Figure 3-14 supporting the decision to initialise the transient simulations with the steady results. In evaluating the models used to simulate Mach 0.3 it can be seen that all models, both incompressible and compressible, steady and transient as well as SA and SST represent the pressures well with minor deviations from the experimental results of Agard.

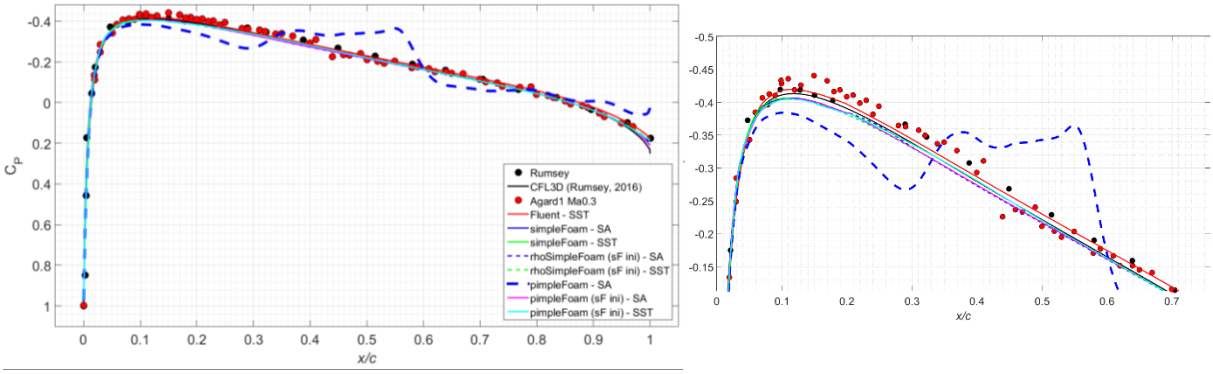

Figure 3-14: Pressure coefficients for different solvers and turbulence models at Mach 0.3

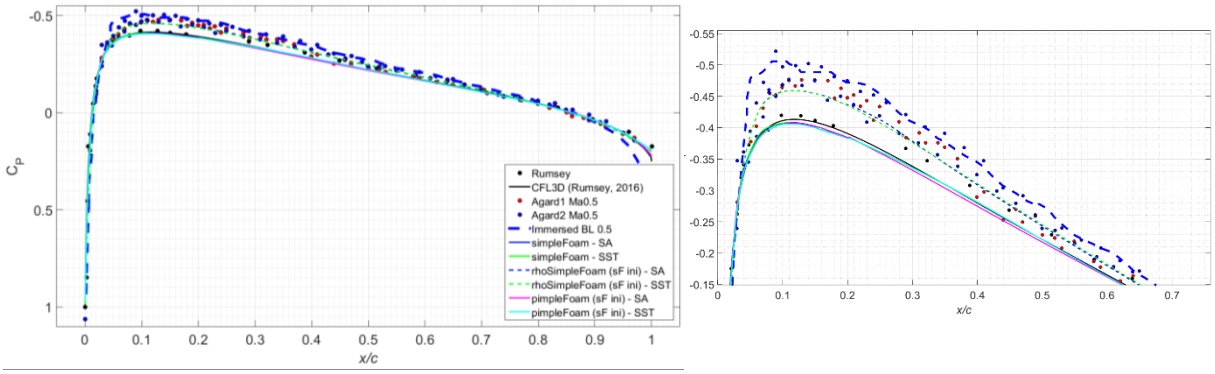

Figure 3-15: Pressure coefficients for different solvers and turbulence models at Mach 0.5

Considering Figure 3-15, it is apparent that there is a larger drop in the pressure at the leading edge for Mach 0.5 than for Mach 0.3. The incompressible models do not model this occurrence well where it is seen that both simpleFoam and pimpleFoam are restricted to the validation data provided for the lower, Mach 0.3, speed. The elevated drop in pressure can clearly be described by compressibility effects at Mach 0.5 since rhoSimpleFoam correlates well with the data provided for the higher speed. It is noteworthy that even though the compressibility of the fluid displays this marginal effect at the leading edge, all of the results and solvers converge at the latter half of the airfoil.

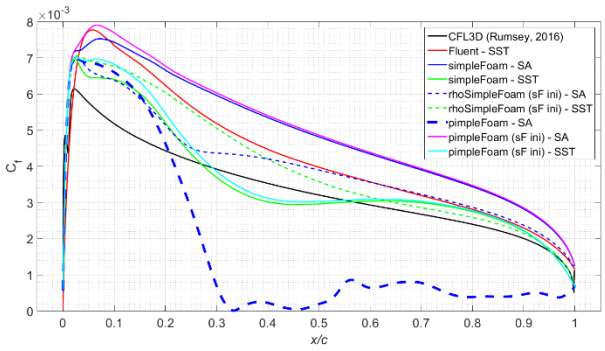

Figure 3-16: Skin friction coefficients for different solvers and turbulence models at Mach 0.3

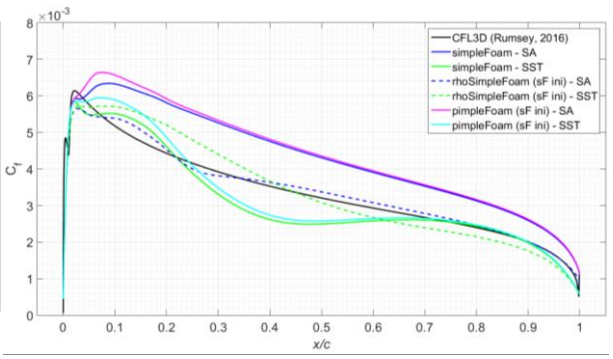

Figure 3-17: Skin friction coefficients for different solvers and turbulence models at Mach 0.5

Figures 3-16 and 3-17 exhibit the skin friction coefficients for the various simulations at the validation speeds. The peculiar results for the pimpleFoam results with specified initial conditions can once again be seen. It is interesting that the profiles of the skin frictions produced for each model resemble one another between the two speeds. The profiles at Mach 0.5 portray smaller peak values though, which may contribute to the reduced drag coefficients at this speed. It is probable that the overall drag decreases due to the increased levels of turbulence intensity, promoting mixing in the boundary layer delaying separation and reducing the pressure drag. The exact reason for the decrease in the skin friction as the speed increases is not known but it could be that with the increased pressure drop (and thus density drop) in this region, the normal forces that drive the fluid flow against the airfoil surface are reduced which diminishes friction and consequently the wall shear stress. Grouping of the incompressible solvers with the same turbulence models is seen with the compressible solver producing results somewhere in between them but with no real trend.

The above studies reveal that conversion from the steady state solvers to the transient solvers produces results that are very similar having noticed small deviations. Transient simulations provide additional information as the time dependent data can be averaged to reproduce steady results aside from other assessments and observations which can be conducted on the produced data. It was established that careful attention must be given to the initial conditions since the unsteady transient solver can easily stray from practical results even when using initial conditions that work for the steady solvers.

Compressibility effects on the flow field properties were observed between the two speeds by using the rhoSimpleFoam solver. In analysing the results of the various studies it is seen that the compressible solver presents values which are within reason of the incompressible solvers. The only substantial benefit of its use is in the accurate modelling of the pressure at the leading edge of the airfoil for higher speeds. A similar discussion can be given for the difference between the results of the SA and SST turbulence models. It is expected of the SST model to perform better since it models separation and recirculation better. This has been seen with better predictions of the drag and skin friction coefficient throughout. With that being said, the SA model performed well throughout having modelled lift and pressure well whilst exhibiting minor differences in the drag and skin friction values. Since the objective of this investigation is not focused on modelling performance parameters comprehensively, modelling can be done more efficiently using the cheaper SA model under incompressible conditions. Such a selection reduces the complexity and computational expense since modelling compressibility and using the SST model adds extra equations. Furthermore, using the SA model for the proposed rotor setup provides sufficient accuracy because extensive separation is not expected for the zero-pitched rotor. Small amounts of separation have been mentioned in the studies, but not enough to significantly affect the results.

3.6 Further Preparations

In preparation for the final rotor simulations a few other investigations were conducted to ensure that all grounds were covered developing the necessary skills to execute the modelling. In order to become acquainted with the dynamic mesh solvers in OpenFOAM, a simplistic model of a three-dimensional rectangular rotor was generated with a coarse mesh. The pimpleDyMFoam solver was used to perform the exercise as this is the intended solver for the final rotor simulation which is the transient incompressible solver for turbulent flows, like pimpleFoam, with the inclusion of dynamic mesh modelling. The results of this analysis are not presented as the study was done purely to gain exposure to the solver and the case setup required to execute the simulation.

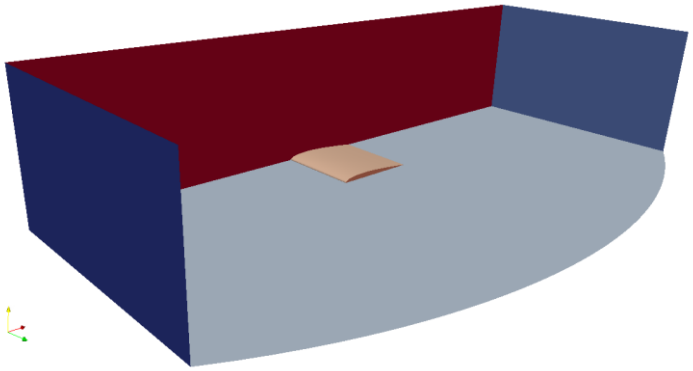

Figure 3-18: Domain of 3D rotor tip study

An attempt was made at modelling a portion of the tip of the blade to acquire further information about the mesh independency requirements as well as the effect of the boundary locations relative to the blade surfaces. The domain portrayed in Figure 3-18 was setup such that a symmetry plane was used through the centre of the symmetric airfoil to save computational costs. The portion of the rotor displayed represents the last 20% of the radial distance of the rotor. The study considered the effect of the normal and radial boundary distances as well as the mesh densities around the airfoil on parameters such as the skin friction and pressure coefficients over the entire surface as well as the forces experienced by the blade tip. Measuring from the plane of the rotor, normal boundaries at 10, 5, 2, 1 and 0.5 metres did not affect these parameters but normal boundaries smaller than this did. Measuring from the tip of the blade, radial boundaries at 5, 3, 1, 0.75 and 0.5 metres were investigated where it was found that a radial boundary smaller than 1 m affected the parameters. Even though the implementation of this study was effective and results were obtained on these effects, the complete set of results will not be presented here. It was realised that the simulations performed would not reflect the true boundary interactions of a rotating rotor since the boundary conditions at the inlet for this study were imposed perpendicular to the boundary. Implementing the inlet boundary condition in this way produced a wake which followed directly behind the airfoil which is fundamentally different to the circular trailing wake expected of the rotor blade.

The mesh independence study conducted in Section 3.3 gave some idea of the meshing required around the airfoil, however this study was only completed at the single Mach 0.3 speed. Even though mesh independence was performed at this speed alone, the selected mesh was used for the remainder of the studies including the cases which considered Mach 0.5. Another quantity used to assess the applicability of the mesh in resolving the boundary layer is the y^+ value. If one recalls, wall functions are being used which means that the inner layers of the boundary layer do not need to be resolved in the mesh and is adequately modelled as long as the first layer of cells are situated such that the y^+ is evidenced between 30 and 500. Table 3-2 presents the values for y^+ over the entire airfoil when simulations were performed using the pimpleFoam solver and the SA turbulence model using the mesh selected

in the mesh independency study and used through all the investigative studies at both speeds. It is clearly observed that the mesh suffices in representing the boundary layer and thus the flow at both speeds. The minimum value at Mach 0.3 of 25 is slightly below the recommended limit but it is evident that the generated mesh can be used as guidance to setup the mesh for the final rotors. Knowing what height is required for the first cell off the rotor wall and using this to develop the mesh will assure that the entire rotor is modelled with appropriate mesh resolution in the vicinity of the wall. These results conclude that for the rotor setup, the height of the first cell off the rotor wall should fall within 0.65 mm - 0.9 mm in order for the solution to abide by the law of the wall.

Table 3-2: Values of y^+ over airfoil for simulations at both representative speeds

	Values of y^+		
	Minimum	*Maximum*	*Average*
Mach 0.3	25.73424	113.2864	89.25560
Mach 0.5	44.69719	209.1315	166.6473

3.7 Conclusion

A number of investigative studies were conducted to compare parameters for their applicability in modelling the full rotor simulations. Results were not only evaluated against one another but were also compared to data from literature to validate the results against numerical and experimental results. The studies produced results which represent actual phenomena to an acceptable degree where discrepancies resulting from different chord lengths, mesh resolutions, wall functions, turbulence models and solvers were discussed.

It was concluded that using an incompressible transient solver for turbulent flow in the form of pimpleFoam to resolve the zero pitched rotor will provide sufficient modelling for the purposes of this study. Furthermore, the Spalart Allmaras turbulence model and the nutUSpaldingWallFunction for wall treatment are acceptable for use. Finally, the mesh independence study and y^+ values for the representative speeds of the rotor provide a foundation on which the mesh can be constructed for the full rotor model to resolve the flow suitably.

Chapter 4 – Rotor Simulations and Fault Identification

Completion of the experimental study and acquisitioning of data as well as the presentation of investigative studies to select appropriate numerical parameters allowed the full rotor simulations to commence. Possessing a firm understanding of the modelling requirements for the rotor, the simulation case was constructed. In this Chapter, the case construction is described in terms of the geometry definition for both the healthy and the mistracked rotors, the domain extents, meshing strategy, solving strategy and other components which make up the case structure. The results produced for the healthy rotor are compared to the experimental results of Chapter 2 for validation in which good correlation shall be seen. Differences between the results for the healthy and mistracked blades are described to demonstrate the applicability of using flow field quantities for fault detection. Finally, remarks on the numerical proficiency and the computational expense experienced in implementing the simulations are reported.

Note, two full rotor simulations were executed in this investigation. The simulation relating to the perfectly symmetric rotor will be referred to as the healthy simulation whereas the simulation relating to the rotor with a mistracked blade shall be referred to as the faulty simulation.

4.1 Simulation Case Setup

Pre-processing steps including the generation of the rotor geometries and their domains as well as the meshing strategy pursued are described. The contents of the OpenFOAM case files prepared for the simulations are briefly discussed along with the strategy followed once solving began.

4.1.1 Rotor Geometry and Domain

Firstly, it is important to have a good understanding of the co-ordinate system used for the rotor models. Figure 4-1 summarises the rotor model setups simplistically so that the axes can be described appropriately. The axes shown in the figure describe the global co-ordinates of the rotors in their original setup (at time zero). Rotation was prescribed about the positive y-axis. In this initial configuration, the blades extended radially into the z-axis. The selected faulty blade and the direction in which it was geometrically modified is shown by the arrow.

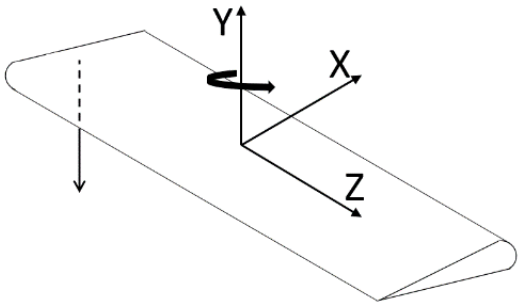

Figure 4-1: Simplified rotor to describe coordinate system

The rotor geometry was defined by following the specifications provided in Chapter 2 and using the scaled version of equation 3.3 for the NACA 0012 airfoil with a 185 mm chord length. Figure 4-2 portrays the model generated for the healthy rotor. Spanning from a radius of 270 mm to the tip of the blade, the NACA 0012 airfoil maintained a constant profile without twist. The rotor geometry was simplified from the true geometry to exclude unnecessary details as is usually done in CFD implementations.

Simplifications include the modelling of the hub region as well as the removal of the trim tab. It is understood that the trim tab effects the aerodynamics of the rotor but it is not within the scope of this investigation to study its effects directly. This study considers the overall effect of blade mistracking which may be effected by trim tab arrangements and can be considered independently in further investigations. It is also true that since this study is purely considering a CFD analysis, the rotors are modelled as rigid. This is done to avoid the complexity of dealing with the flexibility of the composite rotor.

Figure 4-2: Healthy blade model

Figure 4-3: Healthy and faulty blade models showing offset blade

The faulty (or mistracked) rotor was modelled identically to the healthy rotor apart from offsetting one of the blades. Figure 4-3 shows both the healthy and faulty rotor blades where one can see the geometric offset that has been imposed to one of the blades in the faulty configuration. At time zero, the blade situated in the negative z-direction was offset by 4° into the negative y-direction.

After modelling the rotor geometry, the domain was defined to set the extent of the boundaries wherein the fluid flow will be solved. Figure 4-4 shows the domain modelled around the rotor blade. The rotor was situated at the centre of a 3.86m diameter and 1m high cylinder implying that the rotor tip was a radial distance of 1m away from the boundary and the symmetric rotor chord line was a normal distance of 0.5m from the boundary. The boundary locations were approximated according to the study described in Section 3.6 but comments were made about the eligibility of this study in representing the flow field of the rotating blade. Knowing the prescription of the first cell height off the blade from the studies in Chapter 3 gave an indication of the mesh density that would be required. With this in mind, the boundary locations were not extended to keep the computational expense of the simulations within reason. Using the domain described in Figure 4-4 does have the advantage that it resembles the experimental setup of the rotor in the laboratory to some degree as the radial boundaries emulate the restriction of the walls.

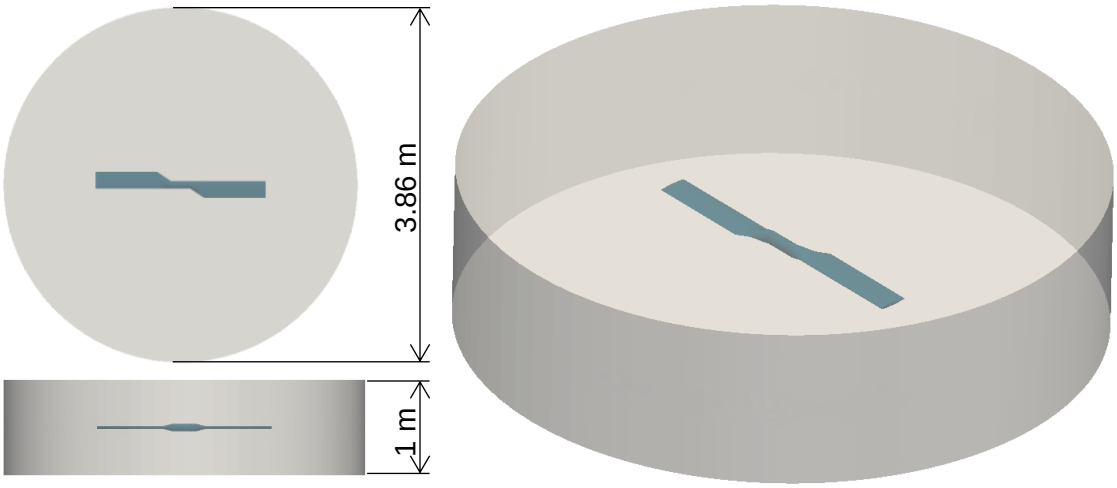

Figure 4-4: Boundary locations for domain around rotor model

4.1.2 Meshing

Seeing that the height of the first cell off the wall was known from the investigative studies of Chapter 3, this was treated as a priority in the meshing phase since mesh independence studies and reruns at this level would be unlikely and costly. The domain around the rotor was sectioned into blocks to allow better control of the meshing and in almost all regions a structured mesh was sought after. A dominantly structured mesh was set as a target to acquire good mesh quality and thus a good solution. The mesh cell heights were linearly stretched such that areas anticipated to have high gradients and require good resolution were biased to have smaller cell heights. The mesh stretched from these regions with the prescribed cell height off the wall to the boundaries reducing the number of cells generated in the mesh and saving computational expense.

Figure 4-5 provides a number of screenshots of the mesh that were generated for the healthy rotor where the meshing strategy described above can be seen. The mesh is stretched normally to focus more cells nearer to the blade as well as radially from the boundary to the tip and from the rotor hub to the tip to focus cells near the tip. This ensures that the tip of the blade, its wake and the flow field in the direct vicinity of the rotor blade is resolved well. A mesh of approximately 7.2 million cells was produced.

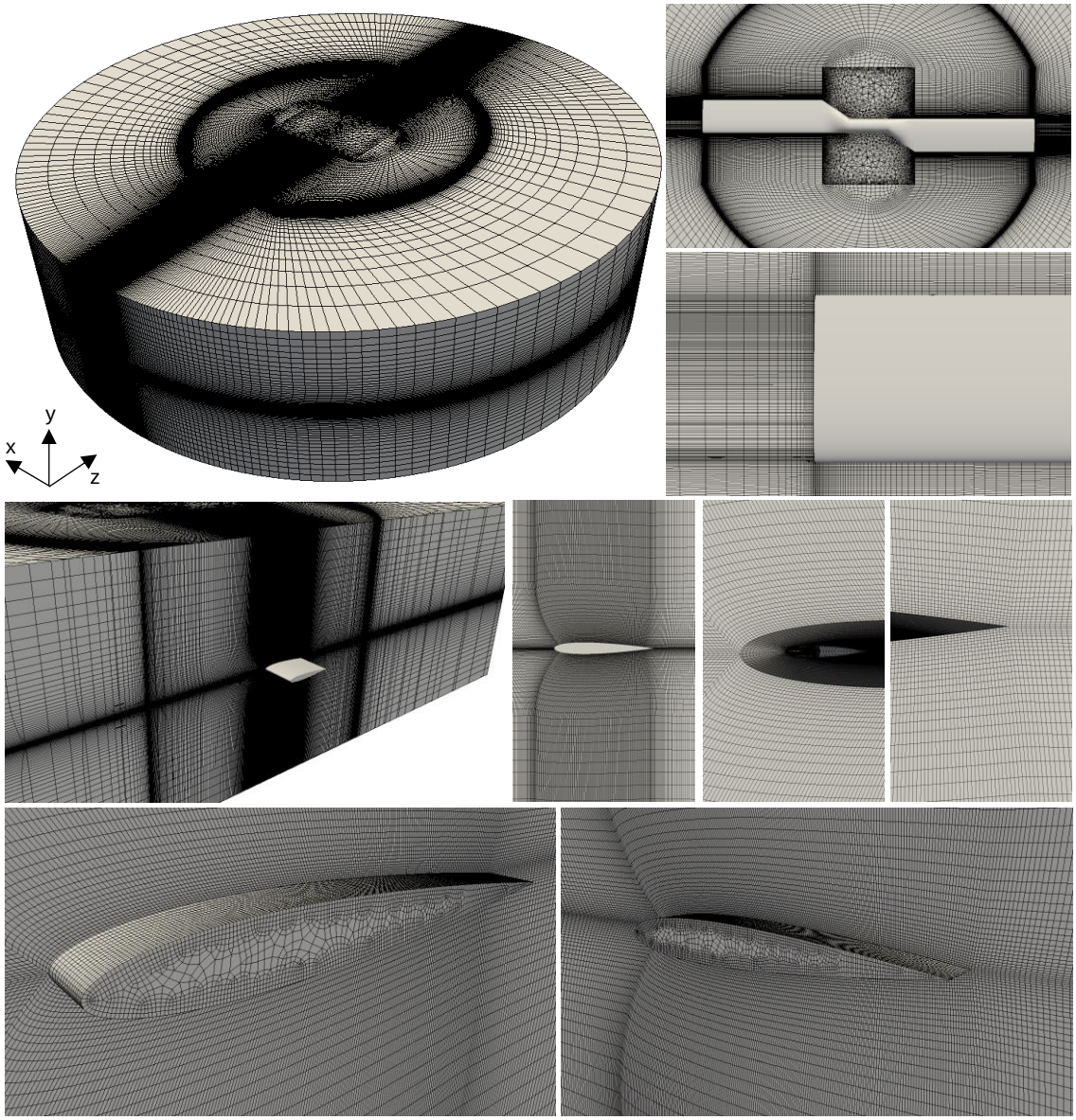

Figure 4-5: Mesh generated for healthy rotor

Figure 4-5 reveals that in most regions, the mesh is structured and of good quality as desired, with the exception of the centre region where the hub is located. This centre square region meshes the domain for the radial locations at which the NACA 0012 profile begins on the blade. A general rule of thumb when generating meshes for CFD is that the transition from one cell to the next should not experience a length change greater than 30%. This is obeyed throughout the domain except for the transitioning of the mesh from the other regions to the hub region. If this issue of transitioning from other portions of the domain to the hub could be rectified then there would be no other issues in the meshing but this could not be rectified without affecting the remainder of the meshing approach and severely impacting the mesh quality metrics. Exceptionally poor quality metrics resulting from adjustments to the above meshing approach prevented the simulations from starting as they were too unstable, therefore the mesh depicted in Figure 4-5 was used for the simulations understanding that the mesh in the hub region could be done better. It is also the case that fluid dynamic information produced at the hub is not of concern but the possible effects of the meshing produced in this region on the simulation as a whole must not be disregarded.

4.1.3 Case Structure and Solving Strategy

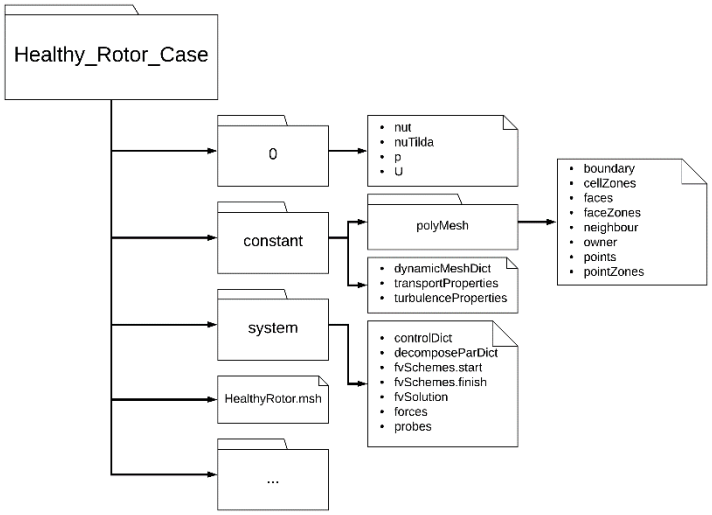

Figure 4-6: Breakdown of simulation case structure

The required files and directories to run the simulations are broken down and provided in Figure 4-6. The zero directory provides the boundary conditions and initial conditions for the pressure, velocity, turbulent viscosity and turbulence field variable fluid properties. The nutUSpaldingWallFunction was prescribed in the turbulent viscosity file with other turbulence properties prescribed according to the original derivation of the Spalart Allmaras turbulence model which are a function of the far field kinematic viscosity for air. A meshing file (.msh) was generated for each rotor and placed inside their respective case directories. The meshes were converted so that the polyMesh directory could be created containing all the necessary text files detailing the mesh. A rotational speed of 191.64 rad/s (1830 RPM) was prescribed in the dynamicMeshDict for the rotors while the viscosity for air and the Spalart Allmaras turbulence model were prescribed in the remaining files in the constant directory. The system file contained files to control the time steps and running of the simulations, the decomposition of the case for parallel computing, the selection of discretisation schemes and solving algorithms as well scripts to define the recording of rotor forces, moments and to probe fluid data in the field. The case files discussed above are provided in Appendix A. Each case also had extra scripts which were written to run the case and monitor the convergence of the simulations.

The locations at which pressure and velocity were probed in the field of the rotor are shown in Figure 4-7. Probes 0 to 5 correspond to the experimental locations of Chapter 2 at which data were captured in the field of the blade.

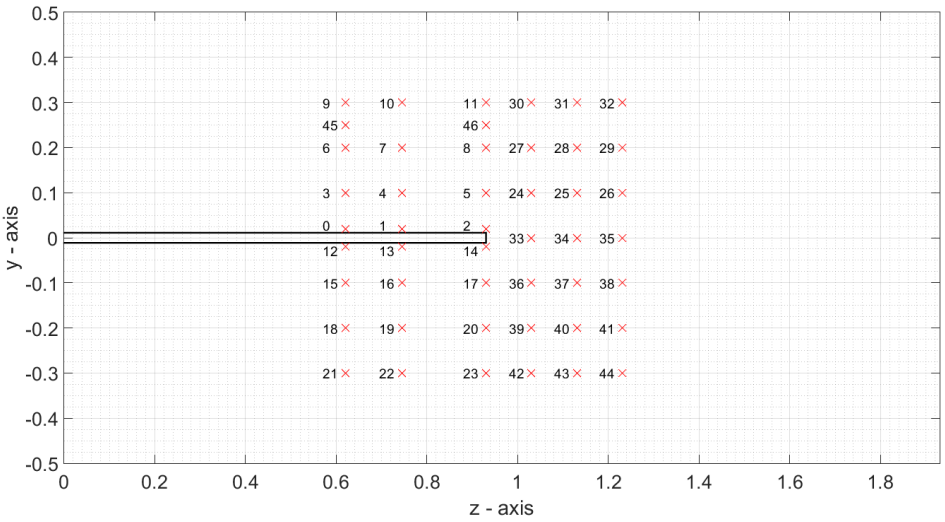

Figure 4-7: Locations of simulation probes in domain

The Centre for High Performance Computing (CHPC) based in Cape Town, South Africa provided the computational resources on their Lengau Dell Linux cluster to run the simulations. The cluster has a total of 1368 compute nodes, each of which has 24 cores and between 64 to 128 GB of memory. The cases were decomposed into 120 subdomains and run on the cluster in parallel. The pimpleDyMFoam solver was used which allowed the mesh to rotate dynamically producing incompressible transient results. When there are concerns about numerical stability it is suggested to start the simulations with first order discretisation schemes (defined in fvSchemes.start) allowing numerical transients to dissipate and lowering the risk of divergence. Once the simulations had dissipated any erratic transients, second order discretisation schemes (defined in fvSchemes.finish) were used for the remainder of the solution. Of course, a big concern when performing transient simulations is the specification of the time-step used as this dictates stability and time resolution of the simulation. The feature in OpenFOAM which allows the specification of running the simulation with a maximum courant number as opposed to a fixed time-step was used. The time-step is continually adjusted to ensure that the maximum courant number throughout the domain is maintained at the specified value. This can be beneficial since the time step will start low and rise till it converges as the simulation converges making the simulation more efficient and stable than adjusting the time-step manually. As an extra means of ensuring stability, the maximum courant number prescribed for the simulations was ramped as the simulation commenced.

For the computational resources used for the simulations and the solving strategy implemented, the simulations were still demanding requiring numerous runs. A simulated time of approximately 0.024 seconds took 48 hours to compute when using 120 cores on the cluster. The solving strategy could not be adjusted too much to speed up the runs since increasing the maximum courant number resulted in the simulation diverging. At this stage, the simulations were left to run and restarted in 48 hour increments until convergence was acquired.

Convergence of the simulations were monitored using a number of parameters. The residuals of the field variables were monitored as well as parameters such as the force and moments on the blade. Field variables such as the probed pressures and velocities could also be plotted to interrogate their behaviour as the simulations commenced. One should understand that plots of these variables indicate fluctuations which can still

represent converged solutions since a transient analysis is being performed and time-dependent data is anticipated. The solution is thus deemed converged when these fluctuations become consistent and are seen to exhibit ordered fluctuations. Finally contours at slices of the domain for different times were compared to assess any large deviations. Figures 4-8 and 4-9 illustrate the convergence of the faulty simulation when monitoring the residuals and slices of the domain over time instances. A number of other convergence plots for both simulations are provided in Appendix B. Figure 4-8 reveals a number of large spikes which occur throughout the simulation, it is imperative to understand that this is not being modelled physically but is a numerical issue which occurs every time the simulations had to be restarted. When the simulation needs to restart, it does not have the information for the time-step exactly before it which produces an instability. These instabilities dissipate but are seen in all of the time-dependent data recorded and its presence will be seen in all of the data presented in this chapter.

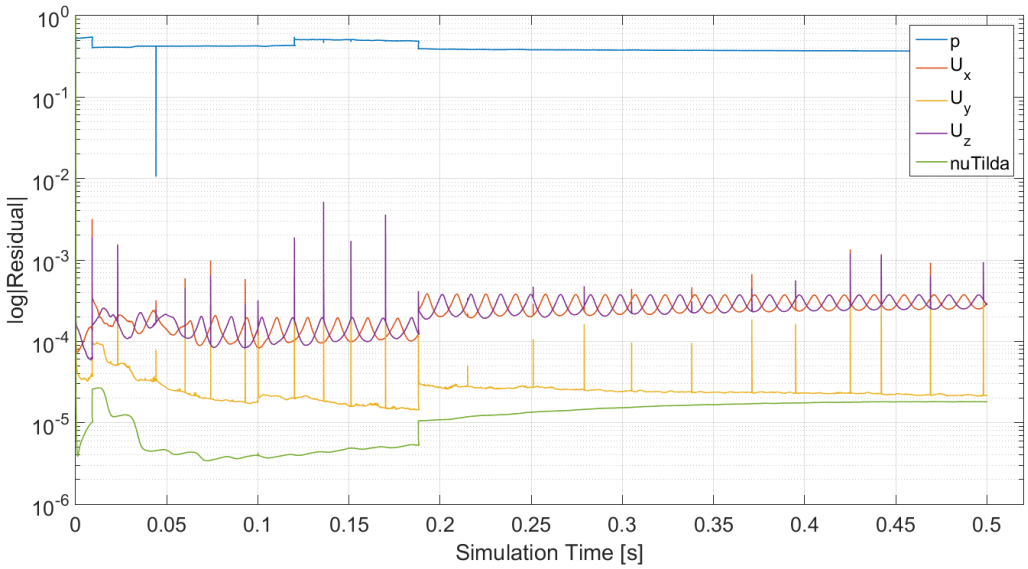

Figure 4-8: Residual plot over simulation time for faulty simulation

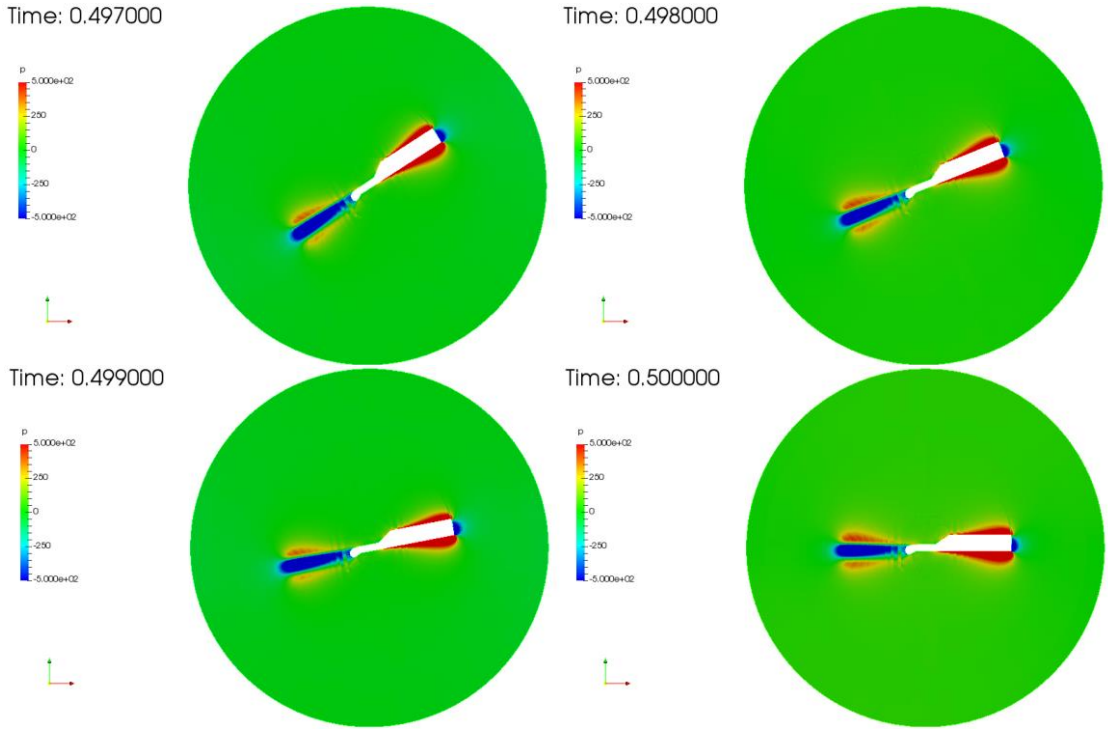

Figure 4-9: Pressure field (P/ρ) at different time instances for faulty simulation sliced at domain centre

4.2 Validation of Results

The numerical results produced by the simulations for the healthy rotor blade are compared to the experimental results produced in Chapter 2 for validation and to assess the integrity of the simulations in representing the physical phenomena. Validating the simulations also provides a basis on which model based condition monitoring and fault detection can be used to represent actual scenarios. The pressure results recorded at probes 0 to 5 in the simulations were processed by filtering the data to use the converged time frames, subtracting the mean of the signal (to remove any DC offset) and converting to pascals by multiplication with the density of air (OpenFOAM records pressure data as pressure divided by density when using incompressible solvers). Damping of the numerical instabilities caused by the simulation restarts was then performed before the signals were time-synchronously averaged and plotted against the experimental results. Figure 4-10 compares the time-synchronously averaged signals over a single revolution for the experiments and the healthy simulation at probes 0 to 5. The maximum and minimum values recorded during the experiments are also plotted as dotted lines.

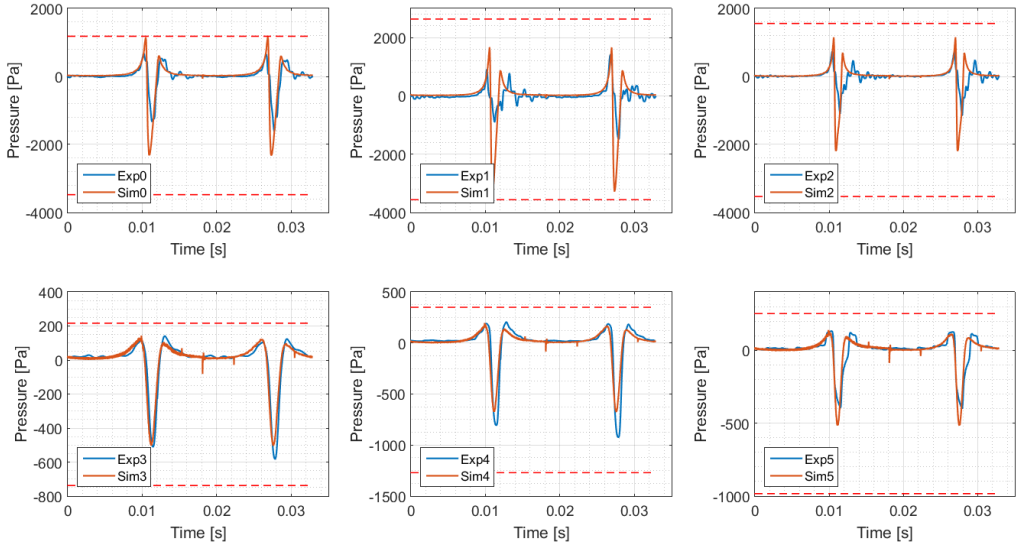

Figure 4-10: Comparison of experimental and numerical pressure profiles

Overall one could say that the numerical results compare fairly well with the experimental results. The simulations predict the crests and the troughs of the pressure profiles at each location reasonably well. Probes 3 to 5 appear to match the experiments better than probes 0 to 2. However, experimental probes 0 to 2 feature a larger variance in its peak values which is evidenced by the difference between the maximums, minimums and averaged signals at each probe as well as the presence of the fluctuations inherent in the averaged signals, specifically after the blade had passed. These fluctuations are not well represented by the simulated probes which is most likely due to the limitation in using URANS modelling as it would not be able to model disturbances at these frequencies. Even though these discrepancies are present, the numerical results at these closer locations are still within reason of modelling the pressures at these locations as they represent the experimental signals appropriately and are within their maximum and minimum bounds. A visible distinction is also seen at probes 2 and 5 since these probes are situated at the tip of the rotor. Again, disturbances effect the profile of the experimental pressures but the simulated signal of probes 2 and 5 resolve the drop in the pressure peaks at these locations in comparison to the peaks at probes 1 and 4. The numerical results at probes 3 and 4 resemble the experimental results impeccably. It is compelling to see that the numerical results produce troughs which are near identical for each blade passing while the experiments do not, this shall be addressed in more detail in the next section when the healthy and faulty simulations are compared for fault detection. Small spikes observed in some of the numerical results are again attributed to the instabilities caused by simulation restarts which could not be completely damped.

It is also of interest to comment on the pressure profile that develops in each case. Each of the profiles as the blade passes can be compared to the pressure coefficient profiles used for the blade in Chapter 3. As the blade approaches, the pressure increases which is followed by a steep pressure drop that recovers over the blade surface as was seen in the pressure coefficient plots. These physical phenomena occur as a result of the pressure peaking at the leading edge where there is a stagnation point while the velocity drops transferring its energy into potential (pressure) energy. This energy is transferred back into kinetic energy as pressure is relieved once the flow passes the stagnation point. The influx of potential energy accelerates the flow causing a sudden drop in the pressure field. Recovery in the form of the balance between the velocity and the pressure occurs over the length of the blade surface and past its trailing edge. Furthermore, the difference in the DC offset between the experimental and numerical results was in the order of 200 Pa which is small and could be due to a factors such as altitude. These comments support the capability of the numerical results in representing the physical phenomena exhibited by the blade.

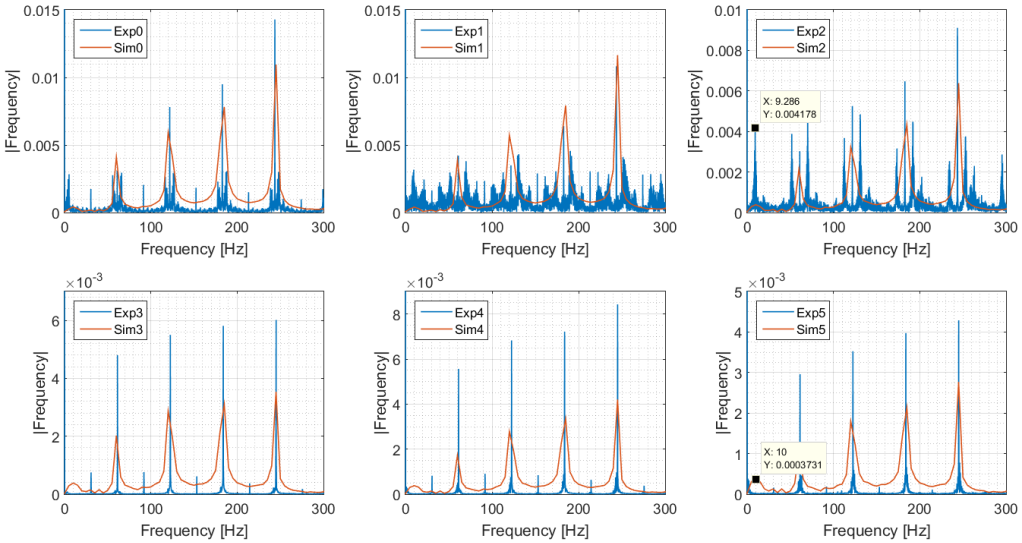

Figure 4-11: Comparison of experimental and numerical frequency content

Each of the simulated pressure results were then transformed into the frequency domain so that they could be compared to the experimental frequencies that were captured. Figure 4-11 compares the frequencies for the experiments and the healthy simulations at probes 0 to 5. Be aware that the numerical amplitudes had to be scaled for the comparison, so it is only the peak frequency components that are of interest. Nevertheless, the comparisons of the frequencies show that all of the numerical probes predict the blade pass frequency and all of its harmonics well correlating with the experiments. The numerical probes do not observe frequencies at the rotational frequency, which is expected since the healthy simulation had near identical profiles for each blade passing thus identifying the blade pass frequency only. Chapter 2 identified that the blades on the rotor test bench did not track perfectly explaining the presence of frequency components at the rotational frequency for the experimental results. Note that the numerical results predict a low frequency component at approximately 10 Hz but do not display any sidebands like the experimental work. This may prove that the low frequency result of 10 Hz is due to aerodynamic delay (as alluded to in Chapter 2) which is modelled well whereas the sideband frequency may be indicative of the blades flapping or vortex shedding which the current simulation is incapable of modelling due to the rigid rotor assumption and the use of RANS turbulence modelling.

It can be concluded from this section that the numerical results correlate well with the experiments and thus model physical phenomena well. Frequencies caused by occurrences such as blade flapping or fluctuations from other fluid dynamic behaviour cannot be modelled but are not of interest. The results indicate that pressure troughs and frequencies in the order of the rotor rotation and blade passing are modelled well and are of more interest in the light of fault detection.

4.3 Fault Detection

It has been shown that the numerical results approximate the experimental results quite well. One can assume that the numerical simulations represent the physics appropriate to this investigation adequately. Comparison of the results delivered by the healthy and faulty simulations can be conducted to assess the flow field information to see in what ways the blade asymmetry can be inferred and thus detected. The literature in Chapter 1 outlined relevant investigations which dealt with fluid dynamic modelling of machine faults. The majority of these investigations considered fault detection by analysing the power output and apart from investigations which considered noise analyses, none considered the implications on the fluid dynamics.

First, the moments and forces are analysed to assess the effects the fault considered in this investigation cause. A pressure probe analysis follows which again considers the pressure profiles and frequency content at selected probes thereafter other probes in the field are assessed for their sensitivity to dictate how far recordings would need to be taken before fault detection capabilities are lost. Finally, a discussion is given on the pressures observed on the blade under anomalous conditions.

4.3.1 Force and Moment Analysis

In order to make sense of the force and moment information described in this section, it is necessary to revise the coordinate system described in Figure 4-1. The dynamic mesh model used in the simulations rotates the entire mesh during the simulations where quantities are prescribed according to a stationary coordinate system, in other words, the coordinate system of Figure 4-1 is fixed as the rotor rotates about its y-axis. Results for the stationary frame (or global coordinates) shall be referred to as the hub results since forces and moments of this type would be measured at stationary locations situated at the hub of the rotor system. Alternatively, results which make reference to the blade refer to a local coordinate system which 'follows' the blade as it rotates. This corresponds to measurements taken on the blade throughout its rotation. The blade results were determined by performing a coordinate transformation of the hub results for the x and z components as the blade rotates.

Figure 4-12 gives the results acquired for the moments for both the healthy and faulty simulations at the hub and blade reference frames. Considering the hub loads first, the healthy rotor illustrates minute fluctuations around 0 for the x and z-components while reporting a mean value of -24 Nm for its y-component. These values reflect the healthy simulation well since values of 0 for the x and z-components reflect the blades symmetry

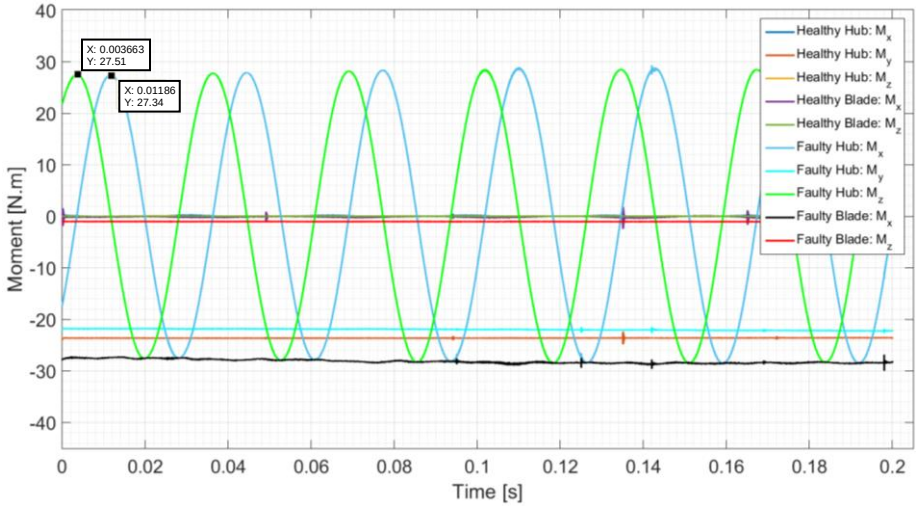

Figure 4-12: Comparison of healthy and faulty rotor moments for hub and blade reference frames

while the larger negative value for the y-component reflect the torque required to rotate the blade. The x and z-components transformed to the local blade reference frame reflect similar findings with mean values of 0 reported.

Comparing the results for the faulty blade at the hub, considerable differences are observed. The x and z hub components fluctuate between high moment values. These two components are phase shifted by a 90° rotation of the blade which is clearly based on the time instances at which the measurements align with the hub (global) coordinate system. It is also intriguing to note the minor decrease in the y-component for the faulty rotor at the hub. The transformed x and z-components for the faulty rotor show that in a reference frame which follows the blade, there is a small negative z moment and a large negative x moment. Referring back to Figure 4-1 and considering the imposed fault, these conclusions are logical as the lift of the two mistracked blades are enforced in two different planes causing a twist about the x-axis.

Transforming each of these signals into the frequency domain reveals that there are no other noteworthy frequency components apart from large amplitude increases in the x and z hub components at the frequency of the rotational speed. This is apparent by simply observing the trends shown in Figure 4-12.

Table 4-1 gives a breakdown of the mean force and moment values computed for the healthy and faulty rotors in each reference frame. Analysing the results for the forces experienced at the hub and blade reference frames presented similar findings. The only difference between the force and moment analyses are the components which express the anomaly. For example, the x blade moment expresses the fault attempting to turn the blade about the x-axis while the z blade force expresses the blade being pulled toward the positive z-axis with these two related. Due to the similarity of the force results, they are not presented to avoid repeatability.

Table 4-1: Healthy and faulty rotor mean force and moment values

	Hub (Global)			**Blade (Transformed to Local)**		
	x	*y*	*z*	*x*	*y*	*z*
Healthy Force	-0.0041	*1.9064*	0.0081	-0.0301	-	0.0179
Faulty Force	0.0130	1.7737	0.0374	-0.9469	-	1.8849
Healthy Moment	-0.0155	-23.6142	-0.0772	-0.1493	-	0.0003
Faulty Moment	-0.1233	-21.9709	0.7975	-28.1531	-	-1.0320

Section 1.2.5 identified numerical investigations which have performed CFD analyses under faulty rotor conditions. Most of these studies used the force and moment (or torque) information for fault finding and nothing else. The results described above for the helicopter rotor simulations serve as a further proof of these analyses since it confirms that the presence of a fault increases the 1/rev amplitudes of force and moments encountered which the studies in literature also found. However, acquiring these measurements practically for condition monitoring purposes is difficult and, where possible, does not eliminate the issue of identifying the specific fault since most rotor faults would manifest in this response. Measurements on the blade are undesirable due to their complexity and expense. A dynamometer could be used to monitor the torque of the rotor but this component did not provide much diagnostic information and would be difficult to implement. It would also be difficult, if possible, to measure force and moments about the other axes at the hub of the rotor. Finally, increases in the 1/rev force and moment amplitudes would result in vibrations at this frequency which could be measured in the aircraft. This is already done in rotor track and balance procedures and although the vibration levels could signify a fault they do not aid in identifying and isolating the specific fault. It can be concluded that force and moment data does provide diagnostic information but is difficult to implement practically which serves as motivation for seeking

alternative means of rotor fault detection, where fluid dynamic monitoring may have the potential to be a simplistic, cheap and viable option.

4.3.2 Pressure Probe Analysis

Pressure probe results are compared in the time and frequency domain between the healthy and faulty simulations, similar to the analysis described for the comparison between the healthy and experimental investigations. Figure 4-13 compares the time-synchronously averaged signals over a single revolution for the healthy and faulty simulations at probes 0 to 5.

To varying degrees, each of the probes in Figure 4-13 show a clear reduction in the pressure trough when the faulty blade passes. A reduction (as opposed to an increase) in the trough is expected since all of the probes pictured are situated in the positive y-axis while the blade was deflected into the negative y-axis. All of the probes exhibit a decrease in the amplitude of the trough of over 30% with respect to the healthy profile. This phenomenon clearly demonstrates that a rotor which is out of track is expressed as non-symmetric troughs in the time-domain. This is substantiated by the results produced in Section 2.3 where the experimental pressures were non-symmetric having been recorded for a rotor which was out of track. One should also note the phenomenon of the slight amplitude increase for the blade that tracks perfectly on the faulty rotor in comparison to the stable symmetric troughs for the healthy rotor. This might be caused by the perfect blade rotating through flow that is more orderly than when it passes through the other blades wake, causing an adverse pressure gradient and disturbing the flow more.

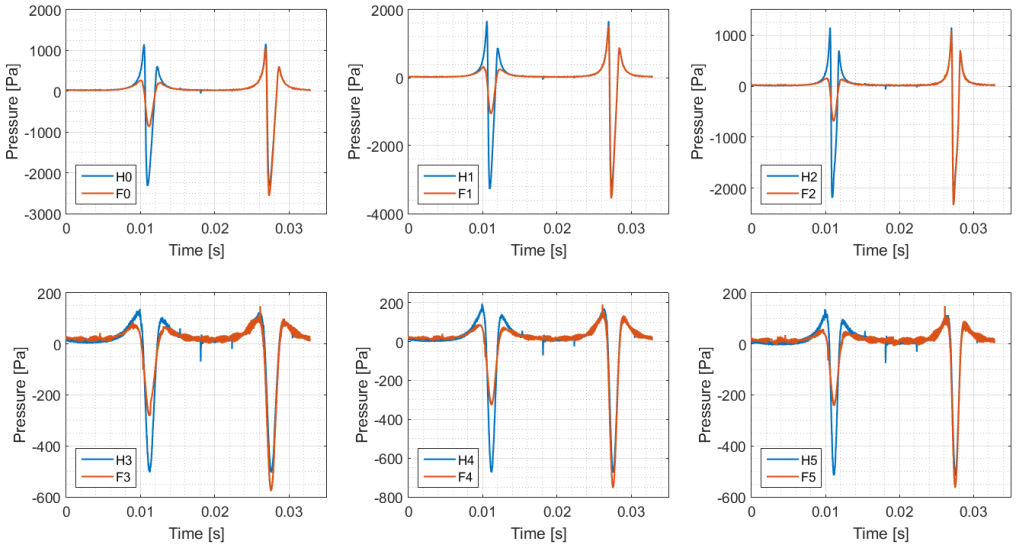

Figure 4-13: Comparison of healthy and faulty pressure profiles

Figure 4-14 compares the frequencies for the healthy and faulty simulations at probes 0 to 5. It is clear that the fault arises as increases in the amplitudes of the frequencies at the rotational frequency of the rotor (1/rev frequency). This is again supported by the results produced in Section 2.3 since frequencies at the rotational frequency were observed for the out of track rotor. Comparing the 1/rev frequency amplitudes exhibited at each probe location, probes 0 and 1 have similar amplitudes and are the highest amongst all the probes. Probes 3 and 4 also reproduce similar amplitudes but are smaller than probes 0 and 1 since they are located further away from the blade. Probes 2 and 5 see major reductions in their amplitudes in comparison to their rake counterparts and can again be attributed to the loss in pressure due to tip vortices. All probes for both rotor configurations display high frequency amplitudes at the blade pass frequency and

its harmonics. The pressure signals for the faulty blades appear to decrease the amplitudes of the harmonics at these frequencies slightly.

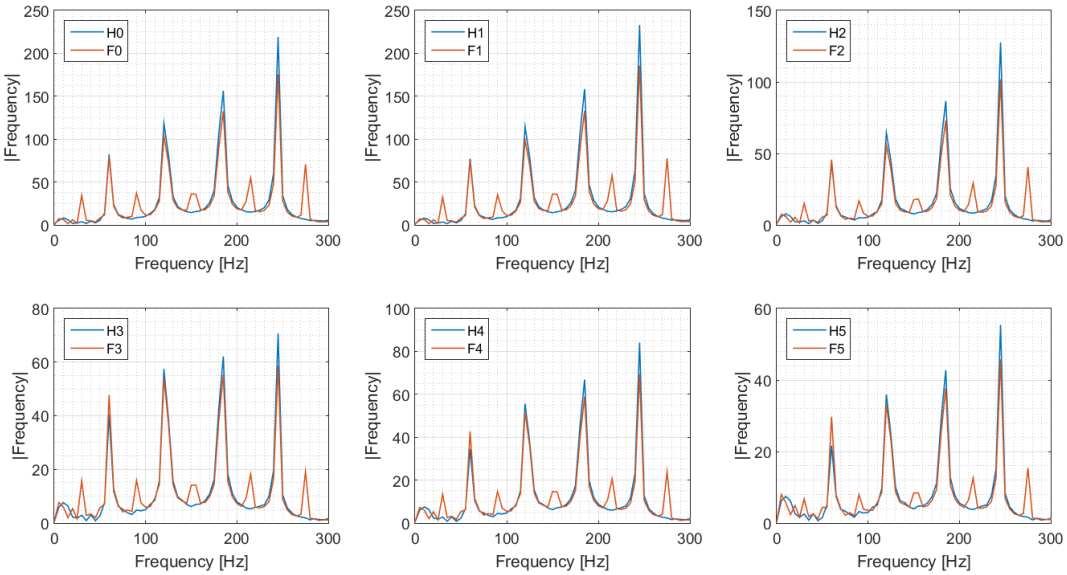

Figure 4-14: Comparison of healthy and faulty frequency content

The above discussion proposes fault detection features from simulated pressure data presented as a time-synchronously averaged signal and in the frequency domain. The use of a rigid rotor assumption and RANS turbulence modelling means that the simulations are not capable of representing phenomena such as blade flap and vortex shedding. This means the model fails to represent components of the pressure signal which are realistic contributors as seen in Section 2.3. One might argue that these components could deteriorate the fault detection capabilities of the features introduced above. However, even though the simulations are not able to replicate certain phenomena they demonstrate the response of the fault mechanism independent of the effects of blade flap and vortex shedding. This means that the fault is easily observed as the primary source of the features identified. It is also the case that the phenomena which are absent in the simulations presented themselves through other features such as the sidebands of the carrier frequencies which are not present in this analysis nor important to the fault detection strategy mentioned. Another consideration of how the results might be effected could be due to the neglected phenomena on the troughs of the pressure signals in a practical environment. Figure 2-12 showed considerable variance in the pressure troughs which may have been a consequence of the blade flap or vortex shedding but Figure 2-13 did not. One might say that the time-synchronous averaging is necessary since it separates the discrete and random components of the pressure signal, where the random components include the blade flap/vibrations and the vortices which cause the signal to fluctuate as has been seen. This provides the averaged signal which can be analysed for its behaviour and to assess the presence of fault features. Confidence in the fault detection feature is drawn from the fact that the experiments of Chapter 2 were conducted under faulty conditions and was capable of detecting the rotor asymmetry despite the presence of these components.

Section 4.2 described the principle behind the pressure profiles in the time domain from a fluid dynamics perspective. This description supports how the fault presents itself in Figure 4-13 as the faulty blade passes further away from the probe locations producing smaller pressure gradients and blunter peaks in the profile. The asymmetry of the troughs corresponds to how the fault features in Figure 4-14. This description implies that, in theory, one might expect these features to depict the severity of the fault. Furthermore, these results prove that rotor asymmetry is presented as increases in the

1/rev frequencies but this would be the case for a number of aerodynamic based fault mechanisms. Comparison of the time domain pressure profiles for the different blades provides valuable information about the fault. In this instance, the faulty blade is seen as a proportioned version of the other blade. Suppose one of the blades has a pitch error, theoretically this would feature different changes in the pressure profile leading to a fault detection technique which is capable of identifying the type of fault present.

The results presented prove the capability of pressures recorded in the field of the rotor in identifying an asymmetric rotor. Furthermore, the signal processing performed indicates that it may aid future investigations to make comparisons in the averaged time and frequency domains. Time-domain results present pressure profiles which may be examined for specific faults based on the deviations observed. But with the information provided this cannot be confirmed.

4.3.3 Pressure Field Sensitivity

All of the pressure probe analyses which have been considered up until this point have been based on probes 0 to 5 in order to relate them to the experimental investigations. These probes were all located within a close proximity of the blade plane and positioned in radial locations which represented the outer half of the rotor blades. The results discussed in this section compare amplitudes of the pressure profiles and their frequency components for probes located in other parts of the domain.

Previous sections made comments on the different pressure levels recorded at the respective locations. Pressure probes 0 to 2 portrayed higher peak values in comparison to probes 3 to 5 which intuitively makes sense. Also, various results illustrated the inefficiency of the probes situated at the rotor tip in representing the pressure amplitudes found by the probes within the blade radius. Implying that probes at 67% and 80% of the radius predicted the anomaly better. Referring to Figure 4-7 for the probe locations, pressures probed at 80% of the blade radius will be compared to assess the degradation in the fault detection as one moves perpendicularly away from the rotor blade (probes 10, 7, 4, 1, 13, 16, 19 and 22). Also, probes situated in the plane of the rotor but extended past its radius (probes 33, 34 and 35) shall be compared as well as pressures at locations far away from the blade radius and out of the rotor plane (32, 29, 26, 38, 41 and 44). Figure 4-15 shows the results of the pressures at each of these locations and its respective frequency transformations for the faulty rotor only.

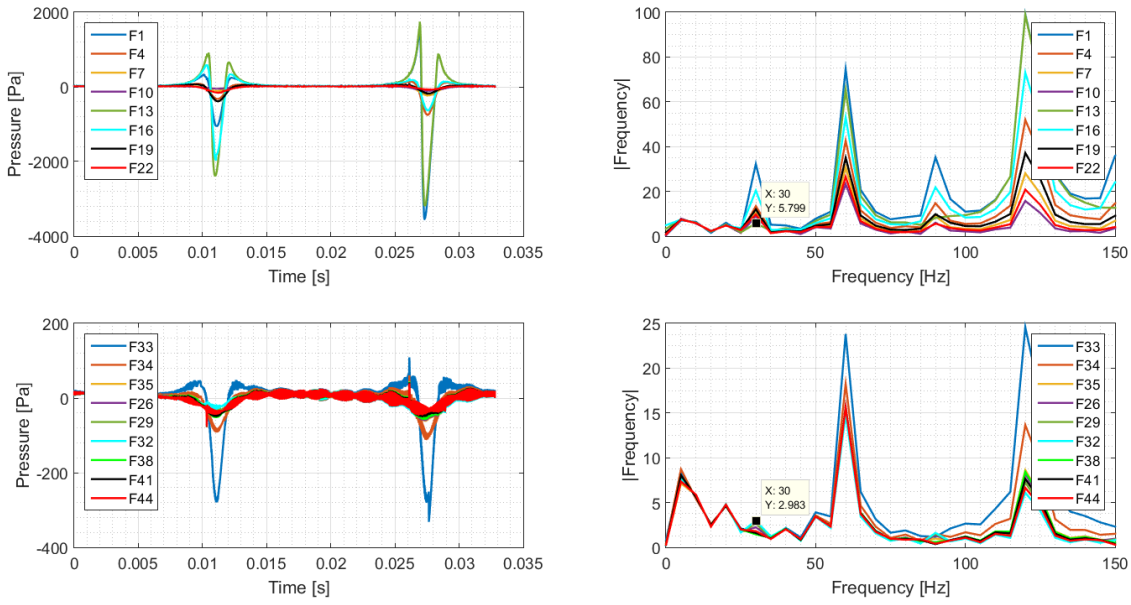

Figure 4-15: Comparison of faulty pressure profiles and frequencies at different probe locations

Comparing the pressure profiles of the probes recorded in line at 80% of the faulty rotor radius expresses the decay in the troughs as the probes move perpendicularly away from the rotor blade. The trough representing the perfect blade of the faulty rotor deteriorates with minimum values of 3500, 752, 230 and 110 Pa for probes 1, 4, 7 and 10 respectively. This shows that at a perpendicular distance of 0.3 m away from the rotor blade, a pressure probe would need to detect a pressure fluctuation smaller than 110 Pa which could very well be lost to external interactions and noise in practical applications. Nevertheless, the numerical results show that even with the smaller peak values, the frequencies at these pressure probes demonstrate that they are still capable of establishing the existence of the asymmetry since there are peaks at the rotational frequency of the blade.

Probe 13 produces peculiar results as it is located in a region where it records pressures below the perfect tracking blade and above the mistracked blade as they pass. This explains its poor performance in detecting the fault in the frequency domain having the smallest amplitude for these probes at a value of 5.8 for the rotational frequency. This probe is unrealistically situated and would not be used in any practical application.

Probes 16, 19 and 22 show similar trends to the probes discussed. However, these probes reflect the faulty blade as the higher of the two troughs for a single rotation. This is a result of the probes being situated in the negative y-axis with the faulty blade passing nearer them than the perfect blade. They show the same detection capabilities as the probes in the positive y-axis indicating frequency amplitudes at the 1/rev frequency.

Comparison of the results for all of the probes which extend further than the rotors radius signify inadequate fault detection. Not much can be distinguished in the pressure profiles plotted per rotation which is verified in the frequencies they produce. These probes do not identify the rotational frequency of the rotor well enough.

The results presented in this section recognised the incapability of detecting the fault using pressure probes located outside the radius of the rotor. It is seen that pressure measurements within the radius detect the fault appropriately. The loss in pressure peak values as measurements are acquired further away from the plane of the rotor was described. This concluded that the fault could be detected as one moved further away from the blade perpendicularly but results measured in practice would most likely be susceptible to other interactions and noise, skewing the results. One should also understand that the conclusions derived in this analysis are for the specialised case of a zero-pitched rotor and considering pressure information alone. A pitched rotor is bound to disturb the flow more and it is possible that other fluid dynamic quantities and noise can be acquisitioned in other locations depending on the phenomena and behaviours presented.

4.3.4 Blade Surface Pressure Comparisons

Investigations into the use of pressure sensitive paint to identify the presence of particular flow phenomena were described in the literature in Section 1.2.5. This was used as motivation for the study into fluid dynamic behaviour in the presence of a fault. This is so as it provides a practical grounds on which rotor monitoring and fault detection could be implemented if it is feasible to observe the fault from the blade surface pressures. Figure 4-16 compares the surface pressures along the blade for the healthy and faulty rotor systems. All of the contours are taken from the last time instance of the respective simulations. Comparisons (i) and (iii) show the results in the same configuration but plotted on different scales, the faulty blade on the faulty rotor is the right hand side blade with the fault imposed into the page. Comparisons (ii) and (iv) are given for the same configuration and represent the other side of the blade for configurations (i) and (iii) respectively. The fault in these instances are again on the right

hand side but protrude out of the page. The pressures are compared on different scales to show the fidelity for each pressure range used in observing the fault.

In all of the healthy instances, good symmetry is observed in the surface pressures between each of the blades. On the contrary, each of the faulty rotors show some irregularities between the blades. Figure 4-16 (i) shows a larger drop in pressure near the leading edge at the tip of the faulty blade for the specific pressure range. Although, a vast difference can be seen between the healthy and faulty surface pressures for (iii), it is difficult to identify the fault by only comparing the blades of the faulty rotor as done for (i). Similar comments can be given for the detection capabilities of (ii) and (iv) noting that (iv) performs better than (ii) which illustrates the effect that the specified pressure range has on observing the fault. The surface pressures also portray the difference in the pressure exhibited by the perfectly tracking blade of the faulty rotor (consider the left blade of comparison (iv)) from those on the healthy rotors which was explained in Section 4.3.2 as a result of the blades experiencing different upstream flows.

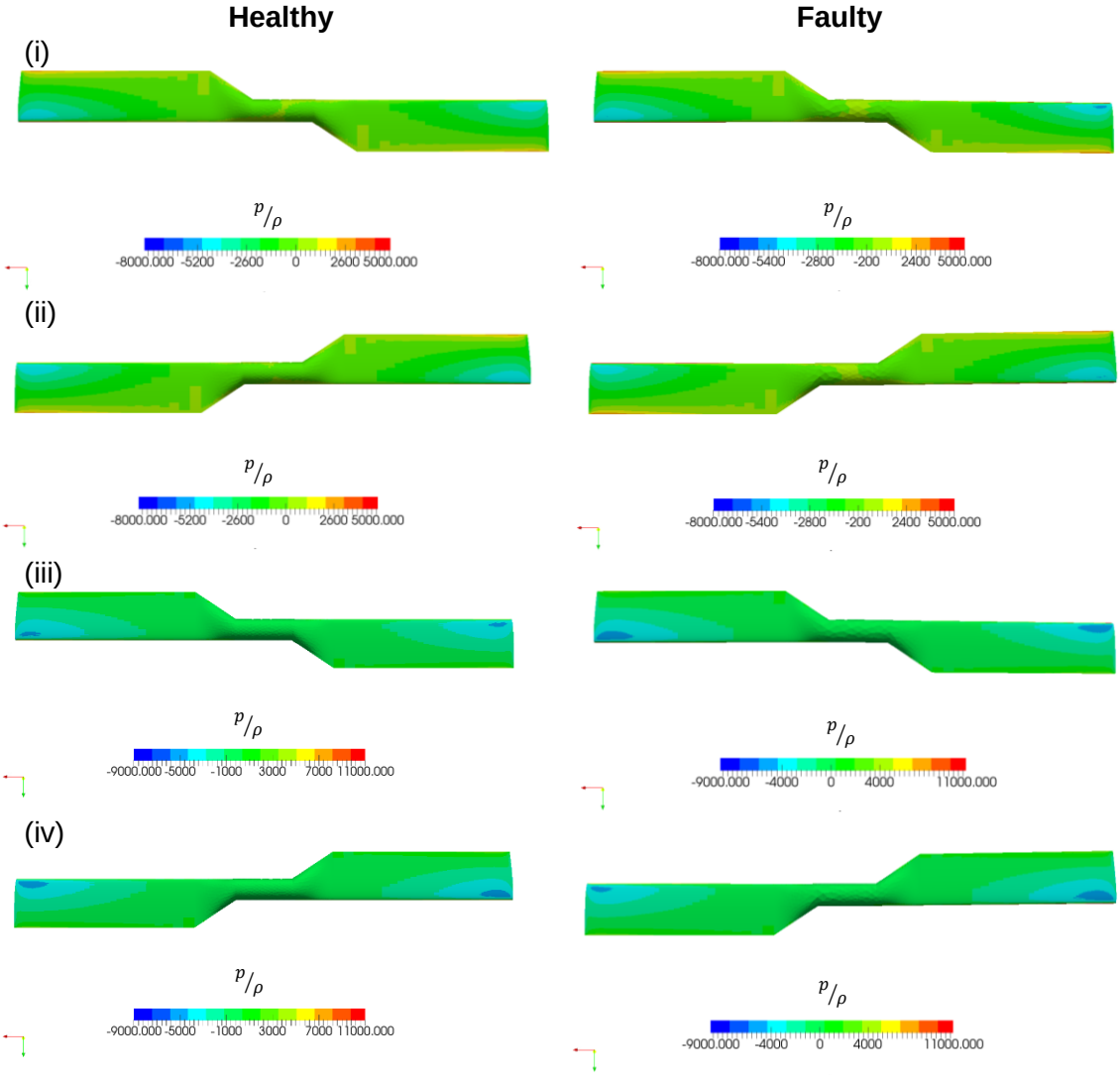

Figure 4-16: Comparison of healthy and faulty pressures over the surface of the blade

Implementation of such a monitoring technique would need to be considered carefully since the results established are particularly sensitive and in a practical environment may be incompetent due to noise and external interactions. Using pressure sensitive paint may become costly depending on the size of the rotor considered and the wear resistance of the paint. The response time of the paint to pressure fluctuations would

also need to be considered since a slow response would probably provide a mean of the fluid dynamic behaviour where individual time instances could be compared as is done in this instance. This may be satisfactory for a rotor in an ideal and steady environment. On the other hand, a fast response from the paint may portray fluctuations which are derived from the natural flow where careful consideration would need to be given for a fault detection strategy but could provide transient information. Having said this, another consideration would be the manner in which the data is acquired as it will most likely be necessary to use a high speed camera.

Still, this section expresses the plausibility of observing a fault by monitoring the surface pressures. The implications of using such a technique would have to be considered in further investigations understanding the fidelity of such a measurement technique. These conclusions are for the particular fault of mistracking where other geometric faults may demonstrate larger deviations, such as an incorrectly pitched blade.

4.4 Numerical Considerations

In constructing the simulations performed, one could say that a particularly economical model was produced in the context of using URANS to acquire the time-dependent information. This statement is deduced from the fact that wall functions and the one-equation Spalart Allamaras turbulence model were used as well as the assumption of incompressibility. These parameters can all be considered as cost-effective selections in comparison to other options available in their categories. For the particular rotor cases considered, it was shown that accuracy in the predictions of the fluid dynamic behaviour was not drastically curbed by these modelling decisions. The simulations produced results which reflected the rotor behaviour well.

Another parameter of the investigative studies of Chapter 3 which was used to setup the rotor simulations was the first cell height to generate the meshes. This prevented having to do mesh independence on the rotor meshes. Figure 4-17 provides a histogram of the y^+ values computed for the cells at the walls for both the healthy and faulty rotor simulations. Recalling that the y^+ should ideally fall between 30 and 500 when using wall functions, the histogram demonstrates that generating the mesh around the cell height prescribed in Chapter 3 maintained good y^+ results for both rotor simulations. The zoomed in portion of the histogram shows that there were a few cells that fell below the value of 30 but these would have been compensated for by the use of the nutUSpaldingWallFunction since it is a scalable wall function. It was found that cells which fell below 30 were situated near the centre of the rotor and were also found on the rotor where the mesh had poor transition from the outer blade to the inner hub region as shown in Figure 4-18. These results exemplify the fact that good CFD practices and fair modelling strategies were considered throughout the investigation.

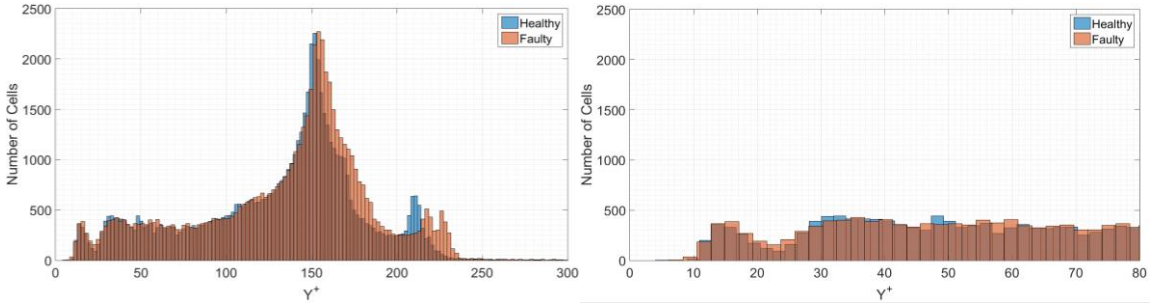

Figure 4-17: Histogram of y+ values for healthy and faulty simulations

Even though all of the mentioned considerations were taken into account in order to make the models economical, the simulations were computationally intense and took months to run. The simulations were run on high performance computers and parallelised between 120 cores. Having followed good practices throughout the reader is advised on a few considerations which may have helped in speeding the simulations up. Transient simulations are sensitive to the time-step used and although a maximum courant number was specified to dictate the time-

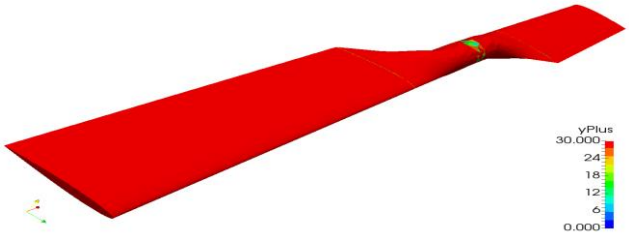

Figure 4-18: Cells with a y+ of less than 30 along the blade

step, there are a number of factors which effect the value. The mesh issue identified where poor transition is seen from the outer blade region to the inner hub region could be approached in a better way. The cells in this region were poor quality which effects the entire simulation and could be where the solution starts to diverge in the case of crashes. Their small sizes could have also been the direct result of the restriction on the time-step and preventing it from increasing. The histograms demonstrate that a large number of the cells produce a y^+ value around 150. The first cell height could be increased more such that the histogram shifts so that most cells produce a y^+ of 300. This will not degrade accuracy of the results but will drastically increase computational efficiency as the time-step will increase with the increase in cell height. The selection of discretisation schemes is also open to multiple options with the options prescribed for this particular study not being definite. One should consider revising the schemes to ensure that the most appropriate selections have been made or if scheme combinations with similar accuracy but more stability can be implemented.

Initially it was intended to study more instances of the rotor faults and possibly other fault mechanisms but the expense of the simulations prevented this. It is hoped that future work can consider further parametric studies and the consideration of other faults for this investigation but restricting the computational expense is important.

4.5 Conclusion

The approach used in constructing the healthy and faulty rotor simulations was discussed with descriptions given on the fault imposed, the generation of the rotor geometries and the boundary locations of the domain. The results produced by the healthy simulation were validated against the results recorded during the experimental investigations of Chapter 2. Good correlation was found between the results with the blade pass frequency and its harmonics dominating the frequency spectrum. The simulations are incapable of modelling blade flap and vortex shedding frequencies which is seen in the experimental frequency spectrum as well as higher frequency fluctuations.

Fault detection for the mistracking blade was assessed through an analysis of the rotor forces and moments, pressure signals probed in the field and from the pressure along the surface of the blades. The forces, moments and pressure signals detect the fault as increases in the 1/rev frequency amplitudes. The field recorded pressure signals could also be compared in the time-domain where the fault is identified as a deviation between the pressure profiles for the particular blade. The field pressure signals were compared for their efficacy based on where they were located. This concluded that recordings in the field of the rotor should be taken at radial locations representing the outer half of the blade but not past its tip and normal locations up to 0.3 m could detect the fault but will most likely be affected by other factors. Comparison of the surface pressure contours concluded that blade asymmetry could be detected using this approach but a high level of fidelity is required in order to visualise and capture the specific fault.

Finally, a reflection was given on the modelling approach. Good CFD practices were followed and an economical model was constructed but the simulations were still computationally intense. Recommendations are given to generate a better all-round mesh for such an analysis and to consider case setup parameters such as the discretisation schemes.

Chapter 5 – Conclusions, Limitations and Recommendations

5.1 Conclusions

The development of this study topic was motivated by the lack of literature which represent condition monitoring and fault detection techniques from a fluid dynamic perspective. The majority of condition monitoring techniques are based on structural responses despite a number of rotors possessing a strong coupling between their structural and aerodynamic behaviours. This investigations primary objective was to assess what could be inferred about a fault from the flow field in order to determine the feasibility of fluid dynamic based fault detection for rotor systems.

The investigation was conducted numerically but experiments were performed in order to capture validation data. Experiments consisted of acquiring time dependent pressure data in the field of a helicopter tail rotor. Transducers recorded data at 6 locations and were processed to represent the rotor at constant speed. Comparison of the experimental data with the results produced numerically, revealed good correlation between the results. The numerical results represented the pressure peaks and troughs when the blade passed specified locations well, but lacked the ability to represent blade flapping and higher frequency fluctuations. The lack in modelling of these phenomena were anticipated since an aero-elastic analysis (a rigid rotor was modelled) was not considered and RANS turbulence modelling was used which is incapable of representing smaller eddies which cause the high frequencies.

Investigative studies were completed in order to make selections on parameters required to set up the final rotor simulations. From these studies it was determined that the Spalart Allmaras turbulence model and an incompressible solver would suffice for the purposes of this study. Other parameters which were determined from this study include the selection of a wall function and the prescription of mesh cell height in order to abide by the y^+ law of the wall.

The simulations were then constructed and run. A number of analyses were used to compare the differences in the results for a rotor that is in a healthy and faulty condition. The results indicate that the fault shows up as an increase in the 1/rev force, moment and field pressure frequency amplitudes. The field pressure measurements were also analysed in the time domain which provides further information on the existence of the fault. This is observed as differences in the pressure troughs for each blade of the faulty rotor. Furthermore, differences could be observed in the pressure contours along the blade for the faulty rotor. Through these conclusions the study proves the ability of monitoring and detecting rotor faults from flow field data.

Detection of the rotor fault as increases in the 1/rev frequency components may seem like a trivial result as a number of other studies have confirmed this for rotor imbalance when monitoring the power characteristics of the rotor. However, the results concluded by this investigation allow better distinction between a mass or aerodynamic imbalance where further analysis of the results could isolate specific faults. For example, a 1/rev increase in the rotor forces and moments (where possible) or by vibrations measured with an accelerometer indicate imbalance but cannot determine the cause. With the information provided by the flow field, the imbalance can be defined as mass or aerodynamic.

Further development may allow for the aerodynamic fault mechanisms to be isolated. Considering the methods explored in this study, the pressure frequencies indicated the existence of the fault while the time domain pressure profiles and the surface pressure contours describe the behaviour of the fault. It is possible that these methods could be used to distinguish asymmetry resulting from the track or pitch of a blade (amongst other faults). The described methods are just examples and could be supplemented with more sophisticated

signal processing techniques and data acquisitioning methods available to extract the required information.

The findings of this investigation conclude that fluid dynamic behaviour carries valuable information about rotor faults. Furthermore, a simple inexpensive pressure transducer placed in the field of the rotor was capable of detecting the fault which is beneficial from a condition monitoring perspective. This research showcased a few simple ways in which the information could be acquired and processed but the success of the investigation opens the door to enhancing techniques in this realm. It is also true that the studies have been shown for their modelling proficiency implying that developments can be considered through model-based diagnostics as long as the limitations of the practical applications are understood.

5.2 Limitations and Recommendations

The selection of modelling parameters, simplifications and assumptions were supported for the particular case considered in this investigation and stated in order to determine the feasibility of the posed hypothesis. The implications of conducting the work in this way needs to be considered in terms of its limitations in its practical application and representation while stating recommendations for future work.

Although it was found that the cheaper Spallart Allmaras turbulence model could be used for the zero-pitched rotor, care should be taken in future modelling in the event that high speed rotor aerodynamics are analysed where there may be more significant fluid dynamic effects such as separation and recirculation with higher pitching angles. A more expensive model such as the k-omega SST model, known to handle these instances better, may be required.

The computational expense and time required to acquire converged results is a limitation which further studies need to consider. This limited the investigation to considering a single instance of one fault mechanism. Recommendations were given on changes which could be made to make the studies more efficient in Section 4.4 and are mainly based around the mesh and discretisation schemes used. Another factor which could be considered, is the location at which the boundaries are situated relative to the blade since this could impact the stability of the simulation depending on the boundary conditions used which may reduce the simulation time required. These recommendations could be made without effecting the numerical accuracy and resolution of flow phenomena but in order to make the simulations even more economical it may be appropriate to sacrifice a small amount of accuracy. These constraints need to be reduced in order for a variety of other studies to be parametrically conducted.

In performing the simulations with an efficient model, other fault mechanisms can be considered. The fluid dynamic information relating to particular faults can be compared and studied for trends so that the fault can be specifically identified amongst others.

Geometric representation of the blade neglected the trim tab for the feasibility study. Trim tabs and pitch control rods are the two components adjusted when performing rotor track and balance to realise aerodynamic changes. This should be considered in future investigations to detail the effect of each to formulate better Rotor Track and Balance correction algorithms. However, it may be difficult to develop a practical correction algorithm of this sort without an aero-elastic analysis since these changes would affect the structural behaviour of the rotor system.

Comparison of the experimental and numerical pressure field results found that the model was incapable of representing certain phenomena. These phenomena were described as either the blade flapping (or vibrations about the flap hinge) as a result of its flexible coupling at the hub or due to vortex shedding. Neither of these two phenomena could be confidently identified nor neglected. Due to the rigid rotor assumption and the use of RANS turbulence modelling it was not expected of the model to represent these phenomena. Future studies should consider these effects in either a numerical or experimental investigation to better characterise the

behaviour and understand its effects on the pressure results to ensure that it does not impair the fault features of the condition monitoring strategy introduced.

One of the prime limitations of the work conducted comes as a result of neglecting external interactions. External interactions could have severe effects on the characteristics exhibited by the flow especially when one considers something like the downwash of the helicopter main rotor onto the tail rotor blade. It is not certain how the fault detection capabilities of the flow field would hold up in such circumstances and requires further investigation.

In this analysis, to detect the seeded fault the time-domain pressure profiles over one revolution were compared. This was proved to be a good method upon which to make comparisons. The issue is that the numerical pressure profiles resolved the pressure peaks very well whereas Chapter 2 showed that the pressure measurements recorded experimentally were sampled low due to the transducer limitation. Experimental comparisons using this method require the use of transducers which can sample higher and resolve the pressure profile per revolution well. The experimental work of Chapter 2 also attempted to measure the air velocity in the vicinity of the rotor blade but the equipment used was found to have an inadequate sampling frequency which could not produce useful measurements for the analysis. These conclusions express the importance of suitable equipment selection for such an analysis. Additionally, improvements in the acquisitioning of information from the flow field may warrant more sophisticated signal processing techniques. Even though the time-domain and frequency-domain analyses used in this study showed some success, these techniques are somewhat basic implying that future work may determine alternative fault detection features if more attention is afforded to the signal processing used.

Another limitation which needs to be considered for the research conducted is the acquisitioning of information in a practical environment. This study considered pressure transducers in the field of the rotor which is possible for grounded or hovering helicopter rotors but would be difficult to implement on a wind turbine. One could mount a pressure transducer on the tower of the wind turbine but corrections would be needed for the effect the tower has on the pressure results, the effect of external interactions such as winds and the distance away from the blade would need to be checked to ensure that it can detect blade anomalies. The positioning of the transducer may also present an issue as the nacelle rotates to face headwinds. Likewise, a simple inexpensive pressure transducer could be fitted to the tail boom of the helicopter but may also require corrections due to the fluid dynamic interactions. Other acquisitioning and detection techniques were alluded to in Chapter 1 which may be useful but were pending the success of detecting the fault from the fluid dynamics. These included the use of pressure sensitive paints and acoustic cameras to detect noise asymmetries between the blades which may be more applicable but require further research.

References

Abbott, I. H. and Von Doenhoff, A. E. (1959). Theory of Wing Sections: Including a Summary of Airfoil data. *Press*, 11, p. 693. doi: 10.1086/470266.

Agard (1979). Experimental Data Base for Computer Program Assessment. Report of the Fluid Dynamics Panel Working Group 04, Agard AR-138.

Airfoil Tools (2017). NACA 0012 AIRFOILS (n0012-il). [Online] Available at: http://airfoiltools.com/airfoil/details?airfoil=n0012-il [Accessed 14 September 2017].

Allmark, M. (2016). Condition monitoring and fault diagnosis of tidal stream turbines subjected to rotor imbalance faults. Available at: http://orca.cf.ac.uk/98633/.

Amenabar, I., Mendikute, A., López-Arraiza, A., Lizaranzu, M. and Aurrekoetxea, J. (2011). Comparison and analysis of non-destructive testing techniques suitable for delamination inspection in wind turbine blades. *Composites Part B: Engineering*. Elsevier Ltd, 42(5), pp. 1298–1305. doi: 10.1016/j.compositesb.2011.01.025.

ANSYS Inc. (2006). Modeling turbulent flows. [Online] Available at: http://www.southampton.ac.uk/~nwb/lectures/GoodPracticeCFD/Articles/Turbulence_Notes_Fluent-v6.3.06.pdf [Accessed October 2017].

Bakker, A. & Fluent Inc. (2002-2008). Computational Fluid Dynamics. [Online] Available at: http://www.bakker.org/dartmouth06/engs150/ [Accessed July 2017].

Bechhoefer, E., Fang, A. and Garcia, E. (2014). Rotor Track and Balance Improvements. *Annual Conference of the Prognostics and Health Management Society*, pp. 1–9.

Ben-Ari, R. and Rosen, A. (1997). MATHEMATICAL MODELLING OF A HELICOPTER ROTOR TRACK AND BALANCE: RESULTS. *Journal of Sound and Vibration*, 200(5), pp. 605–620. doi: 10.1006/jsvi.1996.0670.

Bramwell, A. R. S., Done, G. and Balmford, D. (2000). Bramwell's Helicopter Dynamics. *Bramwell's Helicopter Dynamics*, pp. 1–397. doi: 10.1016/B978-075065075-5/50005-1.

Cardenas Cabada, E., Leclere, Q., Antoni, J. and Hamzaoui, N. (2017). Fault detection in rotating machines with beamforming: Spatial visualization of diagnosis features. *Mechanical Systems and Signal Processing*. Elsevier Ltd, 97, pp. 33–43. doi: 10.1016/j.ymssp.2017.04.018.

Carr, L. W. and Yu, Y. H. (1992). The use of interferometry in the study of rotorcraft aerodynamics. *Optics and Lasers in Engineering*, 17(3–5), pp. 121–146. doi: 10.1016/0143-8166(92)90032-3.

Cengel, Y. A. & Ghajar, A. J. (2011). Heat and Mass Transfer: Fundamentals and Applications. Fifth Edition in SI Units ed. New York: McGraw Hill Education.

Conlisk, A. T. (1997). Modern helicopter aerodynamics. *Annual review of fluid mechanics*, 29(1), pp. 515–567. doi: 10.1146/annurev.fluid.29.1.515.

Disotell, K. J., Nikoueeyan, P., Naughton, J. W. and Gregory, J. W. (2016). Global surface pressure measurements of static and dynamic stall on a wind turbine airfoil at low Reynolds number. *Experiments in Fluids*. Springer Berlin Heidelberg, 57(5), pp. 1–15. doi: 10.1007/s00348-016-2175-z.

Donea, J., Huerta, A., Ponthot, J. Ph. and Rodríguez-Ferran, A. (2017). Arbitrary Lagrangian-Eulerian Methods. *Encyclopedia of Computational Mechanics Second Edition*, pp. 1–23. doi: 10.1002/9781119176817.ecm2009.

Duarte, F., Gormaz, R. and Natesan, S. (2004). Arbitrary Lagrangian-Eulerian method for Navier-Stokes equations with moving boundaries. *Computer Methods in Applied Mechanics and Engineering*, 193(45–47), pp. 4819–4836. doi: 10.1016/j.cma.2004.05.003.

Forbes, G. L. and Randall, R. B. (2013). Estimation of turbine blade natural frequencies from casing pressure and vibration measurements. *Mechanical Systems and Signal Processing*. Elsevier, 36(2), pp. 549–561. doi: 10.1016/j.ymssp.2012.11.006.

Ganguli, R., Chopra, I. and Haas, D. J. (1998). Simulation of Helicopter Rotor-System Structural Damage, Blade Mistracking, Friction, and Freeplay. *Journal of Aircraft*, 35(4), pp. 591–597. doi: 10.2514/2.2342.

García Márquez, F. P., Tobias, A. M., Pinar Pérez, J. M. and Papaelias, M. (2012). Condition monitoring of wind turbines: Techniques and methods. *Renewable Energy*. Elsevier Ltd, 46, pp. 169–178. doi: 10.1016/j.renene.2012.03.003.

Gardner, A. D., Klein, C., Sachs, W. E., Henne, U., Mai, H. and Richter, K. (2014). Investigation of three-dimensional dynamic stall on an airfoil using fast-response pressure-sensitive paint. *Experiments in Fluids*, 55(9), pp. 1–14. doi: 10.1007/s00348-014-1807-4.

Gwashavanhu, B., Oberholster, A. J. and Heyns, P. S. (2016). Rotating blade vibration analysis using photogrammetry and tracking laser Doppler vibrometry. *Mechanical Systems and Signal Processing*. Elsevier, 76–77, pp. 174–186. doi: 10.1016/j.ymssp.2016.02.019.

Hameed, Z., Hong, Y. S., Cho, Y. M., Ahn, S.H. and Song, C. K. (2009). Condition monitoring and fault detection of wind turbines and related algorithms: A review. *Renewable and Sustainable Energy Reviews*, 13(1), pp. 1–39. doi: 10.1016/j.rser.2007.05.008.

Hirt, C. W., Amsden, A. A. and Cook, J. L. (1974). An arbitrary Lagrangian-Eulerian computing method for all flow speeds. *Journal of Computational Physics*, 14(3), pp. 227–253. doi: 10.1016/0021-9991(74)90051-5.

Potsdam, M., Hyeonsoo, Y. and Johnson, W. (2004). Rotor Airloads Prediction Using Loose Aerodynamics/Structural Coupling.

Karimian, S. M. H. and Ardakani, M. (2011). Immersed Boundary Method for the Solution of 2D Inviscid Compressible Flow Using Finite Volume Approach on Moving Cartesian Grid. *Journal of Applied Fluid Mechanics*, 4(2), pp. 27–36.

Kusnick, J., Adams, D. E. and Griffith, D. T. (2015). Wind turbine rotor imbalance detection using nacelle and blade measurements. *Wind Energy*, 18(2), pp. 267–276. doi: 10.1002/we.1696.

LEAP CFD Team (2013). Turbulence Part 3 – Selection of wall functions and Y+ to best capture the Turbulent Boundary Layer. Leap Australia and New Zealand - Computational Fluid Dynamics (CFD) Blog. [Online] Available at: http://www.computationalfluiddynamics.com.au/turbulence-part-3-selection-of-wall-functions-and-y-to-best-capture-the-turbulent-boundary-layer/ [Accessed 15 August 2017].

Li, C., Lin, Q., Ding, X. and Ye, X. (2016). Performance, aeroacoustics and feature extraction of an axial flow fan with abnormal blade angle. *Energy*. Elsevier Ltd, 103, pp. 322–339. doi: 10.1016/j.energy.2016.02.147.

Lundstrom, T., Baqersad, J. and Niezrecki, C. (2016). Monitoring the Dynamics of a Helicopter Main Rotor With High-Speed Stereophotogrammetry. *Experimental Techniques*, 40(3), pp. 907–919. doi: 10.1007/s40799-016-0092-y.

Madar, E., Klein, R. and Bortman, J. (2019). Contribution of dynamic modeling to prognostics of rotating machinery. *Mechanical Systems and Signal Processing*. Elsevier Ltd, 123, pp. 496–512. doi: 10.1016/j.ymssp.2019.01.003.

Oggiano, L., Boorsma, K., Schepers, G. and Kloosterman, M. (2016). Comparison of simulations on the NewMexico rotor operating in pitch fault conditions. *Journal of Physics: Conference Series*, 753(2). doi: 10.1088/1742-6596/753/2/022049.

OpenCFD Ltd (2004-2019). OpenFOAM. [Online] Available at: https://www.openfoam.com/ [Accessed August 2017].

Ozbek, M., Rixen, D. J., Erne, O. and Sanow, G. (2010). Feasibility of monitoring large wind turbines using photogrammetry. *Energy*. Elsevier Ltd, 35(12), pp. 4802–4811. doi: 10.1016/j.energy.2010.09.008.

Pandey, K. M., Kumar, G., Das, D., Deka, D., Surana, A. and Das, H. J. (2012). CFD Analysis of an Isolated Main Helicopter Rotor for a Hovering Flight. *Volume 1: Advances in Aerospace Technology*. ASME, p. 543. doi: 10.1115/IMECE2012-89227.

Park, K. S., Asim, T. and Mishra, R. (2012). Computational fluid dynamics based fault simulations of a vertical axis wind turbines. *Journal of Physics: Conference Series*, 364(1). doi: 10.1088/1742-6596/364/1/012138.

Pawar, P. M. and Ganguli, R. (2007). Helicopter rotor health monitoring - A review. *Proceedings of the Institution of Mechanical Engineers, Part G: Journal of Aerospace Engineering*, 221(5), pp. 631–647. doi: 10.1243/09544100JAERO245.

Renzi, M. J. (2004). An Assessment of Modern Methods for Rotor Track and Balance.

Rosen, A. and Ben-Ari, R. (1997). MATHEMATICAL MODELLING OF A HELICOPTER ROTOR TRACK AND BALANCE: THEORY. *Journal of Sound and Vibration*, 200(5), pp. 589–603. doi: 10.1006/jsvi.1996.0669.

Rumsey, C. (2016). NASA Langley Research Center: Turbulence Modeling Resource. [Online] Available at: https://turbmodels.larc.nasa.gov/naca0012_val.html [Accessed 25 September 2017].

Singh, H. K., Pawar, P. M., Ganguli, R. and Nam Jung, S. (2008). On the effect of mass and stiffness unbalance on helicopter tail rotor system behavior. *Aircraft Engineering and Aerospace Technology*, 80(2), pp. 129–138. doi: 10.1108/00022660810859355.

Smith, L. (2017). Investigation of a modified low-drag body for an alternative wing-body-tail configuration. Pretoria: University of Pretoria.

Strawn, R. C. and Biswas, R. (1996). Numerical simulations of helicopter aerodynamics and acoustics. *Journal of Computational and Applied Mathematics*, 66(1–2), pp. 471–483. doi: 10.1016/0377-0427(95)00171-9.

Stupar, S., Simonović, A. and Jovanović, M. (2012). Measurement and Analysis of Vibrations on the Helicopter Structure in Order to Detect Defects of Operating Elements. *Scientific Technical Review*, 62(1), pp. 58–63.

Versteeg, H. K. & Malalasekera, W. (2007). An Introduction to Computational Fluid Dynamics - The Finite Volume Method. Second ed. Essex, England: Pearson Education Limited.

Wagner, S. (2005). Flow-Structure Interactions on Helicopter Rotors in Forward Flight. *GAMM-Mitteilungen*, 28(1), pp. 7–36. doi: 10.1002/gamm.201490015.

Weiss, A., Geisler, R., Schwermer, T., Yorita, D., Henne, U., Klein, C. and Raffel, M. (2017). Single-shot pressure-sensitive paint lifetime measurements on fast rotating blades using an optimized double-shutter technique. *Experiments in Fluids*. Springer Berlin Heidelberg, 58(9), pp. 1–20. doi: 10.1007/s00348-017-2400-4.

White , F. M. (2011). Fluid Mechanics. Seventh ed. New York: McGraw - Hill Education.

Xu, C. and Amano, R. S. (2002). Unsteady Pressure Field Investigation of an Axial Fan—Blade Unsteady Pressure Field Measurement. *International Journal of Rotating Machinery*, 8(6), pp. 385–395. doi: 10.1155/S1023621X02000362.

Xu, C., Amano, R. S. and Perez, R. (2002). Unsteady Pressure Field Investigation of an Axial Fan—Inlet and Outlet Unsteady Pressure Field Measurement. *International Journal of Rotating Machinery*, 8(6), pp. 375–383. doi: 10.1155/S1023621X02000350.

Yang, B. and Sun, D. (2013). Testing, inspecting and monitoring technologies for wind turbine blades: A survey. *Renewable and Sustainable Energy Reviews* 22, pp. 515–526.

Yu, Y. H. (2000). Rotor blade-vortex interaction noise. *Progress in Aerospace Sciences*, 36(2), pp. 97–115. doi: 10.1016/S0376-0421(99)00012-3.

Appendices

Appendix A – Case Files

0 – nut:

```
/*--------------------------------*- C++ -*----------------------------------*\
| =========                 |                                                 |
| \\      /  F ield         | OpenFOAM: The Open Source CFD Toolbox           |
|  \\    /   O peration     | Version:  4.x                                   |
|   \\  /    A nd           | Web:      www.OpenFOAM.org                      |
|    \\/     M anipulation  |                                                 |
\*---------------------------------------------------------------------------*/
FoamFile
{
    version     2.0;
    format      ascii;
    class       volScalarField;
    object      nut;
}
// * * * * * * * * * * * * * * * * * * * * * * * * * * * * * * * * * * * * //

dimensions      [0 2 -1 0 0 0 0];

internalField   uniform 0.00001098963297;

boundaryField
{
    //- Set patchGroups for constraint patches
    #includeEtc "caseDicts/setConstraintTypes"

    wall        // OR "rotor.*"
    {
        type            nutUSpaldingWallFunction;
        value           uniform 0;
    }

    ".*boundary"
    {
        type            freestream;
        freestreamValue uniform 0.00001098963297;
    }

}
```

0 – nuTilda:

```
/*--------------------------------*- C++ -*----------------------------------*\
| =========                 |                                                 |
| \\      /  F ield         | OpenFOAM: The Open Source CFD Toolbox           |
|  \\    /   O peration     | Version:  4.x                                   |
|   \\  /    A nd           | Web:      www.OpenFOAM.org                      |
|    \\/     M anipulation  |                                                 |
\*---------------------------------------------------------------------------*/
FoamFile
{
    version     2.0;
    format      ascii;
    class       volScalarField;
    object      nuTilda;
}
// * * * * * * * * * * * * * * * * * * * * * * * * * * * * * * * * * * * * //

dimensions      [0 2 -1 0 0 0 0];

internalField   uniform 0.00005842938776;

boundaryField
{
    //- Set patchGroups for constraint patches
    #includeEtc "caseDicts/setConstraintTypes"

    wall        // OR "rotor.*"
    {
        type            fixedValue;
        value           uniform 0;
    }

    ".*boundary"
    {
        type            freestream;
        freestreamValue uniform 0.00005842938776;
    }
}
```

0 – p:

```
/*--------------------------------*- C++ -*----------------------------------*\
| =========                 |                                                 |
| \\      /  F ield         | OpenFOAM: The Open Source CFD Toolbox           |
|  \\    /   O peration     | Version:  4.x                                   |
|   \\  /    A nd           | Web:      www.OpenFOAM.org                      |
|    \\/     M anipulation  |                                                 |
\*---------------------------------------------------------------------------*/
FoamFile
{
    version     2.0;
    format      ascii;
    class       volScalarField;
    object      p;
}
// * * * * * * * * * * * * * * * * * * * * * * * * * * * * * * * * * * * * //

dimensions      [0 2 -2 0 0 0 0];

internalField   uniform 0;

boundaryField
{
    //- Set patchGroups for constraint patches
    #includeEtc "caseDicts/setConstraintTypes"

    wall        // OR "rotor.*"
    {
        type            zeroGradient;
    }

    ".*boundary"
    {
        type            zeroGradient;
    }
}
```

0 – U:

```
/*--------------------------------*- C++ -*----------------------------------*\
| =========                 |                                                 |
| \\      /  F ield         | OpenFOAM: The Open Source CFD Toolbox           |
|  \\    /   O peration     | Version:  4.x                                   |
|   \\  /    A nd           | Web:      www.OpenFOAM.org                      |
|    \\/     M anipulation  |                                                 |
\*---------------------------------------------------------------------------*/
FoamFile
{
    version     2.0;
    format      ascii;
    class       volVectorField;
    object      U;
}
// * * * * * * * * * * * * * * * * * * * * * * * * * * * * * * * * * * * * //

dimensions      [0 1 -1 0 0 0 0];

internalField   uniform (0 0 0);

boundaryField
{
    //- Set patchGroups for constraint patches
    #includeEtc "caseDicts/setConstraintTypes"

    wall        // OR "rotor.*"
    {
        type            movingWallVelocity;
        value           uniform (0 0 0);
    }

    ".*boundary"
    {
        type            zeroGradient;
    }

}
```

constant – dynamicMeshDict:

```
/*--------------------------------*- C++ -*----------------------------------*\
| =========                 |                                                 |
| \\      /  F ield         | OpenFOAM: The Open Source CFD Toolbox           |
|  \\    /   O peration     | Version:  4.x                                   |
|   \\  /    A nd           | Web:      www.OpenFOAM.org                      |
|    \\/     M anipulation  |                                                 |
\*---------------------------------------------------------------------------*/
FoamFile
{
    version     2.0;
    format      ascii;
    class       dictionary;
    location    "constant";
    object      dynamicMeshDict;
}
// * * * * * * * * * * * * * * * * * * * * * * * * * * * * * * * * * * * * //

dynamicFvMesh   dynamicMotionSolverFvMesh;          //solidBodyMotionFvMesh;

motionSolverLibs ( "libfvMotionSolvers.so" );

solver solidBody;

solidBodyCoeffs
{
    cellZone        air;

    solidBodyMotionFunction  rotatingMotion;
    rotatingMotionCoeffs
    {
    origin      (0 0 0);
    axis        (0 1 0);
    omega       191.64; // rad/s from 1830 RPM
    }
}
```

constant – transportProperties:

```
/*--------------------------------*- C++ -*----------------------------------*\
| =========                 |                                                 |
| \\      /  F ield         | OpenFOAM: The Open Source CFD Toolbox           |
|  \\    /   O peration     | Version:  4.x                                   |
|   \\  /    A nd           | Web:      www.OpenFOAM.org                      |
|    \\/     M anipulation  |                                                 |
\*---------------------------------------------------------------------------*/
FoamFile
{
    version     2.0;
    format      ascii;
    class       dictionary;
    location    "constant";
    object      transportProperties;
}
// * * * * * * * * * * * * * * * * * * * * * * * * * * * * * * * * * * * * //

transportModel  Newtonian;

nu              [0 2 -1 0 0 0 0] 1.4607e-05;
```

constant – turbulenceProperties:

```
/*--------------------------------*- C++ -*----------------------------------*\
| =========                 |                                                 |
| \\      /  F ield         | OpenFOAM: The Open Source CFD Toolbox           |
|  \\    /   O peration     | Version:  4.x                                   |
|   \\  /    A nd           | Web:      www.OpenFOAM.org                      |
|    \\/     M anipulation  |                                                 |
\*---------------------------------------------------------------------------*/
FoamFile
{
    version     2.0;
    format      ascii;
    class       dictionary;
    location    "constant";
    object      turbulenceProperties;
}
// * * * * * * * * * * * * * * * * * * * * * * * * * * * * * * * * * * * * //

simulationType RAS;

RAS
{
    RASModel        SpalartAllmaras;

    turbulence      on;

    printCoeffs     on;
}
```

system – controlDict:

```
/*--------------------------------*- C++ -*----------------------------------*\
| =========                 |                                                 |
| \\      /  F ield         | OpenFOAM: The Open Source CFD Toolbox           |
|  \\    /   O peration     | Version:  4.x                                   |
|   \\  /    A nd           | Web:      www.OpenFOAM.org                      |
|    \\/     M anipulation  |                                                 |
\*---------------------------------------------------------------------------*/
FoamFile
{
    version     2.0;
    format      ascii;
    class       dictionary;
    location    "system";
    object      controlDict;
}
// * * * * * * * * * * * * * * * * * * * * * * * * * * * * * * * * * * * * //
application     pimpleDyMFoam;

startFrom       latestTime;

startTime       0;

stopAt          endTime;

endTime         0.65;

deltaT          1e-07;

writeControl    adjustableRunTime;

writeInterval   0.001;

purgeWrite      0;

writeFormat     ascii;//binary

writePrecision  8;

writeCompression true;

timeFormat      general;

timePrecision   8;

runTimeModifiable true;

adjustTimeStep true;

maxCo   2.0;
functions
{
    #include "forces"
    #include "probes"
}
```

system – decomposeParDict:

```
/*--------------------------------*- C++ -*----------------------------------*\
| =========                 |                                                 |
| \\      /  F ield         | OpenFOAM: The Open Source CFD Toolbox           |
|  \\    /   O peration     | Version:  4.x                                   |
|   \\  /    A nd           | Web:      www.OpenFOAM.org                      |
|    \\/     M anipulation  |                                                 |
\*---------------------------------------------------------------------------*/
FoamFile
{
    version     2.0;
    format      ascii;
    class       dictionary;
    location    "system";
    object      decomposeParDict;
}
// * * * * * * * * * * * * * * * * * * * * * * * * * * * * * * * * * * * * //

numberOfSubdomains 120;

method          scotch;
```

system – forces:

```
/*--------------------------------*- C++ -*----------------------------------*\
| =========                 |                                                 |
| \\      /  F ield         | OpenFOAM: The Open Source CFD Toolbox           |
|  \\    /   O peration     | Version:  4.x                                   |
|   \\  /    A nd           | Web:      www.OpenFOAM.org                      |
|    \\/     M anipulation  |                                                 |
\*---------------------------------------------------------------------------*/

rotorforces
{
    type            forces;
    functionObjectLibs  ("libforces.so");
    writeControl        timeStep;
    writeInterval       1;
    log             true;

    patches           ( "rotor.*" );
    pName             p;
    UName             U;

    rho             rhoInf;       //Indicates incompressible
    rhoInf          1.225;      // Redundant for incompressible

    CofR            (0 0 0);    // Centre of rotation for moment calculations
}
```

system – fvSchemes.start:

```
/*---------------------------------*- C++ -*----------------------------------*\
| =========                 |                                                 |
| \\      /  F ield         | OpenFOAM: The Open Source CFD Toolbox           |
|  \\    /   O peration     | Version:  plus                                  |
|   \\  /    A nd           | Web:      www.OpenFOAM.com                      |
|    \\/     M anipulation  |                                                 |
\*---------------------------------------------------------------------------*/
FoamFile
{
    version     2.0;
    format      ascii;
    class       dictionary;
    object      fvSchemes;
}
// * * * * * * * * * * * * * * * * * * * * * * * * * * * * * * * * * * * * //

ddtSchemes
{
    default             Euler;
}

gradSchemes
{
    default         none;
    grad(p)         cellLimited Gauss linear 1;
    grad(pcorr)     cellLimited Gauss linear 1;
    grad(U)         cellLimited Gauss linear 1;
    grad(nuTilda)   cellLimited Gauss linear 1;
}

divSchemes
{
    default                     none;
    div(phi,U)                  Gauss linearUpwind grad(U);
    div(phi,nuTilda)            Gauss limitedLinear 1;
    div((nuEff*dev2(T(grad(U))))) Gauss linear;
}

laplacianSchemes
{
    default         Gauss linear limited corrected 0.5;
}
interpolationSchemes
{
    default         linear;
}
snGradSchemes
{
    default         corrected;
}
wallDist
{
    method meshWave;
}
```

system – fvSchemes.finish:

```
/*--------------------------------*- C++ -*----------------------------------*\
| =========                 |                                                 |
| \\      /  F ield         | OpenFOAM: The Open Source CFD Toolbox           |
|  \\    /   O peration     | Version:  plus                                  |
|   \\  /    A nd           | Web:      www.OpenFOAM.com                      |
|    \\/     M anipulation  |                                                 |
\*---------------------------------------------------------------------------*/
FoamFile
{
    version     2.0;
    format      ascii;
    class       dictionary;
    object      fvSchemes;
}
// * * * * * * * * * * * * * * * * * * * * * * * * * * * * * * * * * * * * //

ddtSchemes
{
    default             CrankNicolson 0.9;
}

gradSchemes
{
    default         none;
    grad(p)         cellLimited Gauss linear 0.6;
    grad(pcorr)     cellLimited Gauss linear 0.6;
    grad(U)         cellLimited Gauss linear 0.6;
    grad(nuTilda)   cellLimited Gauss linear 0.6;
}

divSchemes
{
    default                     none;
    div(phi,U)                  Gauss linearUpwind grad(U);       //First/Second order, bounded
    div(phi,nuTilda)            Gauss limitedLinear 1;            //First/Second order, bounded
    div((nuEff*dev2(T(grad(U))))) Gauss linear;                   //Second order, unbounded
}

laplacianSchemes
{
    default         Gauss linear limited corrected 0.5;
}
interpolationSchemes
{
    default         linear;
}
snGradSchemes
{
    default         corrected;
}
wallDist
{
    method meshWave;
}
```

system – fvSolution:

```
/*---------------------------------*- C++ -*----------------------------------*\
| =========                 |                                                 |
| \\      /  F ield         | OpenFOAM: The Open Source CFD Toolbox           |
|  \\    /   O peration     | Version:  plus                                  |
|   \\  /    A nd           | Web:      www.OpenFOAM.com                      |
|    \\/     M anipulation  |                                                 |
\*---------------------------------------------------------------------------*/
FoamFile
{
    version     2.0;
    format      ascii;
    class       dictionary;
    object      fvSolution;
}
// * * * * * * * * * * * * * * * * * * * * * * * * * * * * * * * * * * * * //

solvers
{
    "pcorr.*"
    {
        solver          GAMG;
        tolerance       0.02;
        relTol          0;
        smoother        GaussSeidel;
    }

    p
    {
        $pcorr
        tolerance       1e-7;
        relTol          0.01;
    }

    pFinal
    {
        $p;
        tolerance       1e-7;
        relTol          0;
    }

    "(U|nuTilda)"
    {
        solver          smoothSolver;
        smoother        symGaussSeidel;
        tolerance       1e-06;
        relTol          0.1;
    }

    "(U|nuTilda)Final"
    {
        $U;
        tolerance       1e-06;
        relTol          0;
```

```
    }
}

PIMPLE
{
    correctPhi          yes;
    nOuterCorrectors    2;
    nCorrectors         2;
    nNonOrthogonalCorrectors 3;
    pRefPoint               (1.93 0 0);
//    pRefCell            31795;
    pRefValue           0;
}

relaxationFactors
{
    fields
    {
        p               0.3;
    }
    equations
    {
        "(U|nuTilda)"   0.7;
        "(U|nuTilda)Final" 1.0;
    }
}

cache
{
    grad(U);
}
```

system – probes:

```
/*--------------------------------*- C++ -*----------------------------------*\
  =========                 |
  \\      /  F ield         | OpenFOAM: The Open Source CFD Toolbox
   \\    /   O peration     |
    \\  /    A nd           | Web:      www.OpenFOAM.org
     \\/     M anipulation  |
-------------------------------------------------------------------------------
Description
    Writes out values of fields from cells nearest to specified locations.
\*---------------------------------------------------------------------------*/

testingprobes
{
type            probes;
libs            ("libsampling.so");

writeControl    timeStep;
writeInterval   1;

fields (p U);
```

```
probeLocations
(
    (0 0.02 0.62)
    (0 0.02 0.744)
    (0 0.02 0.93)
    (0 0.1 0.62)
    (0 0.1 0.744)
    (0 0.1 0.93)
    (0 0.2 0.62)
    (0 0.2 0.744)
    (0 0.2 0.93)
    (0 0.3 0.62)
    (0 0.3 0.744)
    (0 0.3 0.93)

    (0 -0.02 0.62)
    (0 -0.02 0.744)
    (0 -0.02 0.93)
    (0 -0.1 0.62)
    (0 -0.1 0.744)
    (0 -0.1 0.93)
    (0 -0.2 0.62)
    (0 -0.2 0.744)
    (0 -0.2 0.93)
    (0 -0.3 0.62)
    (0 -0.3 0.744)
    (0 -0.3 0.93)

    (0 0.1 1.03)
    (0 0.1 1.13)
    (0 0.1 1.23)
    (0 0.2 1.03)
    (0 0.2 1.13)
    (0 0.2 1.23)
    (0 0.3 1.03)
    (0 0.3 1.13)
    (0 0.3 1.23)
    (0 0 1.03)
    (0 0 1.13)
    (0 0 1.23)
    (0 -0.1 1.03)
    (0 -0.1 1.13)
    (0 -0.1 1.23)
    (0 -0.2 1.03)
    (0 -0.2 1.13)
    (0 -0.2 1.23)
    (0 -0.3 1.03)
    (0 -0.3 1.13)
    (0 -0.3 1.23)

    (0 0.25 0.62)
    (0 0.25 0.93)
);

}
```

Appendix B – Additional Rotor Simulation Convergence Plots

Healthy	**Faulty**
Residual Plot: 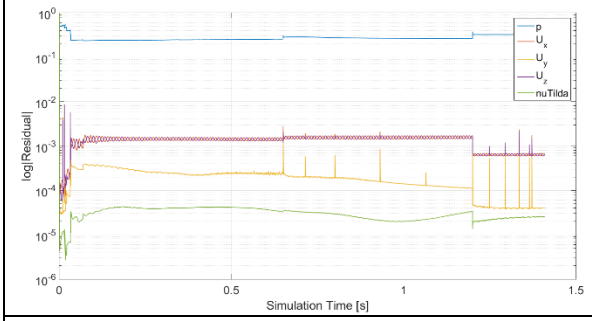	Residual Plot: 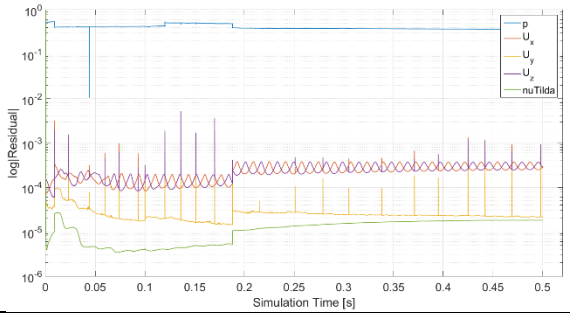
Maximum Courant Number: 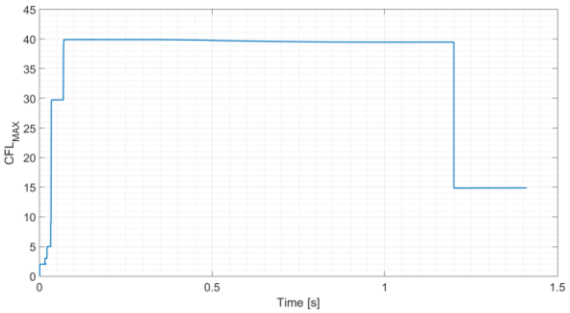	Maximum Courant Number: 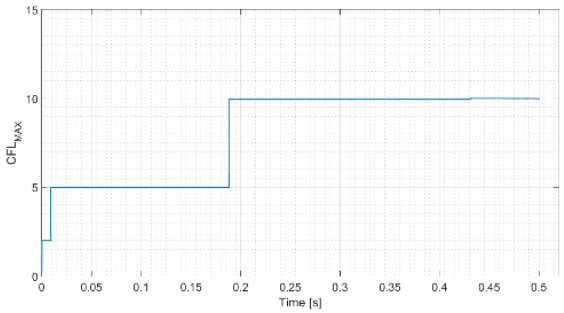
Rotor Moments: 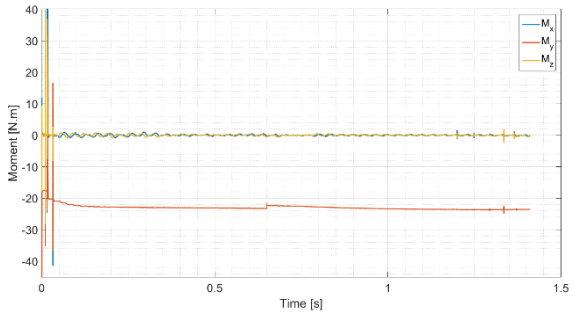	Rotor Moments: 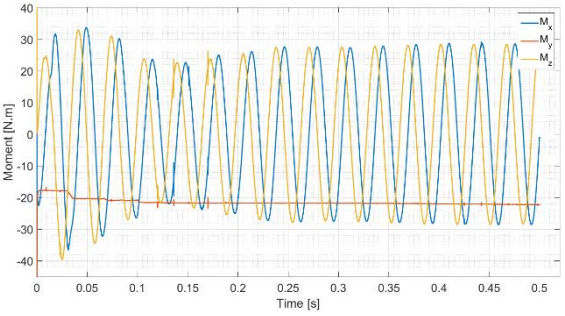
Velocity Measurements: 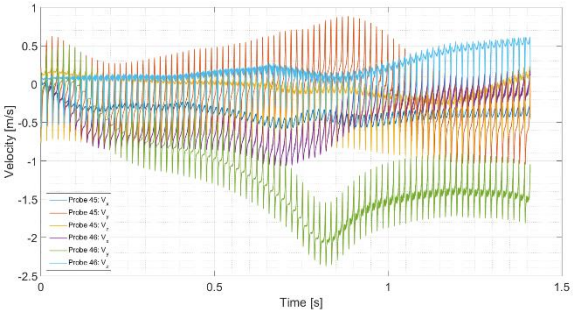	Velocity Measurements: